Investigation of Longitudinal and Transverse Dispersion in Porous Media

by

© **Saeid Eskandari**

A thesis submitted to the School of Gradate Studies in partial fulfillment of the requirements for the degree of Doctor of Philosophy.

Department of Engineering and Applied Science

Memorial University of Newfoundland

May 2019

St. John's, Newfoundland and Labrador, Canada

Abstract

Miscible displacement processes are increasingly feasible methods for the recovery of oil from depleted reservoirs as an enhanced oil recovery (EOR) method. However, a fundamental understanding of the dependency of transport phenomenon to medium properties and their consequent impact on oil recovery efficiency is lacking. Moreover, it is generally believed that miscibility may repeatedly develop and break down in a reservoir due to dispersion arising from velocity and reservoir heterogeneity. Thus, miscible processes are assumed to be dependent on the pore geometry of the reservoir. The current research uses mathematical and unique experimental approaches to investigate miscible displacement in two-dimensional media with focus on pore structure to comprehend the relationship between the transport properties to its pore structure. Transport phenomena significantly influence EOR efficiency and this raises the importance of dispersion and miscibility. The mathematical section of this research uses a statistical oriented mathematical approach to investigate miscible displacement assuming various pore properties to comprehend the relationship between dispersion during miscible displacement and the pore structure. This study focuses on examining the dependence of dispersion in both the longitudinal and transverse directions on heterogeneity and pore geometry using statistical models. The pore element is defined by adjustable distribution functions indicating tortuosity and connectivity of the porous medium. Using random walk theory that assumes the mass transfer occurs as a sequence of discrete physical events as particles move between a series of discrete pore elements, the stochastic functions are used to develop a model to estimate the mechanical dispersion properties of the porous media. The introduced model decouples dispersion in the longitudinal and transverse directions and shows a more specific relationship between dispersion and pore size distribution. An analytical approach is applied to model miscible displacement in a fractured medium to study the effect of velocity on the magnitude of mechanical dispersion. Various displacement scenarios

are assumed to find the the effect of pore properties on dispersion. Results illustrate a strong dependence of mechanical dispersion on pore properties of the medium. Both longitudinal and transverse dispersion coefficients increased by increasing the velocity and heterogeneity ratio. In the experimental section, a new experimental approach has been developed to estimate the average longitudinal and transverse dispersion coefficients in a homogeneous anisotropic porous medium during miscible displacement. A series of miscible flooding tests are conducted and studied. Traditionally, most studies of miscible injection have focused on recovery and mechanism of the method and Peclet number that have been used to find the dispersion and diffusion coefficients from a mathematical correlations. This study utilizes a unique method to estimate the mass transfer properties. A unique image processing tool is developed and used to analyze the developing mixing zone in the process and consequently processed images are used to collaborate with a developed Bayesian estimator tool to fit the dispersion coefficients in analytical solution of Advection-Diffusion Equation (ADE). The details of the approach are explained and obtained images are analyzed and interpreted. The results confirm the strong dependency of the velocity of the displacing fluid and dispersion coefficients in both longitudinal and transverse directions. The effects of anisotropy on miscible mass transport are investigated in this study too.

To my wife Sepideh

and My Parents Sarah and Haji

Acknowledgements

This thesis is the culmination of my journey of Ph.D. which was just like climbing a high peak step by step accompanied with encouragement, hardship, trust, and frustration. When I found myself at top experiencing the feeling of fulfillment, I realized though only my name appears on the cover of this dissertation, a great many people including my lovely wife **Sepideh**, my wonderful parents Haji and Sara, my supportive mother in Law Zohreh, my brothers Vahid, Navid and Siamak. At this moment of accomplishment I am greatly indebted to my always supportive supervisor, **Dr. Lesley James**, who accepted me as her PhD student and offered me her mentorship, motherly love, and care. This work would not have been possible without her guidance and involvement, her support and encouragement on a daily basis from the start of the project till date. Under her guidance I successfully overcame many difficulties and learnt a lot. Her own zeal for perfection, passion, unflinching courage and conviction has always inspired me to do more. For all these, I sincerely thank her from bottom of my heart and will be truly indebted to her throughout my life time.

Statement of contribution

I would like to thank Chevron Canada, Hibernia Management and Development Company (HMDC), Research and Development Corporation of Newfoundland and Labrador (RDC), Natural Sciences and Engineering Research Council of Canada (NSERC), Innovative NL, and the Canadian Foundation for Innovation (CFI) for financial support. I also thank my colleagues in the Hibernia EOR Research Group Kim, Edison, and Shervin for their technical and professional support.

Contents

List of Tables

List of Figures

List of symbols

θ	Angle from x axis	α	Adjustable coefficient
β	Adjustable coefficient	γ	Adjustable coefficient
μ	Fluid viscosity	τ	Tortuosity
ψ	Probability of pore existence	Ψ	Probability of path existence
λ	Mobility of fluid	C	Concentration
D_L	Longitudinal dispersion	R	Pore throat diameter
D	Dispersion	D_T	Transverse dispersion
D_m	Molecular diffusion	K	Absolute permeability
l	Pore throat length	L_n	Total length of pattern
L_n	Actual total length	M	Mobility ratio
p	Pressure	q	Flow rate
Pe	Peclet number	Re	Reynolds number
Sc	Schimdt number	P	Probability
t	Duration of time step	T	Total time
v	Velocity	M	Mobility ratio
v_x, v_y	Velocity components	$\langle\rangle$	Mean

Chapter 1

Introduction

1.1 Preface

Demand for oil as a source of energy continues to grow leading to new research to produce more oil from the reservoirs. Production from reservoirs is divided into three levels. Primary recovery comes from the natural energy source associated with rock and fluid in the reservoir. Approximately 5% to 10% of the oil in the reservoir can be recovered this way [57]. Secondary recovery involves maintaining the reservoir pressure which has already been depleted due to primary oil production, this is achieved by water injection into the aquifer or gas injection into the gas cap. Secondary recovery allows for an additional 25% to 30% of the oil in the reservoir to be produced [57]. Tertiary or enhanced oil recovery (EOR) is used to produce as much of the remaining oil as possible. Various EOR methods have been introduced to improve oil recovery efficiency. A suitable EOR method usually depends on economic or technical limitations, therefore, numerous methods and techniques have been studied from the lab to field scale. The goal of any EOR process is to mobilize any remaining oil. This is achieved by enhancing oil displacement and volumetric sweep efficiencies by the two

different methods as below:

1. Oil displacement efficiency is improved by reducing oil viscosity (e.g. thermal methods) or by reducing capillary forces or interfacial tension (e.g. miscible displacements). When gas is injected at the pressure above the minimum miscibility pressure (MMP) of the reservoir fluid, the process is called near miscible and miscible displacement [72]. An influential factor in the economics and efficiency of a miscible displacement process design is the mass transfer phenomenon between solvent (displacing) and oil (displaced), which involves mechanical dispersion and molecular diffusion [64].

2. Volumetric sweep efficiency is improved by developing a more favourable mobility ratio between the injectant and the remaining oil in place (e.g., water-alternating-gas processes)

Miscible displacement EOR techniques are very efficient methods and broadly used in the world. However, the complexities along with the miscibility in porous media arising from the heterogeneity and fluid properties if displacing and displaced fluids have still remained. For this reason, it is essential to study the acting parameters and physical aspects of this process.

1.2 Motivation

The studies of fluid flow in porous media have become almost essential in many scientific and engineering applications. The increasing demand for energy and consequently oil as the primary source of energy, water as an arising crisis, and in the overall any fluid transport in porous media has importance, such as petroleum and water production. The broad scope of fluid flow through porous media in various branches is

Table 1.1: Classification of studies of fluid flow in porous media

Study Field	Study Category
Pure Mathematics	Functional and Factorial Analysis Partial Differential Equation (PDE) Approach Uniqueness and Existence of Answer Studies
Civil Engineering	Ground Water Flow and Contaminant Studies Encroachment Studies Moisture Flow and Adsorption Studies in Soil
Chemical Engineering	Flotation, Adsorption and Filtration Process Studies Flow Through Process Towers Mixing Process in Pharmaceutical
Petroleum Engineering	Enhanced Oil Recovery (EOR) Fingering and Imbibition Studies Oil Flushing by Solvent in Reservoir Studies
Bio Science	Biological Studies (Plant and Animal Mechanisms) Nuclear Waste Disposal Fluid Flow in Environmental and Natural Studies

shown in Table 1.1. Numerical modeling of multiphase flow in porous media is of interest to characterize and quantify the complex transport phenomena but require experimental validation. Groundwater hydrology is regarded as specific science which includes geology, hydrology and fluid mechanics. This thesis is principally concerned with the modeling of miscible fluid flow through a porous medium. The motivation behind studying these flows lies in the recovery of oil in a process known as miscible displacement, in which a solvent, such as a short-chain hydrocarbon or pressurized carbon-dioxide, is injected into the oil reservoir. The fluid flows through the reservoir along tortuous paths of interconnected pores and pore-throats. The heterogeneity of the porous medium complicates the effectiveness of miscible processes as an EOR method. This complication arises from the difference in path resistance for fluid flow that caused by heterogeneity. Since, the oil tends to be bypassed, as the displacing

fluid follows paths of least resistance; the oil recovery decreases. Hence, the characterization of heterogeneity including the pore size distribution, orientation, connectivity, and sorting are essential factors in miscible processes but need to be investigated.
A study of such complicated system from the modern mathematical point of view associated with advanced programming techniques such as image processing is the primary motivation of the present investigations. In this study, a probabilistic approach is used to describe dispersion of miscible fluids in a heterogeneous porous medium. This will lower the risk of choosing an inappropriate EOR methodology. To achieve this goal, this research consists of a conceptually simple but powerful approach to analyze the transport phenomena in porous media. The mathematical part uses a Random Walk Theory (RWT) technique, which considers that the transport occurs as a sequence of transitions as particles move between a series of discrete pore elements while solved analytical within the Advection-Diffusion Equation (ADE) solution. Depending on the injection condition, different flow regimes are introduced and characterized. The relationship between important pore geometry parameters and transport phenomena are also addressed in this work. The experimental part of the study uses a custom and unique image processing technique with pixel level accuracy to study miscible displacements in complex porous media experimentally.

1.3 Fundamentals

The reservoir here is a porous medium with fluid filled pore space [82]. A porous medium consists of two components of spaces and solids. The void spaces are called pores and are free of solids, embedded within the solid or semi-solid matrix. The pores usually contain a variety of fluids, such as water, oil, or a mixture of different fluids.

1.3.1 Rock properties

The most important geometric properties of rock are porosity and permeability [11]. Porosity (ϕ) is defined as a ratio of pore space over the total volume and permeability (K) is the ability of a porous media to allow fluid pass through it. Grain alignment, pore throat size, pore throat diameter and grain size sorting are a result of sediment deposition and burial history. Tortuosity (τ) as a key parameter describing the geometry and transport properties of porous media is defined as a ratio of average length of fluid paths over the geometrical length [28].

1.3.2 Heterogeneity

The critical challenge in the characterization of porous media is high spatial heterogeneity which makes this class of problems very scale dependent. The scale dependence of heterogeneity can best visualized by the representative elementary volume (REV) concept [8]. Figure 1.1 shows the different domains of scale and their structural properties classification.

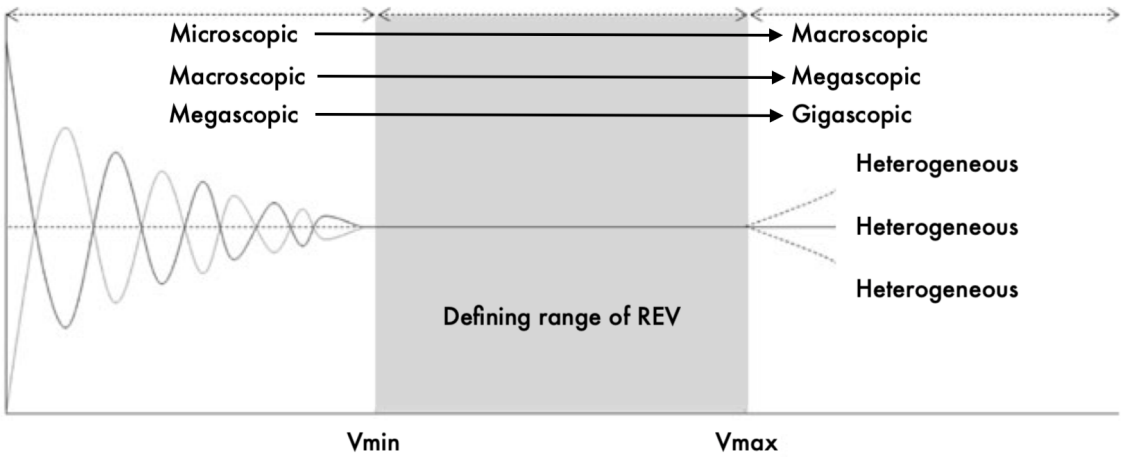

Figure 1.1: The REV depicting zones of different scales of heterogeneity and their relationships. The y axis is any rock properties such as porosity, permeability, and heterogeneity, and x is the volume under investigation. V_{min} and V_{min} are the minimum and maximum volume, representing the elementary

Heterogeneity can be classified into four different categories [40]:

1. Microscopic heterogeneities that exist at the level of the pore surfaces and grains and can be characterized using Scanning Electron Microscopy (SEM) or X-ray computed tomography (CT scan). Characterization and simulations at this scale called pore-scale modeling.

2. Macroscopic heterogeneities that are observed at the core scale where different components of the core may belong to different lithologies with different minerals and transport characteristics. To understand this variability, however, we should use microscopic scale characterization tools.

3. Megascopic heterogeneities that are at the reservoir scale and include faults as well as fractures. A reservoir is an infinitely large number of cores, and its behavior depends on flow properties of cores and their spatial distribution. Also, some heterogeneities only appear at this scale and can change the overall behavior of the flow system drastically. For example, a fault between injection and production wells affects the water-flood performance by reducing the sweep efficiency and recovery factor.

4. Gigascopic heterogeneities that appear at the landscape scale, where reservoirs are studied in the geologic settings relative to rivers, mountains, etc. The characterization at this scale is considered during the exploration phase where seismic techniques are utilized to image the underground rocks.

1.3.3 Miscibility

Fluid displacement in porous media are classified as immiscible or miscible. Immiscible displacement implies that displacing and displaced fluids have clear interface

during the process. When the two phases mix in all properties, it is a miscible displacement and there is no distinct interface between two fluids [68]. Several factors such as fluid density, fluid viscosity and pore properties affect miscibility at the microscopic (pore level) and macroscopic level depending on whether the displacement is a secondary or tertiary recovery process. Under developing miscibility and miscible displacement, mixing of the displacing and displaced fluids by dispersion and diffusion can be significant.

1.3.4 Advection

The amount of material traversing the cross-section depends on the nature of the transporting process. If this process is the passive entrainment of the material by the carrying fluid, then the flux can be related to the concentration and the fluid velocity as follows:

$$\text{flux} = \frac{\text{amount}}{\text{volume of fluid}} \times \frac{\text{volume of fluid}}{\text{area} \times \text{time}} = cv \tag{1.1}$$

where c is fluid concentration and v is the entraining fluid velocity. This phenomenon is called advection, a term that means passive transport by the moving fluid that contains the substance. Depending on the fluid flow velocity and properties advection appears in forms of dominant mechanical dispersion, imperative molecular diffusion or combination of both processes. Advection could play a significant role in accelerating the mixing process and expanding the interface area between the two miscible fluids. Diffusion process works to homogenize the solvent concentration inside the pore spaces. The process of diffusion is slow and does not have ample time to reduce the local solvent concentration at high velocity. Therefore, mechanical dispersive spreading is the main mechanism of dispersion at high velocity. The mechanisms of mixing in capillaries are relatively well studied. Dispersion in porous media uses the same

mechanisms that are active in capillaries. However, additional mechanisms arise from the fact that the flow taking place in capillaries is non-uniform, has variable cross sections, different conductivity, and many other uncertainties in addition to local velocity variation, and heterogeneous permeability [75]. Dispersion coefficients are used to quantify the mixing during solvent based recovery methods.

1.3.5 Dispersion

Dispersion is a transport mechanism of a substance or conserved property by a fluid due to the fluid's bulk motion [75]. A distinction is commonly made between dispersion occurring in the flow direction, **longitudinal** (D_L), or perpendicular to it, **transverse** (D_T). The Advection Diffusion Equation (ADE), mass conservation law, has been commonly used [8] to describe solute dispersion in two-dimensional porous media:

$$D_L \frac{\partial^2 C}{\partial x^2} + D_T \frac{\partial^2 C}{\partial y^2} - v_x \frac{\partial C}{\partial x} - v_y \frac{\partial C}{\partial y} = \frac{\partial C}{\partial t} \tag{1.2}$$

where C is the solute concentration, t is time, v_x and v_y are the components of flow velocity and D_L and D_T are the hydrodynamic longitudinal and transverse dispersion coefficients, respectively. It must be stated that the advection and diffusion phenomena occur on very different time and length scales. Therefore, it is required to effectively average out the dynamics on smaller/faster scales to determine what is the net effect on the larger/slower scales. Assuming that the advection is nearly periodic in time, this then sets the stage for an averaging process by which the faster scale dependence of the solution can be averaged out, leaving us with an effective equation governing the evolution of the solution over the slower time scales.

Direct measurement of dispersion coefficients is not possible but they can indirectly

calculated knowing the velocity and concentration profile. Laboratory studies regarding dispersion have shown that dispersion coefficients are affected by:

- Fluid properties and process conditions: velocity (v), density (ρ), viscosity (μ)
- Pore properties: pore size distribution, pore and grain shape, permeability

These parameters affect dispersion in different ways. One parameter may increase or decrease the effects of other parameters.

1.3.6 Diffusion

Diffusion in this study refers to molecular diffusion, which is the movement of molecules caused by random molecular motion due to the thermal kinetic energy of the solute from a high concentration region to low concentration region [88]. Momentum is transferred through intermolecular collisions. Hence there is no loss of momentum in the mixture in general. Diffusion coefficients represent the molar flux due to molecular diffusion and the gradient in the concentration (the driving force of diffusion). Diffusion coefficient were first introduced in Ficks law as Equation 1.3 in one-direction (x):

$$J = -D_m \frac{\partial C}{\partial x} \tag{1.3}$$

where J is the diffusion flux, D_m the diffusion coefficient, and C is the concentration. There are three descriptions of the diffusion coefficient including the mutual diffusion coefficient, the self-diffusion coefficient, and the tracer diffusion coefficient [69]. In this thesis, the diffusion coefficient refers to the mutual diffusion coefficient that is denoted by D_m and defines the diffusion of one component in a system. When both the solute and the solvent have simple molecules, the diffusion coefficient can be considered as a constant value during the miscible process. In general, the molecular motion in liquids

is smaller than in gases but larger than in solids [60]. Also, the effective molecular diffusion is smaller in a porous medium than in a bulk fluid because of the collision of molecules with the solid walls of the porous medium and the tortuous pathway. The molecular diffusion coefficient depends on the fluid's properties in a porous medium, but it usually ranges between 10^{-9} and 10^{-11} $m^2 s^{-1}$[60].

1.3.7 Peclet Number

Diffusion and dispersion are two of the mechanisms that may lead to mixing and dissipation of a fluid. On the other hand, dispersion may tend to damp out viscous fingers that may be channel through the miscible slug [66]. Hence, dispersion may be detrimental or beneficial (if it prevents fingering through the miscible zone) therefore it is vital to decouple the effect of dispersion and diffusion. The Peclet number (Pe) is defined as the ratio of the rate of advection (mechanical dispersion) to the rate of molecular diffusion driven by an appropriate gradient and defined as below:

$$Pe = \frac{lv}{D_m} \tag{1.4}$$

where v is the fluid velocity, l is a characteristic length and D_m is the molecular diffusion coefficient. Considering the definition of Peclet number, the higher the velocity, the larger the Peclet number and under this condition mechanical dispersion plays a major role in mass transfer, inversely with a lower Peclet number molecular diffusion is dominant. As the Peclet number is a function of characteristic length, it is used in this study to understand the mass transfer at various scales. Dispersion mechanisms may be divided into four categories as Figure 3.6 and listed below [37]:

1. Zone (I) Pure molecular diffusion or dominant diffusion ($0 \leq Pe \leq 5$): In this region molecular diffusion dominates the dispersion process or if mechanical

dispersion appears, it is on the same order of magnitude as molecular diffusion.

2. Zone (II) Diffusion and dispersion both are acting. Dispersion is dominant ($5 \leq Pe \leq 300$):

3. Zone (III) Pure mechanical Dispersion ($300 \leq Pe \leq 10^5$):

4. Zone (IV) Turbulent flow ($Pe \geq 10^5$): In this region, turbulence affects dispersion. The corresponding fluid velocities are rather large and fall outside the validity of Darcy's Law.

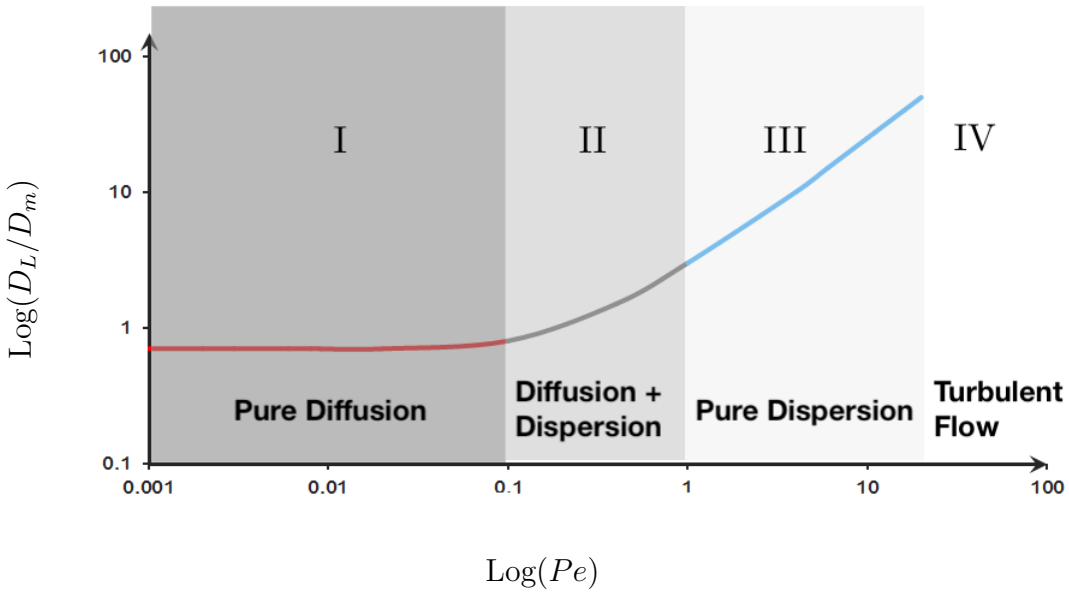

Figure 1.2: Flow regimes for increasing flow velocity [66]

Diffusion causes mixing due to random molecular motions and, on average, particles move from regions of high concentration to regions of low concentration. Diffusion becomes less important at larger fluid velocities as other mechanisms overwhelm diffusion. Variation in fluid properties (density and viscous differences between fluids, saturation levels, and turbulence) cause one fluid to move faster or in different directions than the bulk flow. Fluids may vary simply in viscosity and density. An

important consideration is how easily the different fluids mix; miscible fluids freely mix; immiscible fluids do not mix. This affect appears in the Reynolds dimensionless number. Pore geometry (tortuosity, pore size sorting, dead end pores and recirculation) cause spreading due to the nature and alignment of the pores. Some pores will be longer or wider and will have faster average velocities than others. This causes mixing when the fluid in one pore reaches a downstream location at a different time than the fluid in a different pore. The pore structure may also trap some fluid in a dead end or recirculation zone. These mechanisms may be dominant in cases of anomalous dispersion. Fluid pore interactions (wettability, hydrodynamics, and heterogeneity effects) cause spreading through the pore space. Finally, boundary and initial conditions can skew results when they are not properly described. Entrance and exit affects can cause large changes in fluid velocities and directions over small distances. These effects can be compensated for by measuring actual concentrations around the inlet and outlet. The flux of an individual solute contains contributions from advection and diffusion. This is modelled by including the effect of the local velocity field to Ficks law [62]. Some parameters and coefficients in fluid transport models can be independently obtained from experimental measurements such as recovery factor, permeability, and porosity, etc. However, some parameters, such as the dispersion coefficient, cannot be determined directly [89]. We expect that there are different scaling regimes depending on the Pe number ($\frac{vl}{D_m}$) [20]. This study because of broader coverage of higher velocity displacements, assumes higher Peclet number condition where advection (mechanical mixing) dominates.

1.3.8 Reynolds Number

The Reynolds Number (Re) corresponds to the ratio between inertial and viscous forces and is defined as equation below:

$$Re = \frac{\rho v l_c}{\mu} \tag{1.5}$$

Where ρ is density, v is velocity, l_c is a characteristic linear dimension, and μ is viscosity. For a Reynolds number (Re) below (1) in porous media, the flow regime is classified as laminar and therefore, Darcy's law is valid. The order of magnitude of the characteristic length can be obtained from the absolute permeability (K) and porosity (ϕ) of the medium as below [68]:

$$Re = \frac{\rho v}{\mu}\sqrt{\frac{K}{\phi}} \tag{1.6}$$

In this study, the flow regime is assumed to be laminar and Darcy's law is valid.

1.4 Objectives and Novelty

The purpose of this thesis is to investigate the mass transfer during miscible processes as a function of pore geometry and velocity using novel mathematical and experimental methods. This study uses a combination of mathematical and experimental methods. The significant novelty of this thesis is each approach is as following:

- **Mathematical Part:** This thesis uses a statistical oriented mathematical approach to investigate the miscible displacement process assuming various pore properties to better understand the relationship between dispersion during miscible displacement and pore structure. Previous literature solely studies either

longitudinal or transverse dispersion, the introduced model examines dispersion in both longitudinal and transverse directions and shows a more detailed relationship between dispersion and pore size distribution. The approach improves the processing speed and time for field scale simulations and also covers a broad range of flow velocities and regimes.

- **Experimental Part:** While previous studies use known correlations (e.g., Taylor concentration correlation) to estimate experimental dispersion coefficients, this thesis utilizes a unique method to estimate the mass transfer properties. The novel image processing tool is developed and used to analyze the developing mixing zone in the process, and consequently processed images are used to collaborate with a developed Bayesian estimator tool to fit the dispersion coefficients in analytical solution of Advection-Diffusion Equation (ADE).

1.5 Thesis Structure

Efficient oil production and conservation requires a good knowledge of the fluid displacement in a porous environment. In the following, the thesis provides the fundamentals of geology, science and mathematics. Such is the scope of the thesis. The specific problems within its proper field are almost unlimited in number, and hence it is necessary to make a reasonable preference to include typical problems of interest from a practical point of view, as well as to illustrate the various mathematical and experimental methods that may be used in the thesis. The problems considered involves miscible fluids and homogeneous non-uniform porous media.

- **Chapter 1** gives a brief introduction to objective, motivation, structure of the study and basic principals of the study.

- **Chapter 2** presents a review of existing literature on experimental and mathematical studies of miscible processes. Previous studies models are summarized in a table at the end of this chapter.

- **Chapter 3** explains the developed mathematical and experimental methodologies in this study in details. The mathematical models are developed to model the effect of pore geometry on key factors within miscible processes. In this chapter, the unique developed image processing technique is explained as well. explains all three of the mathematical approaches including statistical, numerical and analytical in detail and the methodology for analyzing the results is presented. The mathematical models are developed to model the effect of pore geometry on key factors within miscible processes.

- **Chapter 4** includes the mathematical and experimental results of the miscible processes using a 2D glass micromodels. This chapter also explains and analyze the effects of several parameters including pore structure properties on dispersion coefficients. And in the following,

- **Chapter 5** includes conclusions and outlines proposed future work.

This study attempts to address specific questions regarding miscible processes that are not yet well characterized or understood:

- How is miscibility affected by the heterogeneity of a porous medium during miscible displacement process?

- How is dispersion dependent on pore geometry and what is its physical interpretation?

- What is the effect of mathematical moments of pore throat size distribution function on longitudinal and transverse dispersion coefficients?

- What are the deficiencies of the most widely used models in predicting dispersion of miscible process?
- How do the dominant forces, including mechanical dispersion and molecular diffusion, change by injection rates and pore geometry?

The main objective of this study is to attempt to overcome the inadequacies observed in the existing models to answer the questions above.

Chapter 2

Literature Review

In this chapter, the existing literature from previous studies on mass transfer in miscible displacement is reviewed. The main goal in this chapter is to summarize the existing dispersion models and their validity. The literature survey is divided into experimental and mathematical studies. Since dispersion is scale dependent, in both categories different scales of studies are considered. Dispersion in porous media involves mechanical dispersion (advection) and diffusion, and it is complicated to model because of its dependence on a wide range of parameters, e.g., pore geometry, fluid properties and, pore-fluid properties [58]. Dispersion in the past has been studied by many researchers from either theoretical or an experimental point of view. Generally speaking, mathematical modeling efforts can be classified as stochastic and deterministic. In either approach, a distinction has been made between longitudinal and transverse dispersion because of inequality.

2.1 Mathematical Studies

Mass transfer due to advection in porous media continues to be of considerable interest in the past and recent years. In various fields of science such as pure mathematics,

chemistry, and biology, and applied science areas such as chemical engineering applications in hydrology, waste management, cosmetics and pharmaceutical industry, or petroleum engineering such as secondary oil recovery from oil reservoirs, oil adsorption processes in downstream industry and more, dispersion and mass transfer have been studied. Depending on the field of the interest different aspects of the process have been focused on and analyzed [73]. The mathematical approach to modeling advection regularly focused on applying the partial differential equation referred to as the Advection-Diffusion Equation (ADE) from continuum mechanics [9]. Advection is mainly characterized by contributions of molecular diffusion and mechanical dispersion expressed as a function of the Peclet number. Many mathematical models including imperial correlations have been studied and proposed over the years. Some of the notable advances include the following. Taylor [87] in 1954 described the principles of solute transport in porous media. He envisioned the porous media as a bundle of capillaries and viscous fluid flowing through a tube of a circular cross-section. Taylor defined dispersion D $(m^2 s^{-1})$ as:

$$D = \frac{a^2 v^2}{48 D_m} \tag{2.1}$$

where a is the radius of the tube (m), v is the velocity (ms^{-1}) and D_m is the molecular diffusion $(m^2 s^{-1})$. Taylor [87] showed that the proposed model was valid when $6.9 \ll Pe \ll \frac{4l}{a}$. Aris [6] in 1956 removed the limitation imposed on some of the parameters at the expense of describing the distribution of the solute in terms of its moment in the direction of flow. Aris also showed that the rate of growth of the variance is proportional to the sum of molecular diffusion and Taylor dispersion [6]. Coats and Smith [23] in 1964, Hoopes and Harleman [45] in 1967, and Brigham [12] in 1986 used Taylor's assumptions and approach to study different physical aspects,

Table 2.1: Contributions and gapsof the statistical study of Taylor (1954) [88] and Aris (1956) [6]

Researcher	Study Type	Contributions	Gaps
Taylor [88] and Aris [6]	Statistical	Introduced the first statistical concept	Longitudinal and transverse dispersion are not decoupled

such as pore heterogeneity and its effects on dispersion. Studies by De Josselin de Jong [51] in 1958 and Saffman [74] in 1959 employed same statistical techniques as Taylor [87] and Aris [6] and built models for longitudinal and transverse dispersion as separate, yet coupled, processes. These studies assumed a porous medium as a series of interconnected, randomly oriented, and uniformly distributed straight tubes of equal length and diameter. Saffman [74] and De Josselin de Jong [51] proposed separate models for longitudinal and transverse dispersion coefficients as below, that are valid when the diffusion is negligible. Equations 2.2 and 2.3 show the proposed models by Saffman and De Josselin, respectively.

$$\text{Saffman's Model}: \begin{cases} \frac{D_L}{D_m} = \frac{Pe}{6}\big(\ln(\frac{3}{2}Pe) - \frac{1}{4}\big), \quad \text{where } Pe = \frac{lv}{D_m} \\ \frac{D_T}{D_m} = \frac{3}{16}Pe, \end{cases} \tag{2.2}$$

$$\text{De Josselin's Model}: \begin{cases} D_L = vl\big(\frac{\lambda+3/4-\ln\lambda}{6}\big), \quad \text{where } Pe = \frac{lv}{D_m} \\ D_T = \frac{3vl}{16}, \end{cases} \tag{2.3}$$

In the Equation 2.3, parameters λ and γ are variables. The dispersion models proposed by Saffman indicate that both components are proportional to the mean velocity of fluid flow. Based on Saffman's and also De Josselin's model, the ratio between longitudinal and transverse dispersion is not constant and increases over the distance

traveled. Schematic of assumed flow through a random porous medium in De Josselin de Jong (1958) [51] and Saffman (1959) [74] studies as been shown in Figure 2.1. As this figure shows, the Newtonian flow passes through randomly selected pathways in a porous medium with different length, angle, and diameter. Haring and Greenkorn

Table 2.2: Contributions and gapsof the statistical study of De Josselin De Jong (1958) [51] and Saffman (1959) [74]

Researcher	Study Type	Contributions	Gaps
De Josselin De Jong (1958) [51]	Statistical	Modelled a pore system of a packed bed by a system of canals	Pore properties (except l pore- throat length) are not taken into account
Saffman (1959) [74]	Statistical	Modelled the micro-structure of a porous media as a network of capillary tubes of random orientation	Pore Size Distribution (PSD) is assumed to be normal and uniform

[42] in 1970 employed a statistical approach to obtain a model for dispersion in non-uniform porous media. They assumed a beta function as a distribution function for pore throat length and diameter and followed the same procedure by Saffman. Haring and Greenkorn concluded that dispersion is a function of the non-uniformity of the porous medium even though tortuosity and resistance are constant. Koch and Brady [54] in 1985 developed a model (Equation 2.4) for calculating the longitudinal dispersion in a disordered medium, within a range of $5 \leq Pe \leq 300$.

$$\frac{D_L}{D_m} = 1 + \frac{3}{8}Pe + \frac{\pi^2}{20}Pe\ln(\frac{Pe}{2}) \tag{2.4}$$

Buyuktas and Wallender [15] in 2004 applied the method of volume averaging to ordered and disordered spatially periodic porous media in two dimensions and proposed Equation 2.5 to compute the components of the longitudinal dispersion tensor for low

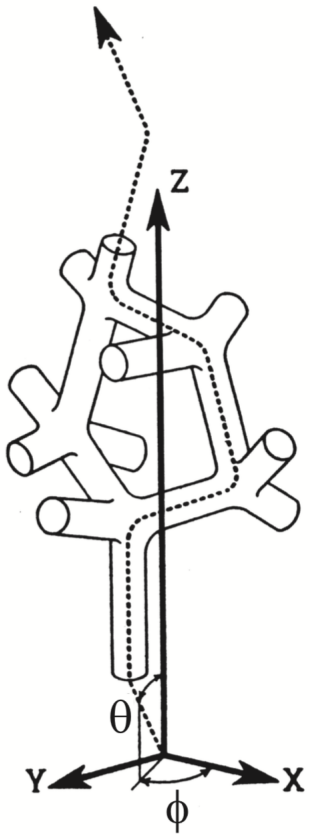

Figure 2.1: Schematic of assumed flow through a random porous medium. Modified from De Josselin de Jong (1958) [51] and Saffman (1959) [74]

Peclet numbers ($0.1 \ll Pe \ll 100$).

$$\frac{D_L}{D_m} = 0.026 Pe^{1.854} \tag{2.5}$$

This study showed that the longitudinal dispersion coefficient decreased with an increase in disorder while the longitudinal dispersion coefficient increased. Further, the longitudinal and transverse dispersion coefficients are independent of Reynolds number and depend only on Peclet number [58]. Most of the mathematical and computational studies in 3D use random network approaches to model flow through porous

media too. Continuous Random Walk Theory (CRWT) is an attractive approach as well that is used and implemented to solve the ADE by many researchers. One of the latest studies by Sahimi (2012) [76], applied this approach to the modeling of anomalous (non-Gaussian) dispersion in flow through heterogeneous porous media. The results were consistent with experimental data, both at the laboratory and field scales, however this study does not take pore properties into account.

Table 2.3: Contributions and gapsof the statistical studies of Hearing, Greenkorn (1970) [37], Koch and Brady (1985) [54], Buyuktas and Wallender (2004) [15] and, Sahimi (2012) [76]

Researcher	Study Type	Contributions	Gaps
Hearing, Greenkorn (1970) [37]	Statistical	Introduced non-uniform Pore Size Distribution (PSD) (β-function)	Not valid for other PSD functions.
Koch, Brady (1985) [54]	Numerical	Identified the underlying physical mechanisms of dispersion	Calibrated by curve-fitting method from limited outputs of experimental studies. Pore properties are not taken into account.
Buyuktas, Wallender (2004) [15]	Continues Random Walk Theory (CRWT)	Volume averaging method has been applied to ordered and disordered spatially periodic porous media	Calibrated by experimental results of field scale studies. Not valid for micro and macro scale. Pore properties are not taken into account.
Sahimi (2012) [76]	Analytical	Introduced anomalous (non-Gaussian) dispersion in flow through heterogeneous porous media	Pore properties are not taken into account.

2.2 Experimental Studies

Mixing processes that occur during miscible or near-miscible injection have been studied at different scales, from the laboratory to field scale, using various experimental approaches. One of the initial leading studies was published by Brigham et al. [13]

(1961) and describes the result of experiments on miscible displacement in various porous media. Both glass bead packs and natural cores were used to represent the porous media. Since the required experimental parameters were not directly measurable, appropriate assumptions were made to obtain such values by Brigham. After analyzing the error function, he proposed Equation 2.6 to calculate the longitudinal dispersion.

$$D_L = \frac{1}{t}\left(\frac{x_{90} - x_{10}}{3.625}\right)^2 \tag{2.6}$$

where t is time in s and x_{10} is defined as the distance to the point of 10% displacing fluid and x_{90} is the distance to the point of 90% displacing fluid. However, Brigham related the dispersion coefficient to the error function by drawing the best straight line through the data points values of U (the error function parameter). The modified equation based on this method is given in Equation 2.7 as:

$$\begin{cases} D_L = \frac{1}{V_P T}\left(\frac{L(U_{90}-U_{10})}{3.625}\right)^2 \\ with\ U = \frac{V_P - V}{\sqrt{V}} \end{cases} \tag{2.7}$$

where V_P is the pore volume of the porous medium in cm^3 and V is the volume of the recovered fluid at the time in cm^3. Figure 2.2 shows the logic behind the correlation 2.6 when U is plotted against the percentage of displacing fluid on arithmetic probability coordinates and provided the advection-dispersion model holds, a straight line results. This investigation showed that the viscosity ratio during displacement and flow velocity greatly affects dispersion rate. For transverse dispersion, Grane and Gardner [36] (1961) carried out a series of experiments in homogeneous porous media media to study the influence of fluid flow velocity and pore structure properties on transverse dispersion. These experiments consisted in keeping a constant fluid velocity, 0.02 m/s and increasing the difference in density up to 10%. Porosity

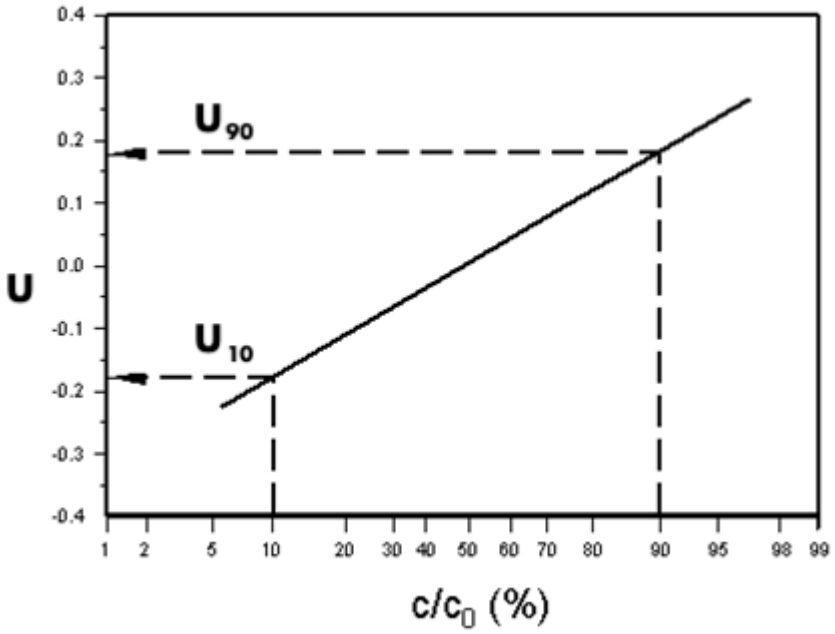

Figure 2.2: Introduced probability plot for determination of longitudinal dispersion coefficient (D_L) by Brigham et al. (1961) [13]

is reported to be around 40% for an average grain diameter 1.5 mm, molecular diffusion $D_m = 1.2 \times 10^{-9}\ m^2/s$, viscosity $\mu = 1.38 \times 10^{-3}\ Pa.s$ and permeability is calculated using the Carmen-Kozeny relationship yielding $K = 2.2 \times 10^{-9}\ m^2$. They observed that by increasing the difference in density, mechanical dispersion significantly decreased and therefore the density difference has significant effect. Perkins and Johnston [66] (1963) performed experimental investigations using the Brigham method. They studied the impact of various parameters including density contrast and pore geometry. Fried and Combarnous [33] (1971) published the result of fairly extensive laboratory experiments to investigate the influence of the increase in velocity on dispersion in porous media. Most of the later experimental studies applied the same methodology as Brigham (1961) [13] to refine the understanding of longitudinal and transverse mixing and effective parameters by directly considering the physical mechanisms governing solute transport. For instance, systematic measurements of the

Table 2.4: Contributions and gapsof the experimental studies of Brigham et al. (1961) [13], Grane and Gardner (1961) [36], Perkins and Johnston (1963) [66] and Fried and Combarnous (1971) [33]

Researcher	Medium	Contributions	Gaps
Brigham (1961) [13]	Glass bead packs	Introduced the first experimental estimation model for calculation of dispersion coefficient	Only studied longitudinal dispersion, the linear estimation was not accurate enough
Grane, Gardner (1961) [36]	Glass beads packs	They investigated turbulent rates of flow and measured the steady-state distribution due to a point source in a cylindrical fluid stream	Only studied the transverse dispersion coefficient, assumed the transverse dispersion is independent of flow rate, whereas longitudinal dispersion increases significantly with flow rate in the same range
Perkins, Johnston (1963) [66]	Packs of granular material	Studied the effect of particle diameter to column diameter and studied wider range of velocity	All calculations were based on Brigham et al., The theoretical were not validated with any experimental results.
Fried, Combarnous (1971) [33]	Field scale- Soil	Studied the effect of presence of sodium on dispersion coefficient in soil and sulphate	The quatified results were all estimated using the same method as Brigham et al. Only longitudinal dispersion has been studied.

longitudinal dispersion coefficient have been done by Ujfaludi [90] (1986) in uniform and non-uniform porous media. Analysing results from both types of media, they concluded that irregular dispersion arises from the irregular pore size distribution of the non-uniform samples. Hassanizadeh and Leijinse [43] (1990) carried out vertical displacement experiments in homogeneous columns. In these experiment, fresh water

was displaced by a high concentration brine. Hassanizadeh concluded that the longitudinal dispersion coefficient decreases with increasing concentration difference and also non-linear behaviour was observed as well. By displacing the brine by another brine with approximately the same density (concentration) the author showed that the difference in dispersion plays a major role when the density contrast is not significant. Hassanizadeh et al. [44] (1995) completed this study and accentuated that the observed non-linearity and deviations from the classical Ficks law was not caused by heterogeneity as their study involved the use of homogeneous column systems. However, due to the small number of experimental runs, no statement was made on the dependence of non-linearity on fluid flow velocity. Later on, Nick et al. [39] (2009) completed this study by further investigations and revealed that the main cause of the non-linear behavior in dispersion, which is the interaction between density contrast and vertical velocity, needs to be explicitly accounted for in a macro-scale model. More recent experimental studies include using slices and casts of rock in an attempt to make more realistic models of pore space. For example, core flooding has been used to obtain relative permeabilities, dispersion coefficients, and relevant hydraulic variables [81]. For general summaries, two studies particularly provide satisfactory summaries of the various approaches to current micromodel design and fabrication. Buckley [14] (1992) revealed the successes and limitations of micromodels in illustrating mechanisms of multiphase flow, while Dawe et al. [67] (1987) highlight pore scale events which depend on network and pore morphology. Watson et al. [92] (2002) showed velocity dependency of deviation from Fick's law by analysis of constant density contrast experiments that velocity varies. Sternberg [84] (2004) carried out experiments to confirm the significant impact of heterogeneity on dispersion. The experimental observations indicated that heterogeneity plays a major role in macro-scale dispersion during miscible fluid injection. A series of experiments were carried

Table 2.5: Contributions and gapsof the experimental studies of Ujfaludi (1986) [90], Hassanizadeh and Leijinse (1990, 1995) [43][44], Watson et al. (2002) [92], Sternberg (2004) [84], Starke and Koch (2006) [83], Fayazi et al. (2015) [30]

Researcher	Medium	Contributions	Gaps
Ujfaludi (1986) [90]	Glass bead packs	Uniform and non-uniform media were studied using Brigham et al. method	Only longitudinal dispersion was studied, one dimensional study
Hassanizadeh and Leijinse (1990, 1995) [43][44]	Plexiglas cylinder	A non-linear theory of dispersion has been suggested	Uniform porous medium only has been studied, only longitudinal dispersion was studied, one dimensional study
Sternberg (2004) [84]	Glass bead packs	Heterpgeneity and pore properties affect the dispersion coefficient	One-Dimensional study, dispersion coefficients have not been calculated, quantitative analysis have not been conducted
Starke and Koch (2006) [83]	Plexiglas tank	Studied the interplay between porous media heterogeneity and density contrast on transverse dispersion	Only transverse dispersion was studied, one dimensional study
Fayazi et al. (2015) [30]	Micromodel	Compared the experimental results with simulated CRWT outputs	Length of the mixing zone has been assumed constant for all conditions, calculations of the experimental dispersion coefficients have not been explained

out by Starke and Koch [83] (2006) to study the interaction between heterogeneity and difference in density on transverse macro dispersion. Fresh water and brine were used as a fluid system. They concluded that dispersion increased with increasing heterogeneity and decreasing density contrast, but the effect of density difference was

reported to be much higher. Fayazi et al. [30] (2015) performed micromodel experiments to validate numerical simulation results using the Continuous Random Walk Theory (CRWT) approach. This study showed good agreement between model results and experimental data indicating that CRWT is an accurate method for simulating miscible displacements.

2.3 Summary of Review

Solute dispersion during fluid flow in porous media has attracted interest since the early years of the 19^{th} century, but it was only since 1950 that the general subject of dispersion or miscible displacement turned into the topic of more study. This subject has intrigued hydrologists, geophysicists, petroleum, and chemical engineers to study the miscible phenomenon. The literature review of miscible injection process including investigation of longitudinal and transverse dispersion shows that however this process has been well established concerning both mathematical and experimental concepts, yet a lack of understanding persists due to the complex dependency of this process to a variety of parameters. Inhwan Park (2018) [48] summarized the mixing scenarios in two-dimensional studies in hydrology in Figure 2.3. As it is shown from the different point of views the mixing zone spreads the different velocities over the depth in both the longitudinal and transverse directions. Figure 2.3 (a) shows miscible displacement in porous media in the intermediate mixing region where the Re number is lower than unity ($Re \leq 1$) leading to the completion of transverse mixing. This study considers co-existence of longitudinal and transverse dispersion at the same time. In this mixing process as it is shown in Figure 2.3 (b) and (c) the displacing fluid column stretched due to variation in velocity in both the longitudinal and transverse directions. In the following, the displacing fluid is widely dispersed and

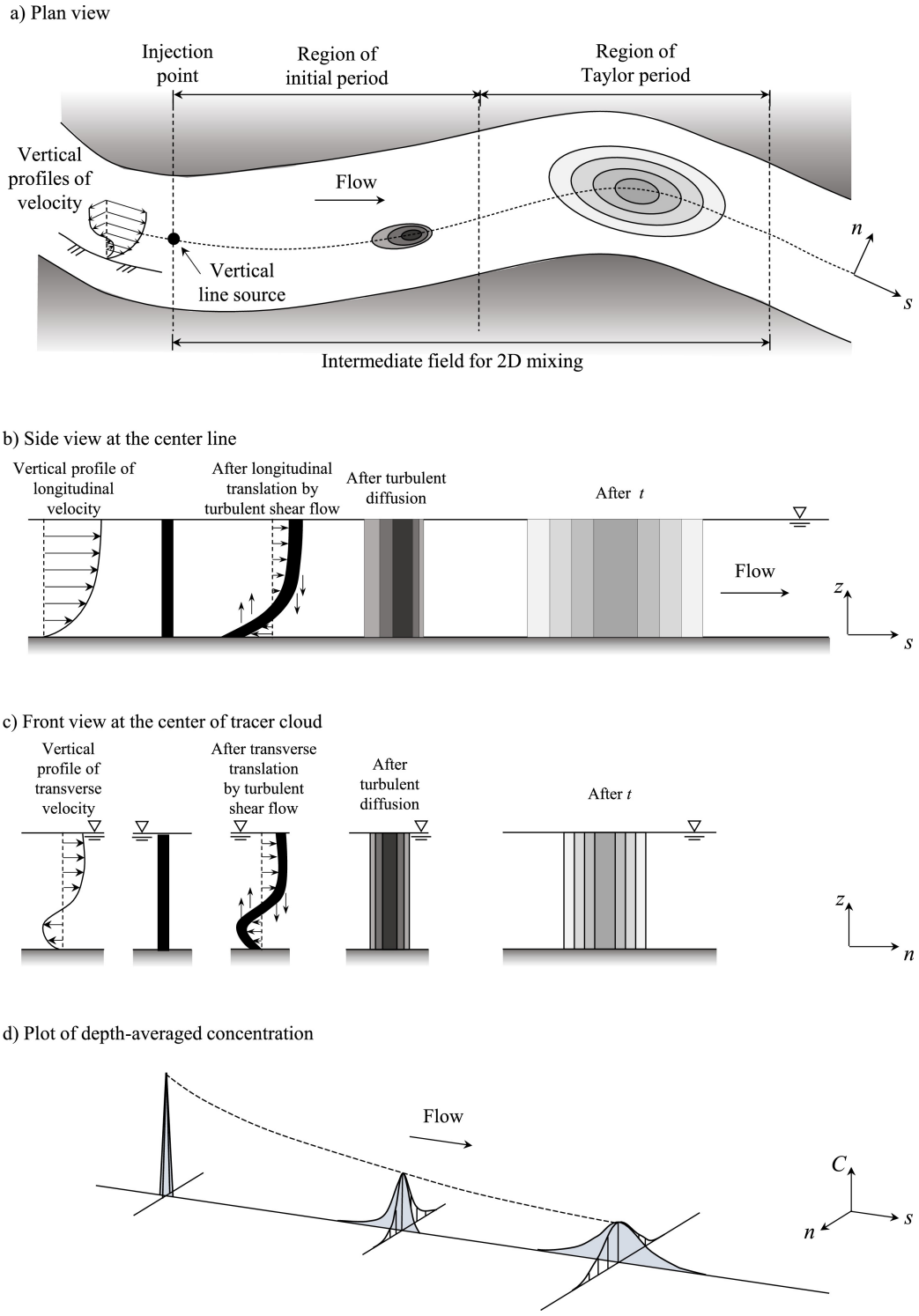

Figure 2.3: Schematic diagram of the dispersion mechanism in two-dimensional

mixing zone spreads as it is shown in 2.3 (d). Among the various mixing mechanisms, the mechanical dispersion due to velocity profile is assumed the most important factor in this study. A summary of previous studies of longitudinal and transverse dispersion and the effect of density contrast, fluid flow velocity, and porous media heterogeneity (proportional) is presented in this chapter. Table 2.3 illustrates a number of proposed models for dispersion in porous media including assumptions and the valid range. Considering the experimental literature review, the current study uses an unique methodology to cover the lack of coupled longitudinal and transverse dispersion in experimental studies. However, there is still room to improve the current methodology. The contributions and persisting gaps of the developed method in this thesis are listed in Table 2.6.

Table 2.6: Contributions and gaps of the used experimental methodology in micro-model study

Contributions	Gaps
1- Uniform and non-uniform media are studied	1- Density contrast is not considered
2- Two-Dimensional porous media is studied	2- Molecular diffusion is assumed negligible
3- Coupled longitudinal and transverse dispersion coefficients are calculated	
4- Advanced image processing technique are implemented to take advantage of pixel-level accuracy	
5- More adjustable parameters such as pore diameter, pore- throat length and orientation are implemented to tune the method and improve accuracy	
6- The proposed technique can be developed for a broader range of Peclet number	
7- The technique can be developed for heterogeneous porous media	
8- Parallel calculations potential in statistical estimation to decrease the processing time significantly lower than analytical and numerical simulations	

Author	**Study**	**Type of media**	**Remarks**
Taylor; Aris, 1953, [6, 88]	Mathematical	Capillaries of length l and radius a	$\frac{D_L}{D_m} = 1 + \frac{Pe^2}{48}$ $6.9 \ll Pe \ll \frac{4l}{a}$
Danckwerts, 1953, [24]	Experimental	Raschig rings	Data point agree with F curve derived from dispersion model
Kramers, 1953, [55]	Experimental	Raschig rings	Mixing of the liquid is increasing with liquid velocity
Carberry, 1958, [17]	Experimental	Glass spheres	Significant bed height effect for bed of less than 0.6m in length
Saffman, 1959, [74]	Mathematical	Capillaries of length l and radius a	$\frac{D_L}{D_m} = \frac{Pe}{6}(\ln(\frac{3}{2}Pe) - \frac{1}{4})$ $Pe \ll 8\frac{a}{l}^2$
Blackwell et al., 1959, [10]	Mathematical	Packed bed of sand	$\frac{D_L}{D_m} = 8.8Pe^{1.17}$ $Pe \geq 0.5$
Gunn, Pryce, 1960, [38]	Mathematical	Random packing of spheres	$\frac{D_L}{D_m} = 0.7Pe^{1.2}$ $Pe \geq 1$

Stoyanovskii, 1961, [49]	Experimental	Sand and glass bead packs	D_L is proportional to velocity and pore diameter and decreases with increasing dispersion. No effect of length, rate and surface tension of the fluids was introduced.
Perkins, 1963, [66]	Mathematical	Unconsolidated sand of bead packs	$\frac{D_L}{D_m} = 0.701 + 1.75Pe$ $2 < Pe < 10^2$
Miyauchi, 1975, [63]	Experimental	Glass spheres	Dispersion data in the stokes flow regime presented
Carbonell, 1979, [70]	Mathematical	Array of parallel pores	$\frac{D_L}{D_m} = 1 + 0.57Pe + 0.033Pe^2$ $Pe < 10^2$
Eidsath et al., 1983, [29]	Mathematical	In-line array of cylinders	$\frac{D_L}{D_m} = 0.7Pe^{1.7}$ $10 \leq Pe$
Koch and Brady, 1985, [54]	Mathematical	Randomly packed fixed beds	$\frac{D_L}{D_m} = 1 + \frac{3}{8}Pe + \frac{\pi^2}{20}Pe\ln(\frac{Pe}{2})$ $5 \leq Pe \leq 300$
Han et al., 1985, [41]	Experimental	Glass beads	For beds of uniform particles, dispersion is strong function of packing

Edwards, 1991, [25]	Mathematical	Staggered arrays of cylinders	$\frac{D_L}{D_m} = 0.174Pe^{1.76}$ $10 \leq Pe$
Edwards, 1991, [25]	Mathematical	Hexagonal arrays of cylinders	$\frac{D_L}{D_m} = 0.032Pe^{1.66}$ $10 \leq Pe$
Sahraoui, 1994, [77]	Mathematical	In-line array of cylinders	$\frac{D_L}{D_m} = 0.048Pe^{1.71}$ $10^{-2} \leq Pe \leq 10^3$
Sahraoui, 1994, [77]	Mathematical	Staggered arrays of cylinders	$\frac{D_L}{D_m} = 0.018Pe^{1.26}$ $10^{-2} \leq Pe \leq 10^3$
Delgado, 2001, [26]	Experimental	Glass beads	Influence of Schmidt number on longitudinal dispersion
Buyuktas, 2004, [16]	Mathematical	In-line array of discs	$\frac{D_L}{D_m} = 0.026Pe^{1.854}$ $10 \leq Pe$
Buyuktas, 2004, [16]	Mathematical	Random array of discs	$0.0924Pe^{1.356}$ $10 \leq Pe$
Freund et al., 2005, [32]	Mathematical	Structured cubic sphere array	$\frac{D_L}{D_m} = 0.719 + 0.0345Pe^2$ $0.2 \leq Pe \leq 3000$
Freund et al., 2005, [32]	Mathematical	Randomly packed fixed beds	$\frac{D_L}{D_m} = 0.790 + 0.303Pe^{1.21}$ $5 \leq Pe \leq 300$

Wood, 2007, [7]	Mathematical	In-line array of spheres	$\frac{D_L}{D_m} = 0.763 + 0.22Pe^{1.17}$ $Pe \leq 5000$
Alkindy et al.[4] (2010)	Mathematical	Glass of bead packs	$\frac{D_L}{D_m} = 0.63 + 0.077Pe^{1.2}$ $10^{-2} \leq Pe < 10^4$
Golfier et al., 2011, [34]	Experimental	Glass flow cell column	Low permeability contrast is not a sufficient criterion to establish displacement.
Scheven, 2014, [79]	Mathematical	Random particle packs	$\frac{D_L}{D_m} = 0.77 + 0.01Pe + 0.0145Pe\ln(Pe)$ $1 \leq P$
Majdalani et al., 2015, [61]	Experimental	Tracer in sand column	Scale sensitivity of dispersion has been investigated and observations show strong dependency. High resolution sampling improves the accuracy of the result

Table 2.7: Summary of mathematical and experimental dispersion models including validity range of Peclet number and assumed porous media since 1953 [59]

Chapter 3

Methodology

Transport phenomena in porous media have been extensively well examined, using different concepts and approaches. The fundamental transport properties are important parameters with an application in the groundwater hydrology, filtration in processes towers, enhanced oil recovery (EOR), and more. As discussed in the literature review, the geometry and topology of the porous media control transport properties, e.g., dispersion and permeability [75], thus characterization of the porous media in this study is vital. In this study a statistical approach is developed to model the dispersion in two-dimensional porous media. Also, an anlytical modeling that is used in the image processing tool for the experimental investigation has been explained in details. In the following the numerical simulation as an alternate methodology is developed to be utilized in computational simulation of the experimental work.

3.1 Mathematical Development

A porous medium can be defined and classified according to its pore geometry and structure, considering this character, the porous medium is defined to be either homogeneous or heterogeneous at the macroscopic level. Properties at the macroscopic

level are averaged over a sufficiently large volume, called the macroscopic volume averaging, to define continuous, stable functions of spatial position [8]. A homogeneous medium contains two subcategories uniform or non-uniform. A uniform homogeneous medium with has the same pore size and shape distribution, whereas a non-uniform porous medium contains variations at the microscopic scale, yet is homogeneous at the macroscopic level for parameters such as the permeability or porosity [51]. A porous medium is also either isotropic or anisotropic at the macroscale. In an isotropic porous media properties do not vary with direction; in anisotropic porous media properties vary directionally [31]. The transport phenomena are dependent on the type of medium. The porous media studied in this work is a homogeneous, non-uniform, anisotropic porous medium, shown by light gray color blocks in Fig 3.1. However, even heterogeneous porous media is often modeled as a homogeneous media with an overall mean flow direction and macroscopic dispersion coefficient, since data on the exact nature of the heterogeneities are usually not available [86]. Scales of interest associated with porous media may vary from the molecular level (on the order of μm) to a mega level (Km). Modelling fluid flow at the pore scale can provide a predictive tool for estimating rock and flow properties at larger scales and serve as a platform to study the physics of transport phenomena in porous media.

In the current study, a statistical approach has been applied at the pore level to find the describing models for the coupled longitudinal and transverse in a randomly generated model. The main benefits of statistical approach is listed in the following:

- The most natural and biological phenomena, such as solute transport in porous media, show variability which can not be modeled using deterministic approaches. There is evidence in natural phenomena to imply that some observations cannot be explained using deterministic approaches. Stochastic methods have a rich repository of objects which can be utilized to represent the randomness

integrated into the system and the development of the system over time.

- The statistical methods lead to a stochastic remodeling of porous media in three dimensions based on statistical information acquired from one or several two-dimensional images of thin sections of the actual material. This application can help advanced computational methods (higher accuracy and resolution, yet faster processing) where the computational procedure tries to imitate the physical processes that commence during the formation of the medium.

- Transport processes are usually modeled by initial and boundary value problems for a Partial Differential Equation (PDE) describing the regional balance of the concentration fields. However, during probabilistic analysis of flow and transport properties in porous media, the uncertainties due to spatial heterogeneity of governing parameters will often be taken into account. The definition of the characteristics of porous media in space and time using the concept of random functions enables studying the built-in heterogeneity, evaluating the spatial variability of the properties, and estimating the uncertainty associated with their estimated values.

We prove that the introduced model can describe the strong dependency of the dispersion displacement to pore geometry factors including pore throat length, orientation and size distribution. The digital reconstruction of porous materials is a relatively new, powerful methodology that enables the reliable representation of the complex structure induced by porosity. The introduced model is a reliable mathematical approach to study flow at the micro-scale to predict averaged macroscopic properties of porous media that are not possible or difficult to obtain experimentally.

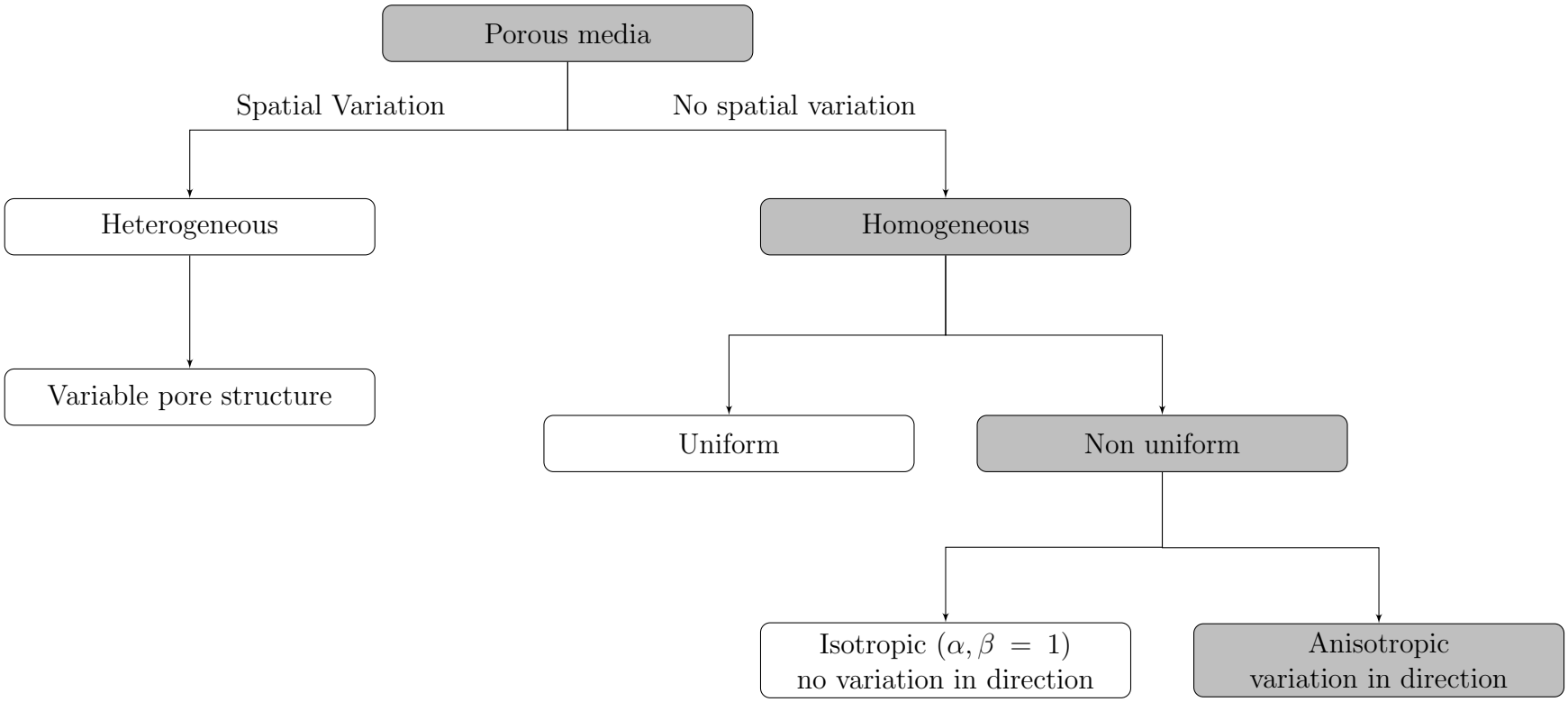

Figure 3.1: Classification of porous media based on pore geometry, α and γ are adjustable parameters for defined function of pore size distribution in Section 3.2

3.2 Characterization of Porous Media

The probabilistic concept used in this study, conceptualizes porous media as an interconnected network of randomly orientated straight capillaries characterized by a probabilistic pore throat length (l) and pore throat diameter (R) density functions and orientation respect to flow direction (θ), starting and ending in each intersection. A marked particle in this model moves along a random succession of straight independent steps through capillaries, of variable directions and distances as indicated in Fig 3.2. We assume that the pore diameter and pore length vary independently and randomly according to their respective frequency distributions. It is assumed that the diameter, length and orientation of pore elements are independent. Various

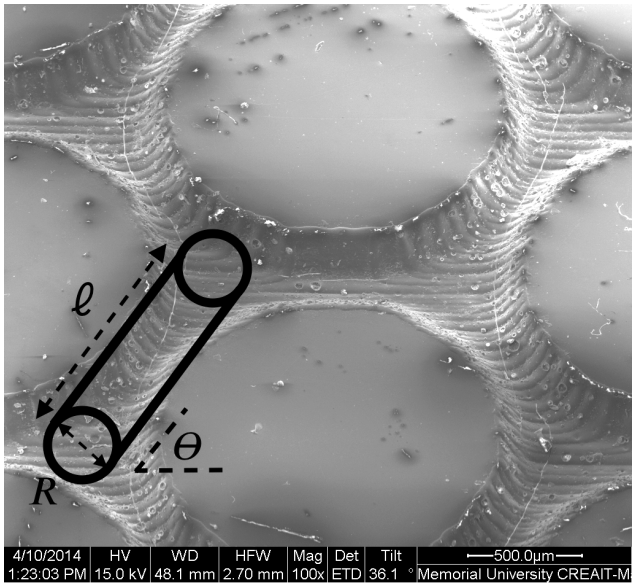

Figure 3.2: Assumed porous media as an interconnected network of randomly orientated straight capillaries characterized by a probabilistic pore throat length (l) and pore throat diameter (R) density functions and orientation respect to flow direction (θ), starting and ending in each

probability density functions (PDFs) could be considered for R and l. As discussed in literature review, Haring and Greenkorn (1970) assumed a beta function for non-uniform porous media parameters [42]. In this study, the general form of $f(R)$ and

$g(l)$, shown in equation 3.1, are assumed for the pore throat diameter and length.

$$\begin{cases} f(R) = \alpha\beta^{\gamma} R^{\gamma-1} e^{-(R\beta)^{\gamma}}, \\ g(l) = \alpha\beta^{\gamma} l^{\gamma-1} e^{-(l\beta)^{\gamma}}, \end{cases} \tag{3.1}$$

Parameters α, β, and γ are adjustable. Equation 3.1 is one of the Kernel functions in Bayesian statistics. This model is chosen for three reasons. 1) it is a continuous probability distribution so it covers the range of pore sizes, 2) the function shows the probability that any real observation will fall between two real limits of minimum and maximum pore sizes, which means the curve approaches zero on either sides of the function. 3) the Gaussian distribution is immensely useful because of the central limit theorem. The central limit theorem states that, under mild conditions, the mean of many random variables independently drawn from the same distribution is distributed approximately normally, irrespective of the form of the original distribution. Parameters α , β, and γ are adjustable and positive parameters that we can relate to the pore geometry which is under investigation in this study. The acceptable interpretation for the physical significance of α, β, and γ is their relevance to pore entry pressure (α), the pore throat (β) and the pore size sorting (γ), respectively [52]. In this model, if we assume $\alpha = 1$, $\beta = \frac{1}{\sqrt{2}}$, and $\gamma = 2$, the model will converge to Gaussian normal distribution.

3.2.1 Adjustable Parameters α, β, and γ

The PDF model relates adjustable parameters α, β, and γ to the pore geometry such as porosity, permeability, pore sorting, totuosity, and aspect ratio. The presented functions can describe a wide variety of distribution features by tuning the adjustable parameters. The parameter α is related to entry pressure. When the pore size goes

to infinity (capillary pressure goes to zero) parameter α approaches zero (pipe flow). Parameter β is the second moment of PDF related to pore-throat geometrical factor that effects the mechanism of displacement. Since β is related to second moment of PDF, we can relate β to the permeability- porosity ratio and tortuosity that is affected by pore shape. The size and shape of the pores and their packing density affect the β factor. With decreasing particle size or packing density, the pore and throat sizes, as well as their variation increase. A general correlation exists between the size and shape of the pores. The larger the pore size relative to the particle size, the more spherical the pore shape. This correlation, however, becomes weaker as packing density decreases. The connectivity between pores is represented by throat size and channel length. With decreasing packing density, the throat size increases and the channel length decreases. Considering this, we can describe the dimensionless parameter β as Equation 3.2:

$$\beta = \frac{\beta'}{\sqrt{\frac{K}{\phi}}} \tag{3.2}$$

where K is the absolute permeability and ϕ is total porosity of model. Equation 3.2 shows that the parameter β is directly related to porosity (Φ), and permeability (K), and indirectly related to tortuosity. Figure 3.3 illustrates the effect of β on the shape of the PDF curve. Parameter γ illustrates the effect of pore sorting. the Pore size distribution for different values of γ are illustrated in Figure 3.4. Sorting refers to the uniformity of grain size, i.e. a well sorted sediment has similar grain sizes. Particles are sorted on the basis of density due to the energy of the transporting medium. Parameter γ is believed to be highly influential with respect to transport mechanism as it represents heterogeneity. The proposed function has a wide variety of flexibility to match with the most common pore size distribution functions such as normal, log-normal and power-law PDFs.

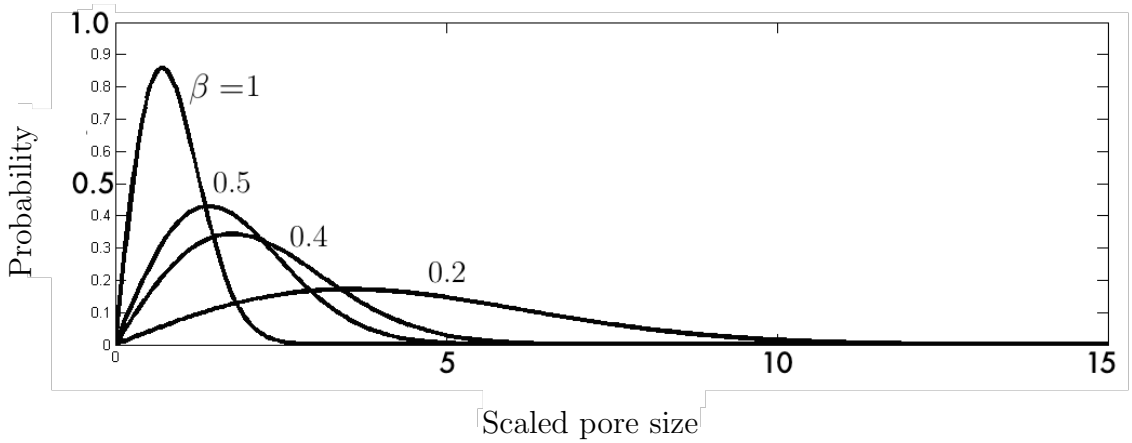

Figure 3.3: Effect of β on the shape of PDF curve. Decreasing particle size or packing density, the pore and throat sizes, as well as their variation increase and β decrease. Lower β values implies wider range of pore sizes which leads to higher heterogeneity

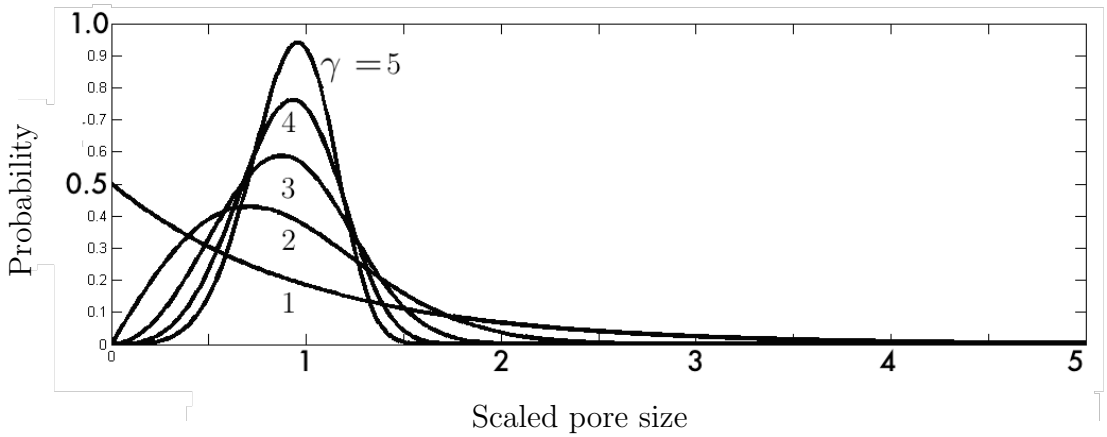

Figure 3.4: Parameter γ and its effect on PDF curve. γ represents heterogeneity, higher γ implies higher heterogeneity

3.2.2 Orientation Angle

As is shown in Fig 3.2, the pore element is defined to be oriented with θ respect to the flow direction (here x) which is within a range of $-\frac{\pi}{2} \leq \theta \leq \frac{\pi}{2}$ as shown in Figure 3.2. The probability of a given angle, θ, of the capillary tube axis relative to the mean flow direction within a range $d\theta$ is given by the proportion of area (or amount

of solid angle) on a unit sphere swept out by the pore axis, $\cos\theta d\theta$. Accordingly, the probability distribution of the angle is $h(\theta) = \cos\theta$ and for a range of preferred possible angles is illustrated in Fig 3.5.

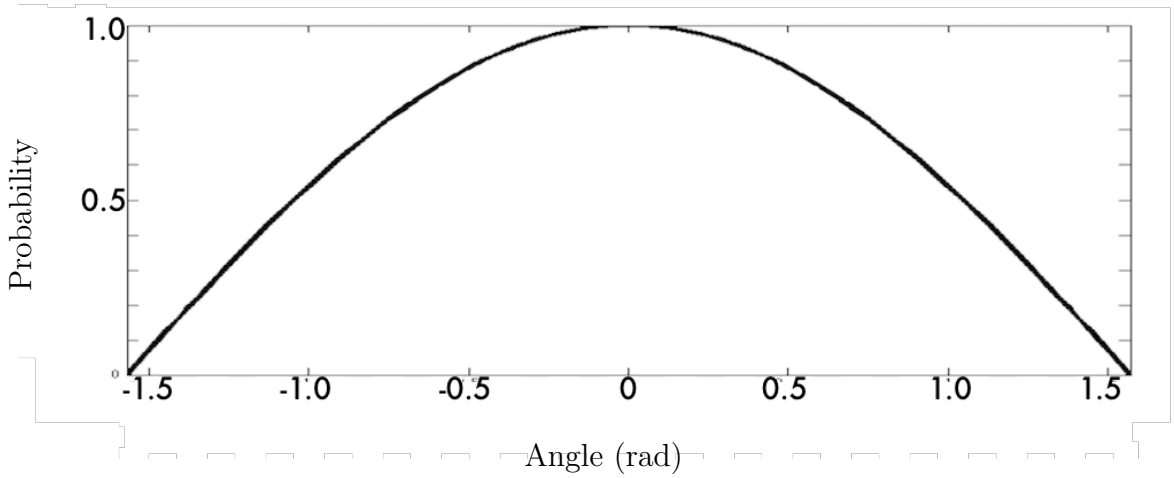

Figure 3.5: Probability of orientation angle respect to flow direction

3.2.3 Probability of Path Existence

Assuming steady, laminar flow in each tube, the flux of fluid through a given tube may be calculated using Poiseuille's law with the orientation and diameter of the tube [56]. The capillary tube is randomly oriented and the length and diameter vary independent of the orientation [37]. The probability that a given pore exists with size in the range l to $l + dl$, R to $R + dR$, and θ to $\theta + d\theta$ is given by the product of the independent probabilities as Equation 3.3 [52]:

$$d\psi = N\Big[f(R)dR \times g(l)dl \times \cos\theta d\theta\Big] \tag{3.3}$$

where N is the normalization factor to ensure that the distribution has unit variance and therefore also unit standard deviation. Thus, the normalization factor (N) is

found below. It should be mentioned that for $f(R)$ and $g(l)$ the integration is equal to unity (summation of probabilities equals 1). It should be mentioned that for $f(R)$ and $g(l)$ the integration is equal to unity.

$$\int_{\psi} d\psi = 1 \Rightarrow N \underbrace{\int_{R_{min}}^{R_{max}} f(R)dR}_{1} \underbrace{\int_{l_{min}}^{l_{max}} g(l)dl}_{1} \underbrace{\int_{-\pi/2}^{\pi/2} \cos\theta d\theta}_{2} = 1 \tag{3.4}$$

The normalization factor is obtained $N = \frac{1}{2}$, so the probability of the existence of a certain pore element is as equation 3.5:

$$d\psi = \frac{1}{2} f(R)dR g(l)dl \cos\theta d\theta \tag{3.5}$$

At each intersection, the probability of the path choice must be related to the probability of the existence of a pore element (Equation 3.5) and the fluid velocity (Equation 3.8). Accordingly, the certain path probability is as below:

$$d\Psi = \zeta q d\psi \quad \text{where} \quad q = \frac{\pi R^2}{4} v \tag{3.6}$$

where ζ is the normalization factor. Substituting Equations 3.5 and 3.8 into Equation 3.6 and integrating results in ζ.

$$\zeta = -\frac{512\mu L_n}{\pi^2 \Delta p \left\langle R^4 \right\rangle} \Rightarrow d\Psi = \frac{2}{\pi \left\langle R^4 \right\rangle} \, g(l)dl \; R^4 f(R)dR \; \cos^2\theta d\theta \tag{3.7}$$

3.3 Calculation of Average Velocities

The permeability of the described model is found by relating the average velocity in a pore element to the average velocity. We follow the same procedure as Kozeny-Carman to find the absolute permeability [18]. We assume that the inertia of the fluid

is negligible and the motion through the pores is dominated by viscosity. Consider that the bulk flow through the model is only in the x direction, and the Reynold's number of flow through capillaries is low ($Re \leq 1$), then according to the Hagen-Poiseuille Equation [50]:

$$v = -\frac{R^2}{32\mu}\frac{\Delta p}{L_n}\cos\theta \tag{3.8}$$

The components of the x and y directional velocity are:

$$v_x = v\cos\theta \qquad ; \qquad v_y = v\sin\theta \tag{3.9}$$

The average velocities in each direction for the ensemble of pores can be found by the integrating the velocity components in Equation 3.9 over the entire range of size and orientation as below:

$$\langle v_x\rangle = \int_\psi v\cos\theta d\psi \tag{3.10}$$

$$= -\tfrac{1}{2}\tfrac{1}{32\mu}\tfrac{\Delta p}{L_n}\int_{R_{min}}^{R_{max}} R^2 f(R)dR \int_{l_{min}}^{l_{max}} g(l)dl \int_{-\pi/2}^{\pi/2}\cos^3\theta d\theta \tag{3.11}$$

$$= \tfrac{1}{64\mu}\tfrac{\Delta p}{L_n} \times \langle R^2\rangle \times 1 \times \tfrac{4}{3} = -\tfrac{\langle R^2\rangle}{48\mu}\tfrac{\Delta p}{L_n} \tag{3.12}$$

$$\langle v_y\rangle = \int_\psi v\sin\theta d\psi \tag{3.13}$$

$$= -\tfrac{1}{2}\tfrac{1}{32\mu}\tfrac{\Delta p}{L_n}\int_{R_{min}}^{R_{max}} R^2 f(R)dR \int_{l_{min}}^{l_{max}} g(l)dl \int_{-\pi/2}^{\pi/2}\sin\theta\cos^2\theta d\theta \tag{3.14}$$

$$= \tfrac{1}{64\mu}\tfrac{\Delta p}{L_n} \times \langle R^2\rangle \times 1 \times 0 = 0 \tag{3.15}$$

where $\langle\rangle$ means average or expected value (See Appendix A.5). The expected value of the flow velocity for porous media represented by a bundle of capillaries is given by Equation 3.16:

$$\langle v_x\rangle = -\frac{\langle R^2\rangle}{48\mu}\frac{\Delta p}{L_n} \tag{3.16}$$

where $\langle R^2 \rangle$ refers to the second moment of the pore throat diameter.

3.4 Model of Fluid Transport

The macroscopic transport of a non-reactive solute in a porous medium can be described by three main transport processes: the advective motion with the mean velocity field of the flow, the molecular diffusion, and the hydrodynamic dispersion of the solute [28]. On the pore scale, dispersive flux is due to sub scale variations in velocity caused by the varying thickness of pores, the bending of streamlines around the grains, and the variation of the velocity profiles within the pores [76]. This study because of broader coverage of higher velocity displacements, assumes a higher Peclet number condition where advection (mechanical mixing) dominates.

3.5 Mass Conservation Model

The Advection-Diffusion Equation (mass conservation law) to describe solute dispersion in porous media in two dimensions is commonly written as[8]:

$$\frac{\partial C}{\partial t} = D_L \frac{\partial^2 C}{\partial x^2} + D_T \frac{\partial^2 C}{\partial y^2} - v\nabla C = \underbrace{D_L \frac{\partial^2 C}{\partial x^2} + D_T \frac{\partial^2 C}{\partial y^2}}_{\text{Advective term}} - v_x \frac{\partial C}{\partial x} - v_y \frac{\partial C}{\partial y} \tag{3.17}$$

where C is the solute concentration, t is time, v_x and v_y are the components of flow velocity, and D_L and D_T are the longitude and transverse dispersion coefficients. In order to use Random Walk Theory (RWT), we need to define the longitudinal and transverse dispersion components from statistical theory to obtain the statistical models. The main advantages of statistical models are lower processing time and higher customizability which leads to higher accuracy and better results of miscible

displacement simulation. For this purpose, the Mean Squared Displacement (MSD) for a random variable (X) is defined as Equation 3.18 with expansion:

$$\text{MSD} \quad = \langle (X - \langle X \rangle)^2 \rangle = \langle X^2 \rangle + \langle X \rangle^2 - 2\langle X \rangle \times \langle X \rangle \tag{3.18}$$

$$= \langle X^2 \rangle - \langle X \rangle^2 \tag{3.19}$$

Using the moment generating function, which is used to describe the moments of the PDF, it is possible to prove that MSD is related to the statistical definition of dispersion coefficient by Equation 3.20.

$$\text{Mean Squared Displacement} = \langle X^2 \rangle - \langle X \rangle^2 = 2DT \rightarrow D = \frac{\langle X^2 \rangle - \langle X \rangle^2}{2T} \tag{3.20}$$

Equation 3.20 shows that the time-average squared displacement is not zero unless the particle has no movement. Hence, the dispersion coefficient, D, exists for any velocity higher than zero. In order to define the longitudinal and transverse dispersion we need to find the displacements in the x and y directions. Based on equation 3.20, the longitudinal and transverse dispersion coefficients (using statistical concept of fluid flow) can be defined as equation 3.21:

$$D_L = \frac{\langle (X_n - \langle v \rangle T)^2 \rangle}{2T} \qquad D_T = \frac{\langle Y_n^2 \rangle}{2T} \tag{3.21}$$

where X_n and Y_n are displacements of the particle in x (parallel to flow direction) and y (perpendicular to flow direction) after n steps and $\langle V \rangle$ is the velocity of the most probable fluid path.

3.6 Categorization of Flow Regimes

A random particle is a marked fluid particle as it wanders through the porous medium selecting elemental pores for each step, according to the prescribed probability function. Each passage of a particle through an individual pore is a step in the random walk. As explained, in this study, we take a coordinate system with the x- axis in the direction of the average velocity, and denote the length of a step l, by θ the angle between the direction of motion along the step and that of the average velocity, t is the duration of the step, and $v = l/t$ is the velocity of the marked particle along the step. The properties derived here will be fulfilled after a particle has completed a very large number, n, of statistically independent steps. In order to find the average time step, an average of $\frac{l}{v}$ over the probability area ($d\Psi$) is required.

$$\langle t \rangle = \int_{\Psi} \left(\frac{l}{v} \right) d\Psi = \frac{4\langle R^2 \rangle}{3\pi \langle R^4 \rangle \langle v_x \rangle} \int_{R_{min}}^{R_{max}} \frac{R^4}{R^2} f(R) dR \int_{l_{min}}^{l_{max}} l g(l) dl \int_{-\pi/2}^{\pi/2} \cos\theta d\theta \quad (3.22)$$

$$= \frac{4\langle R^2 \rangle}{3\pi \langle R^4 \rangle \langle v_x \rangle} \times \langle R^2 \rangle \times \langle l \rangle \times 2 = \frac{8\langle l \rangle \langle R^2 \rangle^2}{3\pi \langle R^4 \rangle \langle v_x \rangle} \quad (3.23)$$

Equation 3.22 shows the average duration for each step over a large number of n steps. As is shown in Equation 3.22, if the velocity is very low (low Peclet number $Pe \leq 5$), the average pore throat length is very large or the variance of the pore throat diameter is significantly large which means a higher heterogeneity; the average time $\langle t \rangle$ is higher; and molecular diffusion has a large effect. This is physically permissible. However, even if the molecular diffusivity is very small for a high velocity (or $Pe \geq 300$), there will still be solute that reside sufficiently long in a pore that molecular diffusion may be significant. It is not clear whether it is consequential to regard them as moving like idealized fluid particles. The effect of molecular diffusion can be described in two possible ways. First, the material quantity diffuses sideways across the pore so that an

element of the material quantity does not stay on a streamline constant but spreads out over neighbouring streamlines. It may be expected that this effect is negligible if $\langle t \rangle \ll t_{critical}$, where $t_{critical}$ is the time for appreciable molecular diffusion over a distance comparable with that in which the velocity differs by a factor of order unity. Molecular diffusion can also be responsible for solute transport along a pore when the velocity is significantly low and mechanical dispersion is negligible. To estimate the required time for molecular diffusion to be effective by either way, (as introduced definition in Equation 3.20), could be used, as below:

$$\text{Mean Squared Displacement} = 2D_m t_{critical} \quad . \tag{3.24}$$

Here, we assume that if MSD is comparable with the average pore throat radius $\frac{\langle R \rangle}{2}$ (named $t_{critical}$) then the first effect of molecular diffusion is appreciable and if the MSD is comparable with the average pore throat length $\langle l \rangle$ then a component has ample time to diffuse through pores. Therefore, molecular diffusion is the dominant regime and the effect of mechanical dispersion (advection) is negligible. The prior assertion may be combined in an approximation to give the following rule for specifying the duration of a step by a particle as below:

$$\begin{cases} \text{if} \quad \langle t \rangle = \frac{8\langle l \rangle \langle R^2 \rangle^2}{3\pi \langle R^4 \rangle \langle v_x \rangle} \ll t_{critical} = \frac{\langle R \rangle^2}{8D_m} & \text{molecular diffusion is negligible} \\ \text{if} \quad \langle t \rangle \approx t_{critical} & \text{dispersion and diffusion are important} \\ \text{if} \quad t_{critical} \leq \langle t \rangle \leq t^*_{critical} = \frac{\langle l \rangle^2}{2D_m} & \text{mechanical dispersion is negligible} \end{cases} \tag{3.25}$$

Equation 3.25 shows three different regimes including, advective, coupled advective and diffusive, and diffusion dominated regimes. The challenge is when both mechanical dispersion and molecular diffusion are important in lower Peclet numbers

$(0.1 \leq \log Pe \leq 1)$. Figure 3.6 illustrates the three regimes. Region I $(\log Pe \leq$

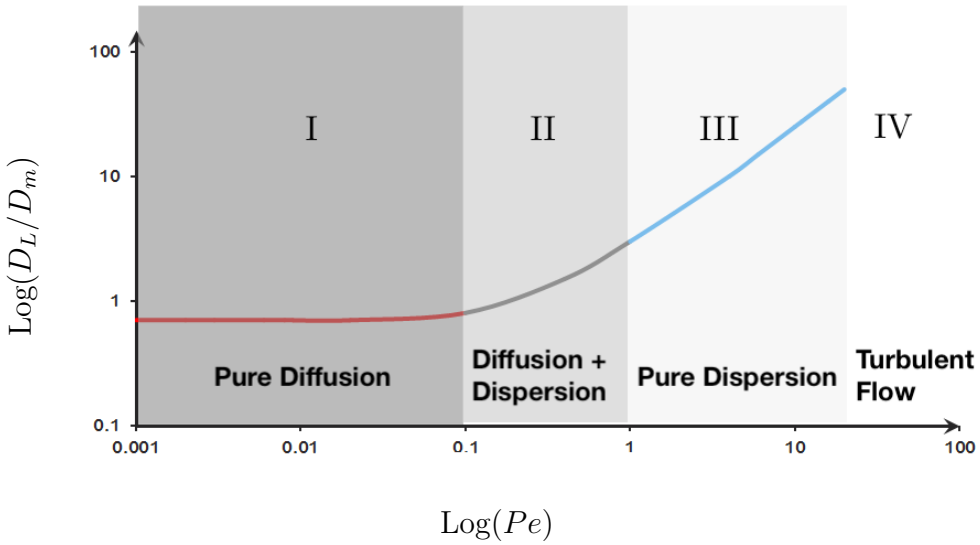

Figure 3.6: Flow regimes for increasing flow velocity [66]

0.1) represents the range of Peclet numbers where diffusion is dominant, region II $(0.1 \leq \log Pe \leq 1)$ illustrates the dispersion and diffusion are important, region III $(1 \leq \log Pe \leq 12)$ represents the advection dominant regime, and region IV $(\log Pe \geq 12)$ shows the condition under which Darcy's law is no longer valid[66].

3.7 Region III

In general, if $\langle t \rangle$ is assumed to be small compared to the time required for molecular diffusion to be appreciable, advection or mechanical mixing (dispersion) is the dominant mass transfer regime. In this section, the limit of very large Pe number is considered, where the Central limit theory (CLT) is valid. In this limit, the effect of molecular diffusion is insignificant compared to dispersion so both D_L and D_T are assumed to be dependent only on velocity.

3.7.1 Probabilistic Properties after n Steps

To find the expressions in Equation 3.21, we need to first calculate the variances of the displacements in the $x-$ and $y-$directions. For this purpose, we need to find the displacement of a marked particle after n steps in both directions. Fig 3.7 shows the proposed procedure to find the dispersion coefficients.

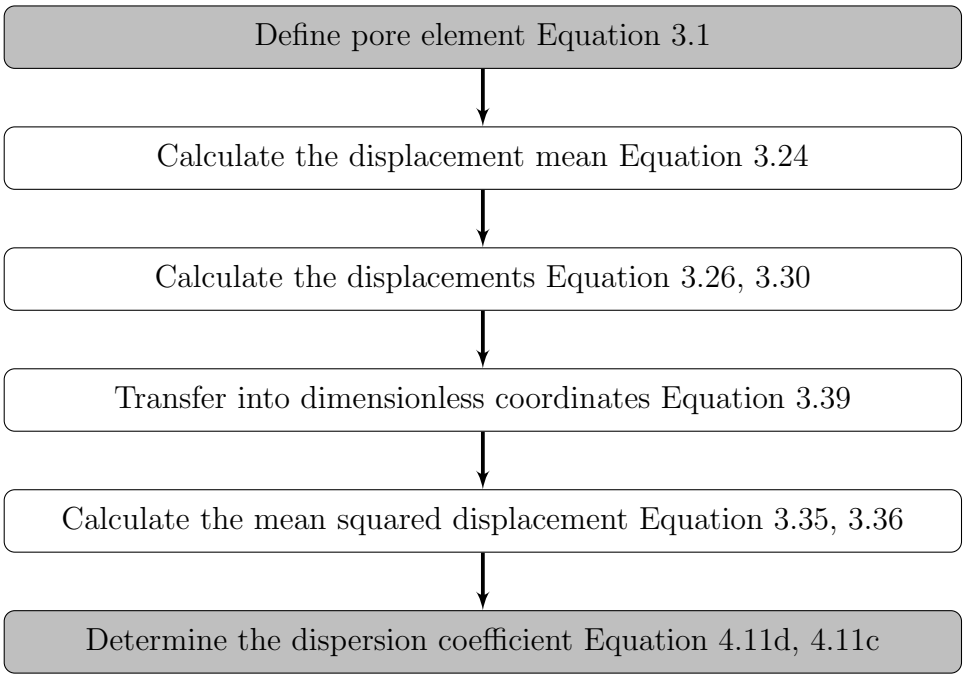

Figure 3.7: Procedure for calculation of dispersion coefficient

Following this procedure, we need to find the mean displacement in each direction. Displacement in the $x-$direction is $\cos\theta$ component of displacement and $\sin\theta$ in the $y-$direction. Substituting the probability of the path choice from Equation 3.7 yields:

$$\langle X_n \rangle = n \int_\Psi l \cos\theta d\Psi = \frac{2n}{\pi\langle R^4\rangle} \int_\Psi l g(l) dl R^4 f(R) dR \cos^3\theta d\theta \tag{3.26}$$

$$= \frac{2n}{\pi\langle R^4\rangle} \underbrace{\int_{l_{min}}^{l_{max}} l g(l) dl}_{\langle l\rangle} \underbrace{\int_{R_{min}}^{R_{max}} R^4 f(R) dR}_{\langle R^4\rangle} \underbrace{\int_{-\pi/2}^{\pi/2} \cos^3\theta d\theta}_{\frac{4}{3}} \tag{3.27}$$

$$= \frac{8n\langle l\rangle}{3\pi} \tag{3.28}$$

For this level, the velocity of the most probable transport path can be found by finding the ratio of average x and average t as below:

$$\langle v\rangle = \frac{\langle x\rangle}{\langle t\rangle} = \frac{\frac{8n\langle l\rangle}{3\pi}}{\frac{8\langle l\rangle\langle R^2\rangle^2}{3\pi\langle R^4\rangle\langle v_x\rangle}} = \frac{\langle R^4\rangle}{\langle R^2\rangle^2}\langle v_x\rangle \tag{3.29}$$

The same procedure is followed in the $y-$direction below:

$$\langle Y_n\rangle \quad = n\int_\Psi l\sin\theta d\Psi = \tfrac{2n}{\pi\langle R^4\rangle}\int_\Psi lg(l)dlR^4f(R)dR\sin\theta\cos^2\theta d\theta \tag{3.30}$$

$$= \tfrac{2n}{\pi\langle R^4\rangle}\underbrace{\int_{l_{min}}^{l_{max}} lg(l)dl}_{\langle l\rangle}\underbrace{\int_{R_{min}}^{R_{max}} R^4f(R)dR}_{\langle R^4\rangle}\underbrace{\int_{-\pi/2}^{\pi/2}\sin\theta\cos^2\theta d\theta}_{0} \tag{3.31}$$

$$= 0 \tag{3.32}$$

The average time step is calculated in Equation 3.22. As a second step we need to find the variances of the total displacements in x and y and also the variance of the time steps. Using the definition of variance (See Appendix A.7) we get:

$$\underbrace{\overbrace{\langle(\underbrace{X_n}_{\text{veriable}} - \underbrace{\langle X_n\rangle}_{\text{mean}})^2\rangle}^{\text{Squared}}}_{\text{mean}} \quad = n\langle(x_n - \langle x_n\rangle)^2\rangle = \underbrace{n\langle x^2\rangle - n\langle x\rangle^2}_{\text{see Equation 3.18}} \tag{3.33}$$

$$= n\int_\Psi l^2\cos^2\theta d\Psi - n(\tfrac{8\langle l\rangle}{3\pi})^2 = n\langle l\rangle^2\sigma_x^2 \tag{3.34}$$

Substituting $d\Psi$ from Equation 3.7 results in a variance of displacement in the $x-$direction σ_x (See Appendix A.7 for full proof) as below:

$$\sigma_x^2 = \frac{3\langle l^2\rangle}{4\langle l\rangle^2} - \frac{64}{9\pi^2} \tag{3.35}$$

Following the same approach results in σ_y (See Appendix A.7 for full proof):

$$\sigma_y^2 = \frac{\langle l^2 \rangle}{4\langle l \rangle^2} \tag{3.36}$$

And for the time variance we assume that, the CLT is valid for the time distribution as well, which is generally correct for random processes occurring in nature [19]. This assumption means that $\frac{\langle (X_n - \langle V \rangle T)^2 \rangle}{2}$ tends to be independent from the value of T. Considering this assumption, σ_t could be defined as (See Appendix A.7 for fully detailed proof):

$$n\frac{\langle l \rangle^2}{\langle v_x \rangle^2}\sigma_t^2 = \langle (T_n - \langle T_n \rangle)^2 \rangle \Rightarrow \sigma_t = \frac{8\langle R^2 \rangle^2 \langle l^2 \rangle}{9\langle R^4 \rangle \langle l \rangle^2} - \frac{64\langle R^2 \rangle^4}{9\pi^2 \langle R^4 \rangle^2} \quad . \tag{3.37}$$

Considering Equation 3.21 we need to find the covariance of x and t as well, which is illustrated below (See Appendix A.8 for fully detailed proof):

$$n\frac{\langle l \rangle^2}{\langle v_x \rangle}\sigma_{xt}^2 = \langle (T_n - \langle T_n \rangle)(X_n - \langle X_n \rangle) \rangle \Rightarrow \sigma_{xt} = \frac{2\langle R^2 \rangle^2 \langle l^2 \rangle}{3\langle R^4 \rangle \langle l \rangle^2} - \frac{64\langle R^2 \rangle^2}{9\pi^2 \langle R^4 \rangle} \tag{3.38}$$

As a next step, using Equations 3.35, 3.36 and 3.37, we define dimensionless variables as below:

$$\chi = \frac{X_n - \langle X_n \rangle}{\langle l \rangle \sqrt{n}} \qquad \eta = \frac{Y_n - \langle Y_n \rangle}{\langle l \rangle \sqrt{n}} \qquad \tau = \frac{(T_n - \langle T_n \rangle)\langle v_x \rangle}{\langle l \rangle \sqrt{n}} \tag{3.39}$$

χ, η and τ are defined to have a mean equal to zero and variance equal to σ_x^2 , σ_y^2 and σ_t^2, respectively (See Appendix A.9). It is assumed that χ, η and τ follow from the CLT which means that the probability distribution of χ, ξ and τ are converging to be normal and independent as $n \to \infty$. For τ, the rate of convergence depends on σ_t^2 and thus the number of steps. In this study, we assume n is a large number to satisfy

this condition.

3.7.2 Probabilistic Properties at a Given Time

So far, the mean of displacements in the $x-$ and $y-$directions and the mean of time steps after n steps that are significantly large and fixed has been calculated. In order to calculate the dispersion, we need to analyze the probabilistic properties at a given time T_n, which is significantly larger than $\frac{l}{v}$. This assumption is in agreement with assuming a large value for n. Set of defined dimensionless variables in Equation 3.39 are used to find the probability distribution of n in a given time T_n and n appears as Equation 3.47.

$$\tau = \frac{(T_n - \langle T_n \rangle)\langle v_x \rangle}{\langle l \rangle \sqrt{n}} \xrightarrow{\text{From Equation 3.22}} \tau = \frac{T_n \langle v_x \rangle}{\langle l \rangle \sqrt{n}} - \left(\frac{8n\langle l \rangle \left\langle R^2 \right\rangle^2}{3\pi \langle R^4 \rangle \langle v_x \rangle} \right) \left(\frac{\langle v_x \rangle}{\langle l \rangle \sqrt{n}} \right) \tag{3.40}$$

$$= \frac{T_n \langle v_x \rangle}{\langle l \rangle \sqrt{n}} - \frac{8\sqrt{n}\left\langle R^2 \right\rangle^2}{3\pi \langle R^4 \rangle} \xrightarrow{\times \sqrt{n}} \tau \sqrt{n} = \frac{T_n \langle v_x \rangle}{\langle l \rangle} - \frac{8n\left\langle R^2 \right\rangle^2}{3\pi \langle R^4 \rangle} \xrightarrow{\text{subtract } \tau\sqrt{n}} \tag{3.41}$$

$$\frac{8\left\langle R^2 \right\rangle^2}{3\pi \langle R^4 \rangle} n + \tau \sqrt{n} - \frac{T_n \langle v_x \rangle}{\langle l \rangle} = 0 \tag{3.42}$$

The Equation 3.40 can be solved by squared equations rule for n as below:

$$\left(\frac{16\langle R^2 \rangle^2}{3\pi \langle R^4 \rangle} \sqrt{n} + \tau \right)^2 = \tau^2 + \frac{32\langle R^2 \rangle^2 T_n \langle v_x \rangle}{3\pi \langle R^4 \rangle \langle l \rangle} \Rightarrow \frac{16\langle R^2 \rangle^2}{3\pi \langle R^4 \rangle} \sqrt{n} = -\tau + \tag{3.43}$$

$$\sqrt{\tau^2 + \frac{32\langle R^2 \rangle^2 T_n \langle v_x \rangle}{3\pi \langle R^4 \rangle \langle l \rangle}} \, , \sqrt{n} = -\frac{3\pi \langle R^4 \rangle}{16\langle R^2 \rangle^2} \tau + \frac{3\pi \langle R^4 \rangle}{16\langle R^2 \rangle^2} \sqrt{\tau^2 + \frac{32\langle R^2 \rangle^2 T_n \langle v_x \rangle}{3\pi \langle R^4 \rangle \langle l \rangle}} \tag{3.44}$$

$$n = \frac{9\pi^2 \langle R^4 \rangle^2}{256\langle R^2 \rangle^4} \tau^2 + \frac{9\pi^2 \langle R^4 \rangle^2}{256\langle R^2 \rangle^4} \left(\tau^2 + \frac{32\langle R^2 \rangle^2 T_n \langle v_x \rangle}{3\pi \langle R^4 \rangle \langle l \rangle} \right) - \frac{9\pi^2 \langle R^4 \rangle^2}{128\langle R^2 \rangle^4} \tau \tag{3.45}$$

$$\sqrt{\tau^2 + \frac{32\langle R^2 \rangle^2 T_n \langle v_x \rangle}{3\pi \langle R^4 \rangle \langle l \rangle}} \tag{3.46}$$

The positive square root is taken to make n positive from 0 to ∞. Hence, final statement for n at a given time T_n is:

$$n = \frac{3\pi\langle R^4\rangle\langle v_x\rangle T_n}{8\langle R^2\rangle^2\langle l\rangle} + \frac{9\pi^2\langle R^4\rangle^2}{128\langle R^2\rangle^4}\tau^2 - \frac{9\pi^2\langle R^4\rangle^2}{256\langle R^2\rangle^4}\tau\sqrt{\tau^2 + \frac{32\langle R^2\rangle^2 T_n\langle v_x\rangle}{3\pi\langle R^4\rangle\langle l\rangle}} \tag{3.47}$$

It is assumed that the distribution of the dimensionless variable τ follows the CLT and it tends to be asymptotically normal. This means (as is shown in Equation 3.47) that the mean value of n appears when $\tau \to 0$ and therefore T_n and $T_{\langle n\rangle}$ are identical and values of n and $\langle n\rangle$ are compareable. Hence $O(\tau) = \tau$ and τ^2 is negligible[1]. Thus, the mean of n at a given time T_n becomes:

$$\langle n\rangle = \frac{3\pi\langle R^4\rangle\langle v_x\rangle T_n}{8\langle R^2\rangle^2\langle l\rangle} - \frac{9\pi^2\langle R^4\rangle^2}{256\langle R^2\rangle^4}\tau\sqrt{\frac{32\langle R^2\rangle^2 T_n\langle v_x\rangle}{3\pi\langle R^4\rangle\langle l\rangle}} \tag{3.48}$$

The other probabilistic properties that should be found after a given time are the mean of variance of displacements in each direction.

3.7.3 Transverse Dispersion Calculation

Starting in the $y-$direction, which is perpendicular to the dominant flow, the statistical transverse displacement after a given time (T_n) can be calculated using Equations 3.30, 3.36 and 3.39, as:

$$\eta = \frac{Y_n - \langle Y_n\rangle}{\langle l\rangle\sqrt{n}} \xrightarrow{\langle Y_n\rangle = 0} Y_n = \eta\,\langle l\rangle\,\sqrt{n} \Rightarrow Y_n^2 = \eta^2\,\langle l\rangle^2\,n \Rightarrow \langle Y_n^2\rangle = \langle\eta^2\rangle\,\langle l\rangle^2\,\langle n\rangle \tag{3.49}$$

where η is defined as a dimensionless variable with a mean of zero and variance of σ_y^2 so $\langle\eta^2\rangle = \sigma_y^2$ and σ_y^2 is $\sigma_y^2 = \frac{\langle l^2\rangle}{4\langle l\rangle^2}$ from Equation 3.36. The average number of steps is

[1] $O(X)$ describes the limiting behavior of a function when the argument tends towards a particular value. Here τ tends to 0

found in Equation 3.48. Substitution of the values yields:

$$\langle Y_n^2 \rangle = \frac{\langle l^2 \rangle}{4\langle l \rangle^2} \langle l \rangle^2 \left(\frac{3\pi \langle R^4 \rangle \langle v_x \rangle T_n}{8\langle R^2 \rangle^2 \langle l \rangle} - \frac{9\pi^2 \langle R^4 \rangle^2}{256\langle R^2 \rangle^4} \tau \sqrt{\frac{32\langle R^2 \rangle^2 T_n \langle v_x \rangle}{3\pi \langle R^4 \rangle \langle l \rangle}} \right) \tag{3.50}$$

$$= \frac{3\pi \langle R^4 \rangle \langle l \rangle^2 \langle v_x \rangle T_n}{32\langle R^2 \rangle^2 \langle l \rangle} - \underbrace{\frac{9\pi^2 \langle R^4 \rangle^2 \langle l \rangle^2}{128\langle R^2 \rangle^4} \langle \tau \rangle \sqrt{\frac{2\langle R^2 \rangle^2 T_n \langle v_x \rangle}{3\pi \langle R^4 \rangle \langle l \rangle}}}_{\text{negligible as } \langle \tau \rangle \to 0} \tag{3.51}$$

We know that at a given time n is a large number and therefore τ approaches zero and we can therefore neglect the effect of the second term. Referring to Equation 3.21, and rearranging Equation 3.50 results in:

$$D_T = \frac{\langle Y_n^2 \rangle}{2T} = \frac{3\pi}{64} \frac{\langle l^2 \rangle}{\langle l \rangle} \frac{\langle R^4 \rangle}{\langle R^2 \rangle^2} \langle v_x \rangle \tag{3.52}$$

This statement for transverse dispersion is valid under the considered assumptions. The main assumption is a higher Peclet number, which infers higher velocity and consequently a smaller time step. This causes mechanical dispersion to be dominant and molecular diffusion to be negligible.

3.7.4 Longitudinal Dispersion Calculation

The mean variance of longitudinal displacement occurring after T_n can be calculated from definition of χ as below:

$$\chi = \frac{X_n - \langle X_n \rangle}{\langle l \rangle \sqrt{n}} \xrightarrow{\langle X_n \rangle = \frac{8n\langle l \rangle}{3\pi}} X_n - \frac{8n\langle l \rangle}{3\pi} = \chi \langle l \rangle \sqrt{n} \Rightarrow X_n = \chi \langle l \rangle \sqrt{n} + \frac{8n\langle l \rangle}{3\pi}$$

$$X_n = \underbrace{\chi \langle l \rangle \sqrt{\frac{3\pi\langle R^4 \rangle \langle v_x \rangle T_n}{8\langle R^2 \rangle^2 \langle l \rangle} - \frac{9\pi^2 \langle R^4 \rangle^2}{128\langle R^2 \rangle^4} \tau \sqrt{\frac{32\langle R^2 \rangle^2 T_n \langle v_x \rangle}{3\pi \langle R^4 \rangle \langle l \rangle}}}}_{\text{Term 1}} +$$

$$\underbrace{\frac{8\langle l \rangle}{3\pi} \Big(\frac{3\pi\langle R^4 \rangle \langle v_x \rangle T_n}{8\langle R^2 \rangle^2 \langle l \rangle}}_{\text{Term 2}} \underbrace{- \frac{9\pi^2 \langle R^4 \rangle^2}{128\langle R^2 \rangle^4} \tau \sqrt{\frac{32\langle R^2 \rangle^2 T_n \langle v_x \rangle}{3\pi \langle R^4 \rangle \langle l \rangle}} \Big)}_{\text{Term 3}} =$$

$$\frac{\langle R^4 \rangle}{\langle R^2 \rangle^2} \langle v_x \rangle T_n - \frac{3\pi \langle R^4 \rangle^2 \langle l \rangle}{16\langle R^2 \rangle^4} \tau \sqrt{\frac{32\langle R^2 \rangle^2 T_n \langle v_x \rangle}{3\pi \langle R^4 \rangle \langle l \rangle}} +$$

$$\chi \langle l \rangle \sqrt{\frac{3\pi\langle R^4 \rangle \langle v_x \rangle T_n}{8\langle R^2 \rangle^2 \langle l \rangle}} \Big(1 - \underbrace{\frac{3\pi \langle R^4 \rangle \langle l \rangle}{32\langle R^2 \rangle^2 \langle v_x \rangle T_n} \tau \sqrt{\frac{32\langle R^2 \rangle^2 T_n \langle v_x \rangle}{3\pi \langle R^4 \rangle \langle l \rangle}}}_{\text{Negligible when multiplied by } \chi\langle l \rangle} \Big) \xrightarrow[\text{From Equation 3.29}]{\frac{\langle R^4 \rangle}{\langle R^2 \rangle^2} \langle v_x \rangle T_n = \langle v \rangle T_n}$$

$$X_n = \langle v \rangle T_n - \tau \sqrt{\frac{3\pi \langle R^4 \rangle \langle \langle l \rangle v_x \rangle T_n}{8\langle R^2 \rangle^2}} + \chi \sqrt{\frac{3\pi \langle R^4 \rangle \langle \langle l \rangle v_x \rangle T_n}{8\langle R^2 \rangle^2}} \tag{3.53}$$

Since T_n is large and τ is small, the Taylor expansion rule[2] is used to linearly approximate it. In Term 2 of Equation 3.53 the product of $\chi\tau$ is negligible when τ and χ both approach zero, while T_n is significantly larger than $\frac{l}{\langle v \rangle}$ and X_n is identical to $X_{\langle n \rangle}$. All of the simplifications produce calculation error in the dispersion coefficient that is estimated at the end, however results show that the error is not not significant. Rearrangement of Equation 3.53 and subtracting $\langle v \rangle T_n$ from both the sides produces a longitudinal displacement term on the left side. Squaring both sides and taking the

[2]Based on Taylor expansion $\sqrt{1-x} \to 1 - \frac{x}{2}$ when $x \to 0$

average yields:

$$X_n - \langle v\rangle T_n = \sqrt{\frac{3\pi\langle R^4\rangle\langle\langle l\rangle v_x\rangle T_n}{8\langle R^2\rangle^2}}(\chi-\tau) \Rightarrow (X_n-\langle v\rangle T_n)^2 = \frac{3\pi\langle R^4\rangle\langle l\rangle\langle v_x\rangle T_n}{8\langle R^2\rangle^2}$$

$$(\chi^2+\tau^2-2\chi\tau) \Rightarrow \langle (X_n-\langle v\rangle T_n)^2\rangle = \langle \frac{3\pi\langle R^4\rangle\langle l\rangle\langle v_x\rangle T_n}{8\langle R^2\rangle^2}\rangle \underbrace{\big(\langle\chi^2\rangle+\langle\tau^2\rangle-2\langle\chi\tau\rangle\big)}_{\text{From Equation 3.39}}$$

$$\Rightarrow \underbrace{\frac{\langle (X_n-\langle v\rangle T_n)^2\rangle}{2T_n}}_{D_L} = \frac{3\pi\langle R^4\rangle\langle l\rangle\langle v_x\rangle}{16\langle R^2\rangle^2}\big(\sigma_x^2+\sigma_t^2-2\sigma_{xy}\big) \xrightarrow[\sigma_x^2,\ \sigma_t^2 \text{ from Equation 3.35, 3.37}]{\sigma_{xt} \text{ from Equation 3.38}} =$$

$$\frac{3\pi\langle R^4\rangle\langle l\rangle\langle v_x\rangle}{16\langle R^2\rangle^2}\Big(\underbrace{\frac{3\langle l^2\rangle}{4\langle l\rangle^2}-\frac{64}{9\pi^2}}_{\sigma_x^2}+\underbrace{\frac{8\langle R^2\rangle^2\langle l^2\rangle}{9\langle R^4\rangle\langle l\rangle^2}-\frac{64\langle R^2\rangle^4}{9\pi^2\langle R^4\rangle^2}}_{\sigma t}-\underbrace{\frac{4\langle R^2\rangle^2\langle l^2\rangle}{3\langle R^4\rangle\langle l\rangle^2}+\frac{128\langle R^2\rangle^2}{9\pi^2\langle R^4\rangle}}_{\sigma_{xt}}\Big)$$

$$D_L = \frac{9\pi}{64}\frac{\langle l^2\rangle}{\langle l\rangle}\frac{\langle R^2\rangle^2}{\langle R^4\rangle}\langle v_x\rangle + \frac{\pi\langle l^2\rangle}{12\langle l\rangle}\langle v_x\rangle - \underbrace{\Big(\frac{4\langle R^4\rangle}{3\pi\langle R^4\rangle}+\frac{4\langle R^2\rangle^2}{3\pi\langle R^2\rangle^2}-\frac{8}{3\pi}\Big)\langle l\rangle\langle v_x\rangle}_{\text{Negligible in comparison with other the two terms}} \tag{3.54}$$

$$D_L = \frac{9\pi}{64}\frac{\langle l^2\rangle}{\langle l\rangle}\frac{\langle R^4\rangle}{\langle R^2\rangle^2}\langle v_x\rangle + \frac{\pi}{12}\frac{\langle l^2\rangle}{\langle l\rangle}\langle v_x\rangle \tag{3.55}$$

The assumptions for validity of this statement for longitudinal dispersion are that *i*) the effect of mechanical dispersion is an order of magnitude larger than molecular diffusion; *ii*) the flooding time is sufficiently long; and *iii*) the total length of the system in significantly larger than the pore throat length. As is shown in Equation 4.11d and 4.11c, the transverse and longitudinal dispersion coefficients are dependant on three main parameters. First, the ratio of $\frac{\langle l^2\rangle}{\langle l\rangle}$, which is the normalized variance probability density function of the pore throat length distribution and is the degree of heterogeneity in statistical analysis of porous media. This ratio is not dimensionless and the units do not cancel, therefore the ratio has a unit of length. Hence, the dispersion coefficient obtained from the presented analysis is scale dependent, which is physically acceptable. Secondly, dispersion coefficients are dependant on the ratio

of $\frac{\langle R^4 \rangle}{\langle R^2 \rangle^2}$, which is the normalized kurtosis (fourth moment) of the probability density function of pore throat diameter distribution. Kurtosis represents the shape of the pore throat diameter distribution and the height and width of the distribution function (Appendix A.5). In simple terms, this ratio shows that for two porous media, if the mean and variance of the two pore throat diameter distributions are identical, the transverse and longitudinal dispersion can still be different, due to the complexity of pore structure. Finally, injection velocity affects dispersion which appeared in all proposed models to date, including both mathematical outcomes and experimental correlations [46]. Equation 4.11d and 4.11c indicate that increasing injection velocity results in increasing dispersion in both directions[3].

3.8 Analytical Solution

The theory of hydrodynamic dispersion of miscible fluid has been extensively studied during the past decades [26], and some analytical [8] and numerical models [76] have been developed for estimating the dispersion coefficients. In this section, an analytical solution is developed as a part of the image processing tool to estimate the experimental longitudinal and transverse dispersion coefficients. Analytical solutions are very useful in determining the physical feasibility of boundary conditions, evaluating the accuracy of numerical solution methodologies, as well as measuring the solute transport parameters under laboratory and field conditions. Some analytical solutions for one, two, and three-dimensional ADEs have been developed for predicting the transport properties. For example, van Genuchten and Alves [91] formulated several analytical solutions for the one dimensional, ADE subject to various initial and boundary conditions. Most two-dimensional available analytical solutions are based

[3]All analysis are valid under considered assumption and when mechanical dispersion is an order of magnitude larger than molecular diffusion

on point solute sources in an infinite medium [47]. Equation 1.2 presents the assumed mathematical model for miscible displacement in 2D porous media. The main objective of this section is a derivation of the two-dimensional Advection-Diffusion Equation (ADE) solution for a model that is finite in width and has a finite length. The obtained solution is used in finding the longitudinal and transverse dispersion coefficients in 2D micromodel miscible displacement experiment.

3.8.1 Methodology

The following section details a generalized two-dimensional analytical solution that is developed for hydrodynamic dispersion in a unidirectional bounded porous media flow field. In the mathematical analysis, the Laplace transform, and Fourier analysis techniques are used simultaneously, and a general equation, in infinite series form has been obtained. The Advection Diffusion Equation (ADE) for two dimensional porous media is as Equation 3.56:

$$\frac{\partial C}{\partial t} = D_L \frac{\partial^2 C}{\partial x^2} + D_T \frac{\partial^2 C}{\partial y^2} - v_x \frac{\partial C}{\partial x} - v_y \frac{\partial C}{\partial y} \tag{3.56}$$

where C is the concentration of the solute (mass of solute per unit volume of the fluid) $[ML^{-3}]$, D_L is the longitudinal dispersion coefficient $[L^2T^{-1}]$, D_T is the transverse dispersion coefficient $[L^2T^{-1}]$, v_x is the average pore velocity in the longitudinal direction $[LT^{-1}]$, v_y is the average pore velocity in the transverse direction $[LT^{-1}]$.

3.8.2 Assumptions

Equation 3.56 is subject to the following assumptions; constant average velocity in both directions, constant porosity, constant longitudinal and transverse dispersion coefficient, negligible off-diagonal dispersion coefficient since flow is assumed to be

dominant in the longitudinal direction, and that the fluid is of constant density and viscosity and incompressible.

To solve the ADE, a complete set of boundary and initial conditions must be specified. Initial conditions are used to define the solute concentration at the time the solute is introduced. For the analytical solutions presented in this work, the initial conditions are specified that all initial concentrations are zero. If the solute is conservative, a constant initial background solute concentration can be added to the calculated concentrations. Also, three types of boundary conditions are associated with the solute-transport equation. The first-type or **Dirichlet** boundary condition specifies the value of the concentration along a section of the flow-system boundary. The second-type or **Neumann** boundary condition specifies the gradient in solute concentration across a section of the boundary. The third-type or **Cauchy** boundary condition must be applied where the flux of solute over the boundary is dependent on the difference in a specified concentration on one side of the boundary and the solute concentration on the other side of the boundary. These three models of boundary conditions are applied to describe conditions at the entrance and exit of two- and three-dimensional systems. The third-type boundary condition best describes solute concentrations at the injection end in a uniform flow system [62], where a well-mixed solute penetrates the system by advection across the boundary and is transported from the boundary by advection and diffusion. The boundary conditions can be presented as:

$$v_x C - D_L \frac{\partial C}{\partial x} = v_x C_0 \qquad at \qquad x = 0 \tag{3.57}$$

where C_0, is the known measured concentration in the injected fluid. The third-type boundary condition allows for solute concentration at the injection boundary to be lower than C_0, initially and then to increase as more solute enters the system. Over

time, the concentration gradient across the boundary, $\frac{\partial C}{\partial x}$, decreases the concentration at the injection boundary approaches C_0. Alternatively, a first-type boundary condition can be specified at the injection end, such that:

$$C = C_0 \qquad at \qquad x = 0 \tag{3.58}$$

Application of this simpler form of boundary condition presumes that the concentration gradient across the boundary equals zero as soon as flow begins. However, this may cause the mass of solute in the system at early times to be overestimated. Equation 3.57 indicates that the difference between concentrations predicted for a system having a first- type source boundary condition and a system having a third-type boundary condition should decrease as the quantity $\frac{D_m}{v_x}$ decreases. When the system has finite dimensions, and solute concentrations near the production boundary are of interest, selection of an appropriate boundary condition becomes more difficult. In general, if the system discharges to a large, well-mixed reservoir and the additional solute will not significantly alter reservoir concentrations, then a third-type or first-type boundary condition can be used. If the porous medium is small or not well mixed, concentrations would equal solute concentration at the production end of the system, and therefore no concentration gradient would exist across the boundary. A second-type boundary condition can define this condition as below:

$$\frac{\partial C}{\partial x} = 0 \qquad at \qquad x = L \tag{3.59}$$

where L shows the length. Van Genuchten and Alves [91] analyzed the difference between predicted concentrations obtained using analytical solutions for a semi-infinite system and a finite system having a second-type boundary condition regarding two dimensionless numbers. First, the Peclet number (Pe) and second the number of

displaced pore volumes (PV), which are defined by:

$$Pe = \frac{Lv_x}{D_m} \qquad , \qquad PV = \frac{v_x t}{L} \tag{3.60}$$

They found that the predicted concentration at points near the production boundary begins to differ significantly for greater than 0.25 pore volume (PV) and that the differences increase as PV approaches 1 (corresponding to movement of the solute front closer to the production boundary). In two- and three-dimensional systems, impermeable or no-flow boundaries may be present at the base, top, or sides of the aquifer. Because there is no advective flux across the boundary, and molecular diffusion across the boundary is assumed to be negligible, the general third-type boundary condition simplifies to a second-type boundary condition, expressed below as:

$$\frac{\partial C}{\partial y} = 0 \qquad at \qquad y = 0 \text{ and } y = W \tag{3.61}$$

where W shows the width of the system. Following our discussion above, the boundary and initial conditions for this case is assumed as below:

$$\begin{cases} C = 0 & at \quad y = 0, y = W \\ C = 0 & at \quad x = L \\ C(0, y, t) = C_0 & at \quad Y_1 < y < Y_2 \\ C(x, y, 0) = 0 & at \quad \textit{Initial condition} \end{cases} \tag{3.62}$$

3.8.3 Transformation

A variable transformation is used to remove the advective terms in Equation 3.56, to make it easily solvable. Ozsik [65] gave a generalized variable transformation of the

dependent variable ψ into a new dependent variable Ψ. Consider a Partial Differential Equation (PDE) with a dependent variable ψ as Equation 3.63:

$$\frac{\partial \psi}{\partial t} = \alpha_1 \frac{\partial^2 \psi}{\partial x^2} + \alpha_2 \frac{\partial^2 \psi}{\partial y^2} - \beta_1 \frac{\partial \psi}{\partial x} - \beta_2 \frac{\partial \psi}{\partial y} \tag{3.63}$$

where α and β are constants. A new dependent variable Ψ can be defined from ψ by multiplying ψ by an appropriate transformation parameter.

$$\Psi(x, y, t) = \psi(x, y, t) \exp[\frac{-\beta_1 x}{2\alpha_1} + \frac{\beta_1^2 t}{4\alpha_1}] \exp[\frac{-\beta_2 x}{2\alpha_2} + \frac{\beta_2^2 t}{4\alpha_2}] \tag{3.64}$$

Multiplying Equation 3.63 by the defined transformation parameter from Equation 3.64 results in;

$$\frac{\partial \Psi}{\partial t} = \alpha_1 \frac{\partial^2 \Psi}{\partial x^2} + \alpha_2 \frac{\partial^2 \Psi}{\partial y^2} \tag{3.65}$$

Equation 3.65, which does not have a advective term, is a result of a variable transformation of Equation 3.63. The dependent variable of the ADE C can be transformed to a new dependent variable c by multiplying by the transformation parameter defined below:

$$c(x, y, t) = C(x, y, t) \exp[\frac{-v_x x}{2D_L} + \frac{v_x^2 t}{4D_L}] \exp[\frac{-v_y y}{2D_T} + \frac{v_y^2 t}{4D_T}] \tag{3.66}$$

The resulting PDE after the variable transformation is given as below:

$$\frac{\partial c}{\partial t} = D_L \frac{\partial^2 c}{\partial x^2} + D_T \frac{\partial^2 c}{\partial y^2} \tag{3.67}$$

subject to the following boundary condition:

$$\begin{aligned} c(0,y,t) = C_0 \exp[\frac{v_x^2 t}{4D_L}] \exp[-\frac{v_y y}{2D_T} + \frac{v_y^2 t}{4D_T}] \qquad & at \qquad Y_1 < y < Y_2 \\ c = 0 \qquad & at \qquad y = 0, y = W \\ c = 0 \qquad & at \qquad x = L \\ c(x,y,t) = 0 & \end{aligned} \tag{3.68}$$

The partial derivative of x in Equation 3.67 is removed by applying the Fourier sine transform defined by Churchill [21] as:

$$S_\alpha F(x) = \int_0^\infty F(x) sin(\alpha x) dx = f_s(\alpha) \qquad (\alpha > 0) \tag{3.69}$$

whose basic operation property can be expressed as:

$$S_\alpha \frac{d^2 F(x)}{dx^2} = -\alpha^2 f_s(\alpha) + \alpha F(0) \tag{3.70}$$

The inverse of the finite sine transformation is given as:

$$S_\alpha^{-1} f_s(\alpha) = F(x) = \frac{2}{\pi} \int_0^\infty f_s(\alpha) \sin(\alpha x) d\alpha \qquad (x > 0) \tag{3.71}$$

The transformed equation, with its boundary and initial conditions is expressed as:

$$\frac{\partial c^*}{\partial t} + \alpha^2 D_L c^* - D_T \frac{\partial^2 c^*}{\partial y^2} = \alpha D_L C_0 \exp[\frac{v_x^2 t}{4D_L} + \frac{v_y^2 t}{4D_T}] exp[-\frac{v_y y}{2D_T}] \tag{3.72}$$

subject to the boundary and initial conditions:

$$\begin{cases} c^* = 0 & at \qquad y = 0, y = w \\ c^*(x, y, 0) = 0 \end{cases} \tag{3.73}$$

The partial derivative of y in Equation 3.72 is removed by applying the finite Fourier cosine transform defined by Churchill [22] as:

$$CF(y) = \int_0^W F(y) \cos(\frac{n\pi y}{W}) dy = f_c \qquad (0 < y < W) \tag{3.74}$$

whose basic operation property can be expressed as:

$$C\frac{\partial^2 F(y)}{dy^2} = (-1)^n \frac{dG}{dy}_{y=W} - \frac{dG}{dy}_{y=0} - (\frac{n\pi}{W})^2 f_c \tag{3.75}$$

The inverse of the Finite cosine transformation is given as:

$$C^{-1} f_c = \frac{f_c(0)}{W}_{n=0} + \frac{2}{W} \sum_{n=1}^{\infty} f_c(n) \cos(\frac{n\pi y}{W}) \tag{3.76}$$

let $\eta = \frac{n\pi}{W}$ nd applying the finite Fourier cosine transform:

$$\frac{dc^{**}}{dt} + (\alpha^2 D_L + \eta^2 D_T) c^{**} = \alpha D_L C_0 \exp[\frac{v_x^2 t}{4D_L} + \frac{v_y^2 t}{4D_T}] I_y \tag{3.77}$$

where:

$$I_y = \int_{Y_1}^{Y_2} exp[\frac{-v_y y}{2D_T} \cos(\eta y) dy] \tag{3.78}$$

The above integral is over Y_2 to Y_1 rather than from 0 to W because C_0 only has non-zero values between Y_2 to Y_1. Equation 3.77, which is the transformed Ordinary Differential Equation (ODE), is solved by an integrating factor. Given an ODE of the

form below:

$$\frac{d\omega}{dt} + g\omega = h(t) \tag{3.79}$$

the solution is given as (Wexler [93]):

$$\omega = \frac{1}{p(t)} \int_{t_0}^{t} p(\tau)h(\tau)d\tau + \omega_0 \frac{p(t)}{p(t_0)} \tag{3.80}$$

where $p(t)$ is the integrating factor and it is expressed as:

$$p(t) = \exp[\int g(\tau)d\tau] \tag{3.81}$$

Applying these equations to the transformed ODE gives:

$$p(t) = \exp[\int_0^t (\alpha^2 D_L + \eta^2 D_T)d\tau] = \exp[\alpha^2 D_L t + \eta^2 D_T t] \tag{3.82}$$

$$c^{**} = \frac{\alpha D_L C_0 I_y}{\exp[\alpha^2 D_L t + \eta^2 D_T t]} \int_{t=0}^{t} \exp[\alpha^2 D_L \tau + \eta^2 D_T \tau + \frac{v_x^2 \tau}{4D_L} + \frac{v_y^2 \tau}{4D_T}] \tag{3.83}$$

after integrating:

$$c^{**} = \frac{\alpha D_L C_0 I_y}{\alpha^2 D_L + \eta^2 D_T + \frac{v_x^2}{4D_L} + \frac{v_y^2}{4D_T}} \Big\{ \exp[\frac{v_x^2 t}{4D_L} + \frac{v_y^2 t}{4D_T}] - \exp[-\alpha^2 D_L t - \eta^2 D_T t] \Big\} \tag{3.84}$$

The inverse Fourier sine transform is applied to remove the α term.

$$\begin{aligned} c^{**} = C_0 I_y \Bigg\{ & exp[\frac{v_x^2 t}{4D_L} + \frac{v_y^2 t}{4D_T}] S_\alpha^{-1} \{ \frac{\alpha}{\alpha^2 + \eta^2 \frac{D_T}{D_L} + \frac{v_x^2}{4D_L^2} + \frac{v_y^2}{4D_L D_T}} \} \\ & - \exp[-\eta^2 D_T t] S_\alpha^{-1} \{ \frac{\alpha \exp[-\alpha^2 D_L t]}{\alpha^2 + \eta^2 \frac{D_T}{D_L} + \frac{v_x^2}{4D_L^2} + \frac{v_y^2}{4D_L D_T}} \} \Bigg\} \end{aligned} \tag{3.85}$$

The table of inverse Fourier sine transform in Churchill [22] is used to resolve the first inverse.

$$S_{\alpha}^{-1}\left\{\frac{\alpha}{\alpha^2+\eta^2\frac{D_T}{D_L}+\frac{v_x^2}{4D_L^2}+\frac{v_y^2}{4D_LD_T}}\right\}=\exp\left[-x\big(\alpha^2+\eta^2\frac{D_T}{D_L}+\frac{v_x^2}{4D_L^2}+\frac{v_y^2}{4D_LD_T}\big)^{1/2}\right] \tag{3.86}$$

There is no match for the second inverse transform in the inverse table. Therefore an integration of the form below is performed:

$$S_{\alpha}^{-1}\left\{\frac{\alpha\exp[-\alpha^2D_Lt]}{\alpha^2+\eta^2\frac{D_T}{D_L}+\frac{v_x^2}{4D_L^2}+\frac{v_y^2}{4D_LD_T}}\right\}=\frac{2}{\pi}\int_0^{\infty}\frac{\alpha\exp[-\alpha^2D_Lt]}{\alpha^2+\eta^2\frac{D_T}{D_L}+\frac{v_x^2}{4D_L^2}+\frac{v_y^2}{4D_LD_T}}\sin(\alpha x)d\alpha \tag{3.87}$$

The solution of this integral is as below (used from Gradshteyn and Ryzhik [35]):

$$\begin{aligned}S_{\alpha}^{-1}\left\{\frac{\alpha\exp[-\alpha^2a]}{\alpha^2+b^2}\right\}=\frac{2}{\pi}\Bigg\{-\frac{\pi}{4}\exp[ab^2]\Bigg[2\sinh(xb)\\ +\exp[-xb]erf[b\sqrt{a}-\frac{x}{2\sqrt{a}}]-\exp[xb]erf[b\sqrt{a}+\frac{x}{2\sqrt{a}}]\Bigg]\Bigg\}\end{aligned} \tag{3.88}$$

where:

$$\begin{aligned}a&=D_Lt\\ b&=(\eta^2\frac{D_T}{D_L}+\frac{v_x^2}{4D_L^2}+\frac{v_y^2}{4D_LD_T})^{1/2}\\ \sinh(xb)&=0.5(\exp[xb]-\exp[-xb])\end{aligned} \tag{3.89}$$

Re-arranging the equation gives,

$$\begin{aligned}S_{\alpha}^{-1}\left\{\frac{\alpha\exp[-\alpha^2a]}{\alpha^2+b^2}\right\}=\frac{1}{2}\exp[ab^2]\Bigg[\exp[-xb]erf[b\sqrt{a}-\frac{x}{2\sqrt{a}}]\\ -\exp[xb]erf[b\sqrt{a}+\frac{x}{2\sqrt{a}}]\Bigg]\end{aligned} \tag{3.90}$$

where $\text{erfc}(x) = 1 - erf(x)$. Substituting the inverse transform into the solution gives:

$$c^* = C_0 I_y \Bigg\{ \exp[\frac{v_x^2 t}{4D_L^2} + \frac{v_y^2 t}{4D_T} - x\gamma] - \frac{1}{2}\exp[\frac{v_x^2 t}{4D_L^2} + \frac{v_y^2 t}{4D_T}]\Big(\exp[-x\gamma]\text{erfc}\big[\gamma\sqrt{D_L t} - \frac{x}{2\sqrt{D_L t}} - \exp[x\gamma]\text{erfc}\big[\gamma\sqrt{D_L t} + \frac{x}{2\sqrt{D_L t}}\big]\Big)\Bigg\} \tag{3.91}$$

Using the identity $\text{erfc}(-x) = 2 - \text{erfc}(x)$, equation can be simplified:

$$c^* = C_0 I_y \Bigg\{ \frac{1}{2}\exp[\frac{v_x^2 t}{4D_L^2} + \frac{v_y^2 t}{4D_T}]\Big(\exp[-x\gamma]\text{erfc}\big[\frac{x - 2D_L t\gamma}{2\sqrt{D_L t}} + \exp[x\gamma]\text{erfc}\big[\frac{x + 2D_L t\gamma}{2\sqrt{D_L t}}\big]\Big)\Bigg\} \tag{3.92}$$

The integral I_y can be simplified with the following conditions. When $v_y = 0$ and $n = 0$:

$$I_{y,v_y=0,n=0} = \int_{Y_1}^{Y_2} dy = Y_2 - Y_1 \tag{3.93}$$

if $v_y \neq 0$ and $n = 0$:

$$I_{y,n=0} = \int_{Y_1}^{Y_2} \exp[\frac{-v_y y}{2D_T}]dy = \frac{2D_T}{v_y}\Big\{ \exp[\frac{-v_y Y_1}{2D_T}] - \exp[\frac{-v_y Y_2}{2D_T}]\Big\} \tag{3.94}$$

and for $n > 0$:

$$I_{y,n>0} = \int_{Y_1}^{Y_2} \exp[\frac{-v_y y}{2D_T}]\cos(\eta y)dy = \frac{1}{\big(\frac{-v_y}{2D_T}\big)^2 + \eta^2}$$
$$\Bigg\{ \exp[\frac{-v_y Y_2}{2D_T}]\Big(\eta\sin(\eta Y_2 - \frac{v_y\cos(\eta Y_2)}{2D_T}\Big) - \exp[\frac{-v_y Y_1}{2D_T}]\Big(\eta\sin(\eta Y_1 - \frac{v_y\cos(\eta Y_1)}{2D_T}\Big)\Bigg\}. \tag{3.95}$$

Applying the inverse finite Fourier cosine transform and simplifying; we obtain:

$$c = \frac{C_0}{W}\sum_{n=0}^{\infty} L_n P_n \cos(\eta y)\exp[\frac{v_x^2 t}{4D_L^2}+\frac{v_y^2 t}{4D_T}]\Bigg(\exp[-x\gamma]\mathrm{erfc}\big[\frac{x-2D_L t\gamma}{2\sqrt{D_L t}} + \exp[x\gamma]\mathrm{erfc}\big[\frac{x+2D_L t\gamma}{2\sqrt{D_L t}}\big]\Bigg). \tag{3.96}$$

The dependent variable c is transformed back to C by multiplying by the transformation parameter:

$$C(x,y,t) = c(x,y,t)\exp[\frac{v_x x}{2D_L}-\frac{v_x^2 t}{4D_L}]\exp[\frac{v_y y}{2D_T}-\frac{v_y^2 t}{4D_T}] \tag{3.97}$$

The final solution is:

$$C(x,y,t) = \frac{C_0}{W}\sum_{n=0}^{\infty} L_n P_n \cos(\eta y)\exp[\frac{v_x x}{2D_L}+\frac{v_y y}{2D_T}]\Bigg(\exp[-x\gamma]\mathrm{erfc}\big[\frac{x-2D_L t\gamma}{2\sqrt{D_L t}} + \exp[x\gamma]\mathrm{erfc}\big[\frac{x+2D_L t\gamma}{2\sqrt{D_L t}}\big]\Bigg) \tag{3.98}$$

where:

$$
\begin{aligned}
L_n &= \begin{cases} \frac{1}{2} & n = 0 \\ 1 & n > 0 \end{cases} \\
P_n &= \begin{cases} I_{y,v_y=0,n=0} & v_y = 0, n = 0 \\ I_{y,n=0} & v_y \neq 0, n = 0 \\ I_{y,n>0} & n > 0 \end{cases} \\
\gamma &= \big(\eta^2 \frac{D_T}{D_L} + \frac{v_x^2}{4D_L^2} + \frac{v_y^2}{4D_L D_T}\big)^{1/2} \\
\eta &= \frac{n\pi}{W} \\
I_{y,v_y=0,n=0} &= Y_2 - Y_1 \\
I_{y,n=0} &= \frac{2D_T}{v_y}\Big\{ \exp[\frac{-v_y Y_1}{2D_T}] - \exp[\frac{-v_y Y_2}{2D_T}]\Big\} \\
I_{y,n>0} &= \frac{1}{\big(\frac{-v_y}{2D_T}\big)^2 + \eta^2}\Bigg\{ \exp[\frac{-v_y Y_2}{2D_T}]\Big(\eta \sin(\eta Y_2 - \frac{v_y \cos(\eta Y_2)}{2D_T}\Big) \\
&\quad - \exp[\frac{-v_y Y_1}{2D_T}]\Big(\eta \sin(\eta Y_1 - \frac{v_y \cos(\eta Y_1)}{2D_T}\Big)\Bigg\}
\end{aligned}
\tag{3.99}
$$

In the following, this solution will be implemented in the *Athena Visual Studio* solver to estimate the experimental dispersion coefficients.

3.9 Numerical Solution

In this section, the numerical approach has been applied to find the longitudinal and transverse dispersion coefficients during a miscible displacement in 2D porous media. In many industrial applications the advection-diffusion equation is often discretized

by finite difference methods (FDM) or finite element methods (FEM). The statistically calculated dispersion coefficients for each model is implemented in the numerical simulation to compare with the experimental output.

3.9.1 Assumptions

The same assumptions, initial, and boundary conditions as section 3.8 applies in this solution that is summarized as below:

- Assumptions:
    1. Inlet pressure (P_1) and outlet pressure (P_2) are constant.
- Initial conditions:
    1. $\forall x, y \Rightarrow C(x, y, 0) = 0$
- Boundary conditions:
    1. $C = 0$ at $y = -W/2$, $y = +W/2$
    2. $C = 0$ at $x = L$
    3. $C(0, 0, t) = C_0$

3.9.2 Methodology

Equation 3.100 presents the assumed mathematical model for miscible displacement in porous medium with defined assumptions. The set of equations is solved using a upwind numerical approximation.

$$\frac{\partial C}{\partial t} + \underbrace{v\frac{\partial C}{\partial x}}_{\text{advection}} - \underbrace{D_L\frac{\partial^2 C}{\partial x^2}}_{\text{Longitudinal dispersion}} - \underbrace{D_T\frac{\partial^2 C}{\partial y^2}}_{\text{Transverse dispersion}} = 0 \tag{3.100}$$

The solution domain of the problem is covered by a mesh of grid-lines:

$$\begin{aligned} x_i &= i\Delta x & i &= 1, 2, ..., M & \Delta x &= \frac{L}{M} \\ y_j &= j\Delta y & j &= 0, 1, ..., K & \Delta y &= \frac{W}{K} \\ t_n &= n\Delta t & n &= 0, 1, ..., N & \Delta t &= \frac{T}{N} \end{aligned}$$

where x_i, y_j and t_n are parallel to the space and time coordinate axes. For a better understanding of the sensitivity of the solution, the dimensionless formulation of the transport equation is used. The dimensionless parameters are defined as below:

$$x_D = \frac{x}{L} \qquad \text{dimensionless x-coordinate} \tag{3.101}$$

$$y_D = \frac{y}{W} \qquad \text{dimensionless y-coordinate} \tag{3.102}$$

$$C_D = \frac{C}{C_0} \qquad \text{dimensionless concentration} \tag{3.103}$$

$$t_D = \frac{vt}{L} \qquad \text{dimensionless time} \tag{3.104}$$

The advection-diffusion equation in dimensionless form is as below:

$$\frac{\partial C_D}{\partial t_D} + \frac{\partial C_D}{\partial x_D} - \frac{D_L}{Lv}\frac{\partial^2 C_D}{\partial x_D^2} - \frac{D_T}{Lv}\frac{\partial^2 C_D}{\partial y_D^2} = 0 \tag{3.105}$$

When an increased concentration C_{Di}^n enters the first cell with the flow, that affect the concentration distribution in the entire system. To keep it simple it is assumed that the concentration in each cell has a single value. The concentration in the $i-th$ cell at the time step n^{th} is designated as C_{Di}^n. The transport problem is to compute the concentrations C_{Di}^n, depending on time and the transport parameters. Consider the following approximations of the derivatives in the ADE in x-direction

which incorporate time and space as follows:

$$\begin{aligned}
\frac{\partial C_D}{\partial t_D} &= \frac{C_{Di}^{n+1} - C_{Di}^{n}}{\Delta t_D} && n = 0, 1, 2, 3, ..., N \\
\frac{\partial C_D}{\partial x_D} &= \frac{C_{Di+1}^{n} - C_{Di-1}^{n}}{2\Delta x_D} && i = 1, 2, 3, ..., M+1 \\
\frac{\partial^2 C_D}{\partial x_D^2} &= \frac{C_{Di+1}^{n} - 2C_{Di}^{n} + C_{Di-1}^{n}}{{\Delta x_D}^2} \\
\frac{\partial^2 C_D}{\partial y_D^2} &= \frac{C_{Dj+1}^{n} - 2C_{Dj}^{n} + C_{Dj-1}^{n}}{{\Delta y_D}^2}
\end{aligned}$$

substituting in Equation 3.105 results in:

$$\frac{C_{Di}^{n+1} - C_{Di}^{n}}{\Delta t_D} + \frac{C_{Di+1}^{n} - C_{Di-1}^{n}}{2\Delta x_D} - \frac{D_L}{Lv}\left(\frac{C_{Di+1}^{n} - 2C_{Di}^{n} + C_{Di-1}^{n}}{\Delta x_D^2}\right) - \frac{D_T}{Lv}\left(\frac{C_{Dj+1}^{n} - 2C_{Dj}^{n} + C_{Dj-1}^{n}}{\Delta y_D^2}\right) = 0 \quad (3.106)$$

The Figure 3.8 illustrates the solution approach for this modeling. The numerical

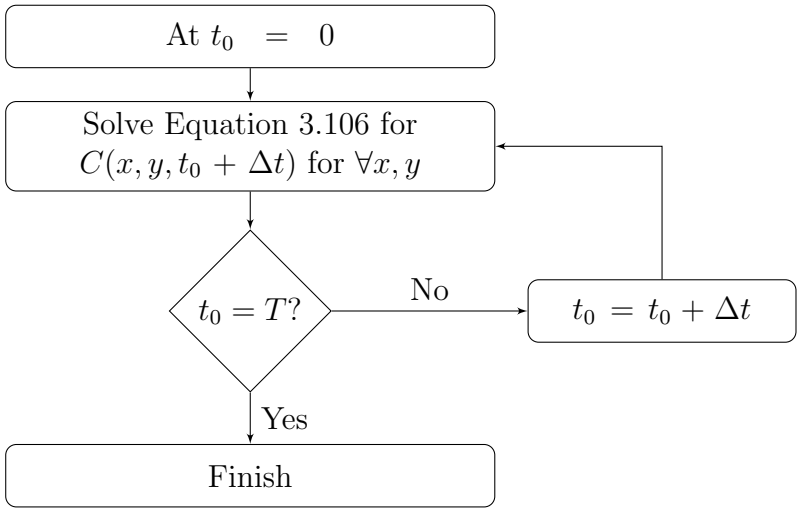

Figure 3.8: Solution approach for numerical simulation in 2D porous media

scheme needs to move in the same direction as the differential equation. Upwind schemes are designed to do it as described: Generally, it has been proved that accu-

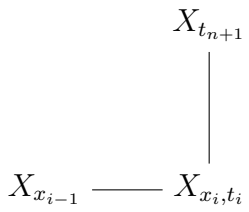

Figure 3.9: Forward differences, if the velocity is positive

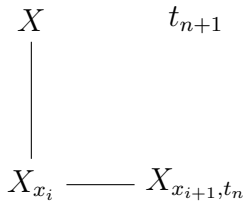

Figure 3.10: Backward differences, if velocity is negative

racy of the numerical methods are acceptable if the initial and boundary conditions are properly defined [27]. This is discussed in details in next chapter.

3.10 Experimental Study

This sections uses an experimental approach with a new image processing technique to find the longitudinal and transverse dispersion occurring during miscible displacement in a randomly generated two dimensional porous medium. In this study, we have a high resolution digital camera to detect fluid concentrations using a newly developed pixel resolution image analysis method. We use a novel custom developed pixel resolution image analysis method to estimate the coupled longitudinal and transverse dispersivity coefficients. In the following, micromodel flooding experiments are designed to evaluate the validity of the obtained mathematical model using statistical and numerical approaches. The determination of dispersivity coefficients through experimentation has been extensively developed for a single dispersivity in either the

longitudinal or transverse directions in the past. From the most influential studies, Silliman et al. (1987) [80] investigated the longitudinal dispersion in anisotropic porous media using sodium chloride as a tracer, and then found a relationship between dispersion and hydraulic anisotropy. Aksoy and Guney (2010) [2] investigated the longitudinal and transverse dispersivities reproducing a homogeneous 3-5 mm sandy aquifer. Kim et al. (2004) [53] conducted a laboratory tracer test representing a two-dimensional aquifer with the aim of estimating the longitudinal dispersivity (D_L) and the ratio ($\frac{D_T}{D_L}$) of transverse to longitudinal dispersivity of sandy aquifer material. Miscible dyed-water and water injections in a glass micromodel have been used in this study to investigate the **coupled** longitudinal and transverse dispersion. In the following, a unique pixel resolution image processing technique is used along with a Beysian estimator tool to fit the experimental results with analytical solution of the Advection-Diffusion Equation (ADE) introduced in Equation 3.8. The used method has following advantages compared to traditional methodologies:

- The developed image processor has the advantage that inferences and predictions fully include parameter uncertainty. The Bayesian estimator tool collects data from spatially random locations.

- Decreasing inconsistency of image processing using advanced colour calibrations to overcome inconsistencies in back lighting as well as intensity variation due to pore depth (since the sides of the pore and pore throats are not the same depth of etching as the center).

- Decreasing the random errors of manual selection and cropping of the images.

3.11 Materials

The materials used in this study are classified in three groups of chemicals, apparatus, and instruments. **Chemicals** include distilled water and distilled dyed-water. The physical properties of test fluids and materials at room temperature (25°C) and ambient pressure (14.7 psi) are shown in Table 3.1. Properties of the distilled clear and dyed-water are illustrated in Table 3.1. The apparatuses include a Cole Parmer® 880195 syringe pump, micromodel holder, Porta Trace® fluorescent light-box, and Swagelok® tubing, valves, fittings, tee, caps, plugs, nuts, male and female connectors and Teflon tape. Instruments include cylinder, OMEGA® OM-CP-PRTEMP1000 pressure transducers, 200 mL graduated cylinders, weighing paper, and an EOS 6D Canon digital camera connected to computer with 100 mm Macro lens (Table 3.2). Figure 3.11 shows a schematic of the experimental set up for this study. A high inten-

Table 3.1: Chemical and physical properties of water at room temperature ($25°C$) and ambient pressure (14.7 psi) [69].

Chemical Formula	**Polarity**	**Density** (g/cm^3)	**Viscosity** (cP)
H_2O	Polar	0.997	0.894

Table 3.2: Apparatus and required instruments for experiments

Apparatus	**Instruments**
Syringe pump (Cole Parmer 880195)	Graduated cylinder
Micromodel	Pressure transducer
Micromodel holder	Digital Camera
Tubing	
Fittings	
Caps	
Valves	
Nuts	
Plugs	

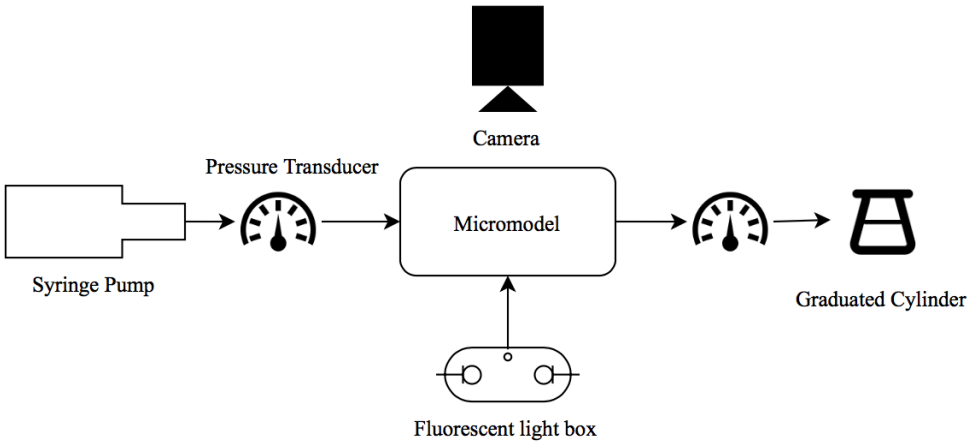

Figure 3.11: Experimental set up

sity halogen light source had to be used to supply enough illumination since the light will be powerful enough to be transmitted through the model. All required equipment and supplies are available in the Hibernia EOR lab.

3.12 Calculation of Experimental Parameters

Various experimental parameters have been used in the experimental analysis including total pore volume, cross-sectional are, pore depth, injection area, porosity, absolute permeability, effective width of the porous medium and injection velocity. In the following, the measurement of all parameters are explained.

3.12.1 Pore volume

The pore volumes of both glass micromodels were determined by flooding a dyed liquid into the porous domain through a syringe pump. The volume injected to fill the whole domain represents the total pore volume of a micromodel.

3.12.2 Average pore depth

The depth of the micromodels refers to the average distance between the flat glass surface and the sandblasted etched surface in which the fluid flowed. The calculation of this parameter is required because the actual depth of cut after the etching operation was unknown. The pore depth was obtained by dividing the total pore volume by the surface area of the whole domain.

3.12.3 Average pore and grain diameter

The average pore and grain diameter of the micromodel were estimated using the developed image processing program. For this purpose, the captured image of the fully saturated micromodel with dyed water was analyzed and the cumulative pore and grain size distribution were obtained. Calculating the average pore and grain diameter using image analysis was used to estimate the average pore diameter with a reasonable accuracy of $\pm 10\%$ using a pore portioning algorithm in the image processing program. To improve the accuracy, knowledge of the pore morphology is used to refine the pore portioning algorithm.

3.12.4 Cross-sectional area

The cross-sectional area of the inlet channel was determined by multiplying the width and the depth of the inlet port. The width of the inlet channel of both micromodels was adjusted by 800 μm during the designing of the patterns. This cross-sectional area was used in the simulation study in order to specify the inlet velocity.

3.12.5 Effective width

The effective width is the average width available to the fluids to propagate in the grains domain. This can be obtained by using the following relation:

$$Effective\ width = \phi \times W \tag{3.107}$$

where ϕ is the porosity and the W is the width of the porous medium.

3.12.6 Porosity

The porosity estimation in micromodel is a ratio rather than a percentage and is characterized as the ratio between the surface area and the total area. Therefore, to calculate the porosity of micromodels in this study, 100% dyed water was injected and the captured image was analyzed to find the dyed area and surface area.

$$\phi = \frac{Saturated\ area\ with\ dyed\ water}{Total\ surface\ area} \tag{3.108}$$

3.12.7 Absolute permeability

Absolute permeability of micromodel was achieved by measurement of pressure drop in the micromodel during a known constant injection rate and using Darcy law. We followed the steps below in this order:

1. The micromodel was fully saturated with clear water.

2. The clear water was injected at two different injection rates by the and the pressure drop across the micromodel length was measured by inlined pressure transducers at each injection rate.

3. The absolute permeability was calculated from the Darcy Law as below:

$$K = Q\frac{\mu L}{A\Delta P} \tag{3.109}$$

Where K is absolute permeability, Q is injection rate, L is length of the micromodel, A is cross-sectional area from Section 3.12.4, and ΔP is the pressure drop during water injection.

3.12.8 Description of the Models

A porous medium can be defined and classified according to its pore geometry and structure, considering this character, porous medium is defined to be either homogeneous or heterogeneous at the macroscopic level. Properties at the macroscopic level are averaged over a sufficiently large volume, called the macroscopic averaging volume, to define continuous, stable functions of spatial position [8]. A homogeneous medium contains two subcategories uniform or non uniform. A uniform homogeneous medium with has the same pore size and shape distribution, whereas a nonuniform porous medium contains variations in grain scale pore structure, but is homogeneous at the macroscopic level for quantities such as the permeability or porosity [51]. A porous medium is also either isotropic or anisotrpic at the macroscale. In an isotropic porous media properties do not vary with direction; in anisotropic porous media properties vary directional [31]. In this study two different porous media have been selected with single and dual permeabilities. In the following, the two different porous media are explained in detail.

3.12.9 Single Permeability Medium

One of the selected porous media in this study is a homogeneous, non uniform, anisotropic type. ADE is found to be valid for the medium. Although the mechanisms of dispersion are the same, non uniformity and heterogeneity provide greater variations in solute speed and tortuosity. The result of this is increased dispersion in non-uniform media. For heterogeneous, isotropic porous media, a generalization of the ADE is possible if the spatial variations of all the macroscopic properties are known. The effects of anisotropy on miscible mass transport are not completely understood therefore it is selected in this study. Even heterogeneous porous media is often modeled as a homogeneous media with an overall mean flow direction and macroscopic dispersion coefficient, since data on the exact nature of the heterogeneity are usually not available.

Figure 3.12 shows the pore size distribution for the fabricated micromodel. The distribution is a log-normal Probability Distribution Function (PDF) with a sharp peak that implies as a great fourth moment so-called Kurtosis that appeared in statistical modeling results as in Equation 4.11c and 4.11d. The qualitative or quantitative interpretation of the kurtosis is complicated and unintuitive, however, in this study, we tried to relate it pore geometry of porous media. Table 3.3 illustrates the properties of the single permeability micromodel in this study. Table 3.4 shows the designated objectives along with gapsin this study.

Table 3.3: Properties of the fabricated micromodel, where W is width, L is length, ϕ is porosity, K is absolute permeability, R_{ave} is average pore diameter, D_{ave} is average pore depth, r_{ave} is average grain diameter, $P.V.$ is estimated pore volume

W (cm)	L (cm)	ϕ (%)	K (mD)	R_{ave} (mm)	D_{ave} (mm)	r_{ave} (mm)	$P.V.$ (cm^3)
16	32	48%	787	0.63	0.23	3.33	11.5

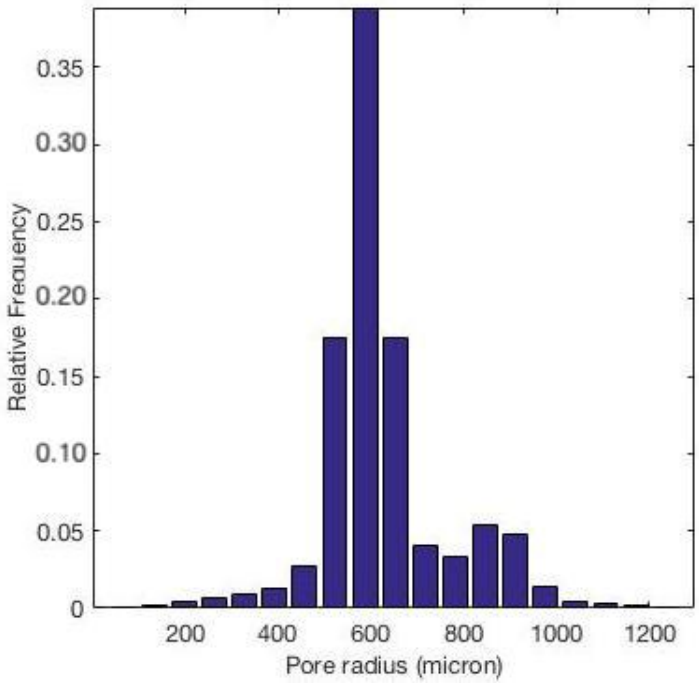

Figure 3.12: Histogram of Pore Size Distribution for the single permeability porous medium

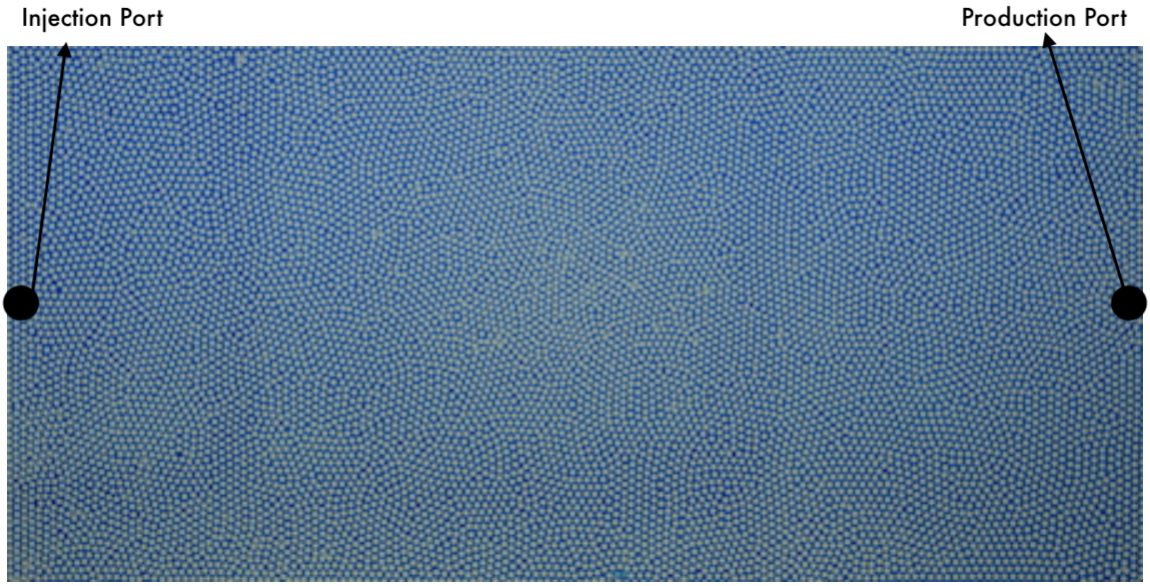

Figure 3.13: Glass micromodel fabricated with single permeability porous medium-saturated with dyed water

Table 3.4: Advantages and disadvantages of the miscible displacement experiments in a single permeability porous medium

Advantages
1- Miscible injection tests at 5 different velocities to determine the experimental relationship of the coupled dispersion coefficients (longitudinal and transverse) in two dimensional
2- The experimental results are used to validate the predicted mathematical results achieved from the developed statistical approach and compared to previous models
Disadvantages
1- Only one micromodel has been used in this study to investigate the effect of pore properties

3.12.10 Dual Permeability Medium

In the field scale of oil reservoirs, the formations are typically dual media, as dominated by a primary permeability system and affected by a secondary permeability or in some cases fractures. In this section, the assumed two-dimensional porous medium, which consists of high permeability (1) and low permeability (2) regions merged in one single medium, has been explained in details. In this model, inlet pressure (P_1) and outlet pressure (P_2) are constant and high permeability region is very low in height (h) (assumed 1D) and region 2 is higher in height (H) and considered two dimensional ($h << H$). The comparison of properties of two regions is shown in Table 3.5. The calculation of the experimental parameters are explained in the Section 3.12. As Figure 3.15 illustrates the region 2 or low permeability zone has a stronger peak double exponential pore size distribution. Although the high permeability zone (region 1)

has a wider and smooth peak (Figure 3.16) in overall the porous medium has strong peak with more rapid decay.

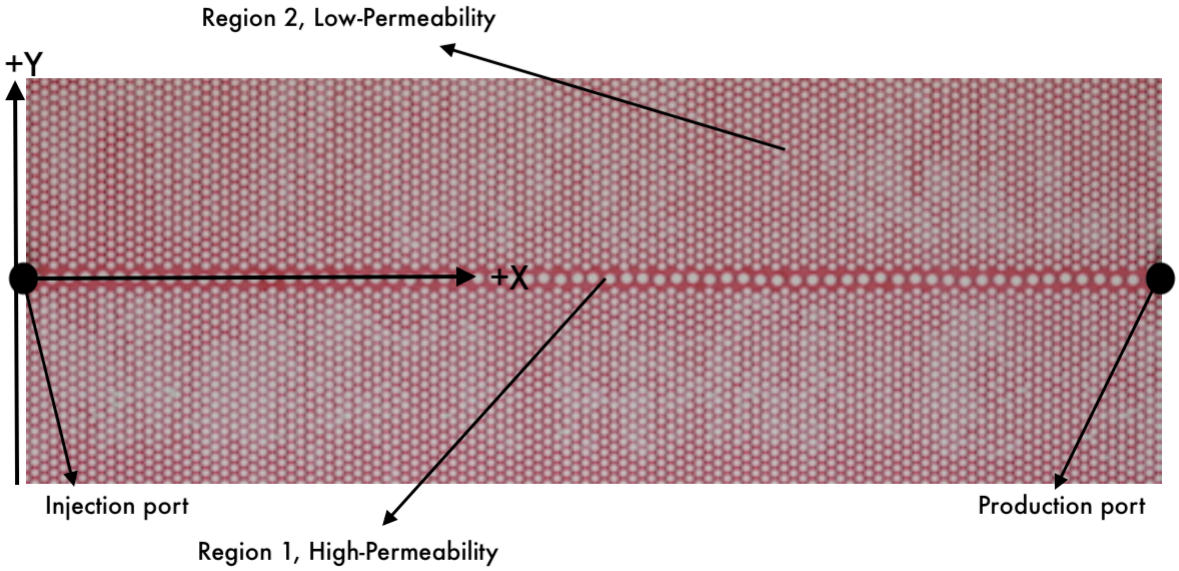

Figure 3.14: Glass micromodel fabricated with dual permeability porous medium, Saturated with dyed (red) water

Table 3.5: Properties of the fabricated dual permeability micromodel, W is width, L is length, ϕ is porosity and K is absolute permeability

Region	K (D)	ϕ (%)	L (cm)	W (cm)	R_{ave} (mm)	D_{ave} (mm)	$P.V.$ (cm^3)
1	5.6	52.2	32	0.5	1.35	0.28	0.45
2	1.8	39.6	32	6×2	0.68	0.23	8.83
Overall	1.9	40.4	32	12.5	0.68	0.23	9.28

Figures 3.5 and 3.14 show the dual permeability porous medium in a assumed and actual design, respectively. This approach can be applied in simulation of heterogeneity and its effect on longitudinal and transverse dispersion in miscible displacements. Figure 3.15, 3.16, and 3.17 show the pore size distribution for the fabricated dual permeability micromodel. The distribution for low permeability region is log-normal Probability Distribution Function (PDF) with a sharp peak that is similar to single

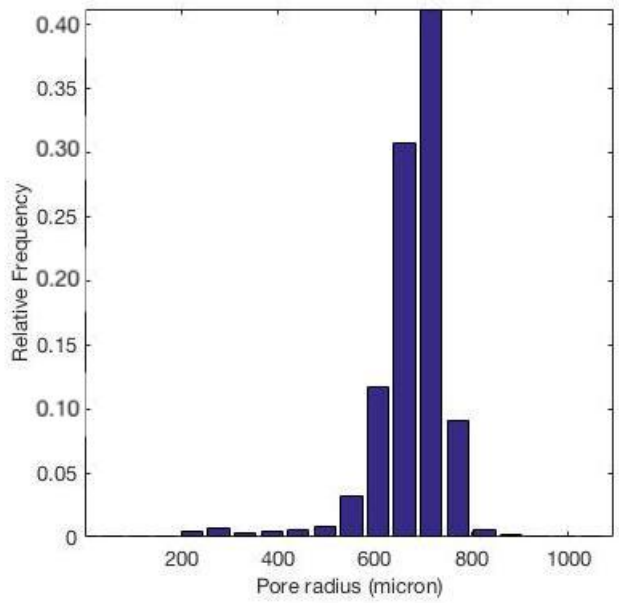

Figure 3.15: Histogram of the pore size distribution for the dual permeability porous medium, low permeability, region (2)

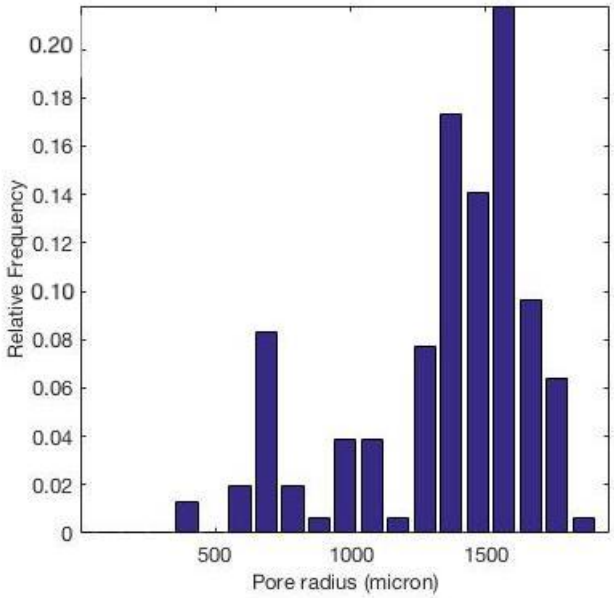

Figure 3.16: Histogram of pore size distribution for the dual permeability porous medium, high permeability, region (1)

permeability porous medium. The high permeability region has a wider distribution with β distribution. The beta distribution implies the behavior of random variables

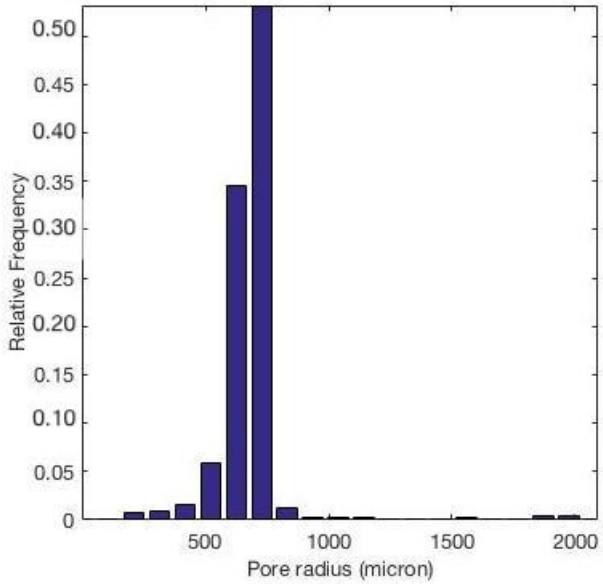

Figure 3.17: Histogram of pore size distribution for the dual permeability porous medium, coupled high and low permeability zones

limited to intervals of finite length in a wide variety of disciplines (pore size). In Figure 3.17 we see the over PDF looks like log-normal function again but with less sharp peak. Table 3.5 illustrates the properties of the used single permeability micromodel in this study. Table 3.6 shows the objectives along with gaps in this study for dual permeability porous medium.

Table 3.6: Objectives of the miscible displacement experiments in dual permeability porous medium

Advantages
1- Miscible injection tests are studied at 5 different velocities to determine the experimental relationship of the coupled dispersion coefficients (longitudinal and transverse) in two dimensions
2- The experimental results are used to validate the predicted mathematical results achieved from the numerical and statistical approaches
Disadvantages
1- The effect of the pore scale properties is characterized using permeability instead of detailed pore structure properties

3.13 Micromodel Fabrication

The glass micromodels were custom designed and manufactured for this study. Below, details of the glass micromodel preparation and the experimental procedure followed are discussed. Figure 3.18 shows the overall steps in fabrication of micromodel. As a

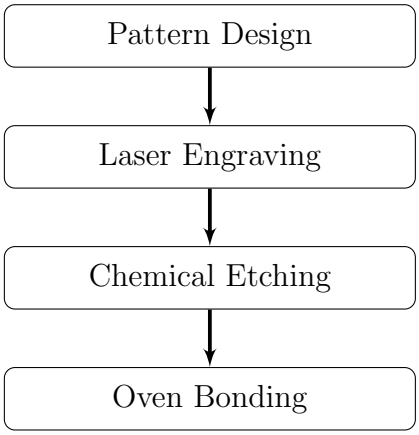

Figure 3.18: Micromodel fabrication procedure

first step to design the pattern, a program was developed to account for the influence of particle aspect ratio, area fraction, and orientation on representative length scales in two dimensional porous medium. This program includes the ability to generate the solid particles with various distributions of particle sizes and orientations. In this program the directional form is used to assess the directional dependence of the length scale of the underlying structure. Patterns can be directly designed with lines/pixels with a variety of methods using any software. In this study Adobe Illustrator and a custom developed Java code are used. The program was applied for distribution of grains in the two dimensional medium.

For laser engraving the ©Trotec Speedy 300 with the configuration shown in Table 3.7 was used. Glass etching can be done by applying a cream such as Armour Etch or

Table 3.7: Applied configuration for laser engraving. PPI is Pulse Per Inch

Material	Applied Speed	Applied Power	Applied PPI
Glass	$35cm/s$	$15W$	1000

soaking the engraved plate in a liquid acidic bath (has been used in this study). The depth of penetration depends on the etching rate of the acid and time. Consequently, the type of cream used and the exposure time are determined by trial and error. The desired depth is 200 to 300 μm and it was determined that approximately 90 minutes of etching was required. In the following, the etched glass plate must be bounded to another plate (same material/same size). The is ramped to achieve optimal smooth bonding, as illustrated in Table 3.8.

3.14 Experimental Procedure

In this section the experimental procedures are described. The micromodel has two ports. One is used for fluid injection and the other one is used as production port.

Table 3.8: Applied configuration for oven bonding with a $1\frac{^{\circ}C}{min}$ heating and cooling rate

Level	Applied Temperature ($^{\circ}C$)	Applied Time (hr)
Level I	$85 - 90$	$12 - 24$
Level II	$125 - 140$	$24 - 48$
Level III	Cooling down	$12 - 24$

The micromodel is placed between two frames. The upper frame has two holes to allow access to the two ports on the micromodel. In the system, cleaning fluids and test fluids are pumped through the micromodel using a pump. The syringe pump is used to inject the clear and dyed water. Good control of flow rates and absence of pressure pulsing are essential during the micromodel test. Injection of dyed water and fully saturation of the micromodel is needed for calculation of porosity and absolute permeability. To avoid trapping any air bubbles, the dyed-water injection rate is high initially and then decreased to ensure full saturation. The miscible flood is then conducted by injecting clear water while taking a high quality picture every 60 seconds (1 min) The custom pixel-level image processing technique is used to analyze the pictures and calculate the longitudinal and transverse dispersion components. Figure 3.19 illustrates the taken steps for experimental procedure. During the miscible displacement tests, we do not have a distinct interface between the displacing and displaced fluids. However, a mixing zone exists between the pure displacing fluid and the displaced fluid. The mixing zone contains a range of concentrations from zero (a clear displacing fluid) to 100 (a pure displaced fluid). Images taken during miscible injection at known times are used to approximate the concentration profile. The most challenging part is distinguishing the concentration of the solvent across the porous medium; this requests a strong calibration of color intensity. To relate the different colors to corresponding concentrations, several images will be taken to

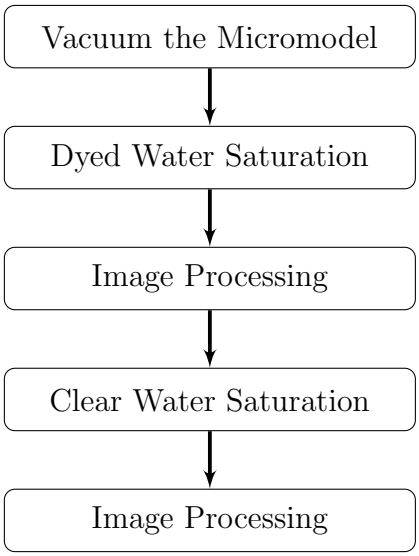

Figure 3.19: Experimental procedure for miscible displacement experiments

obtain a unique correlation (explained in details in Section 3.15.1). A specific color identifies a particular concentration. After extracting the concentration profile, the longitudinal and transverse dispersion will be estimated by fitting the experimentally measured transient solute concentration profiles with the aid of the Bayesian estimator to an analytic solution of Equation 3.98. Figure 3.20 illustrates the cropped raw image (A), selected-analyzed mask image (B) and processed image (C).

3.15 Image Processing

The dispersion calculations for miscible displacements in experimental studies of transport process are challenging to the difficulty of measuring concentration at a particular location. Recently, the availability of high-quality digital images and image processing tools made the development of new techniques for the investigation of the dispersivity coefficients in 2D more possible. This section shows the application of new image processing technique, along with a matching tool that allows a detailed estimation of longitudinal and transverse dispersion coefficients in experimental studies. The

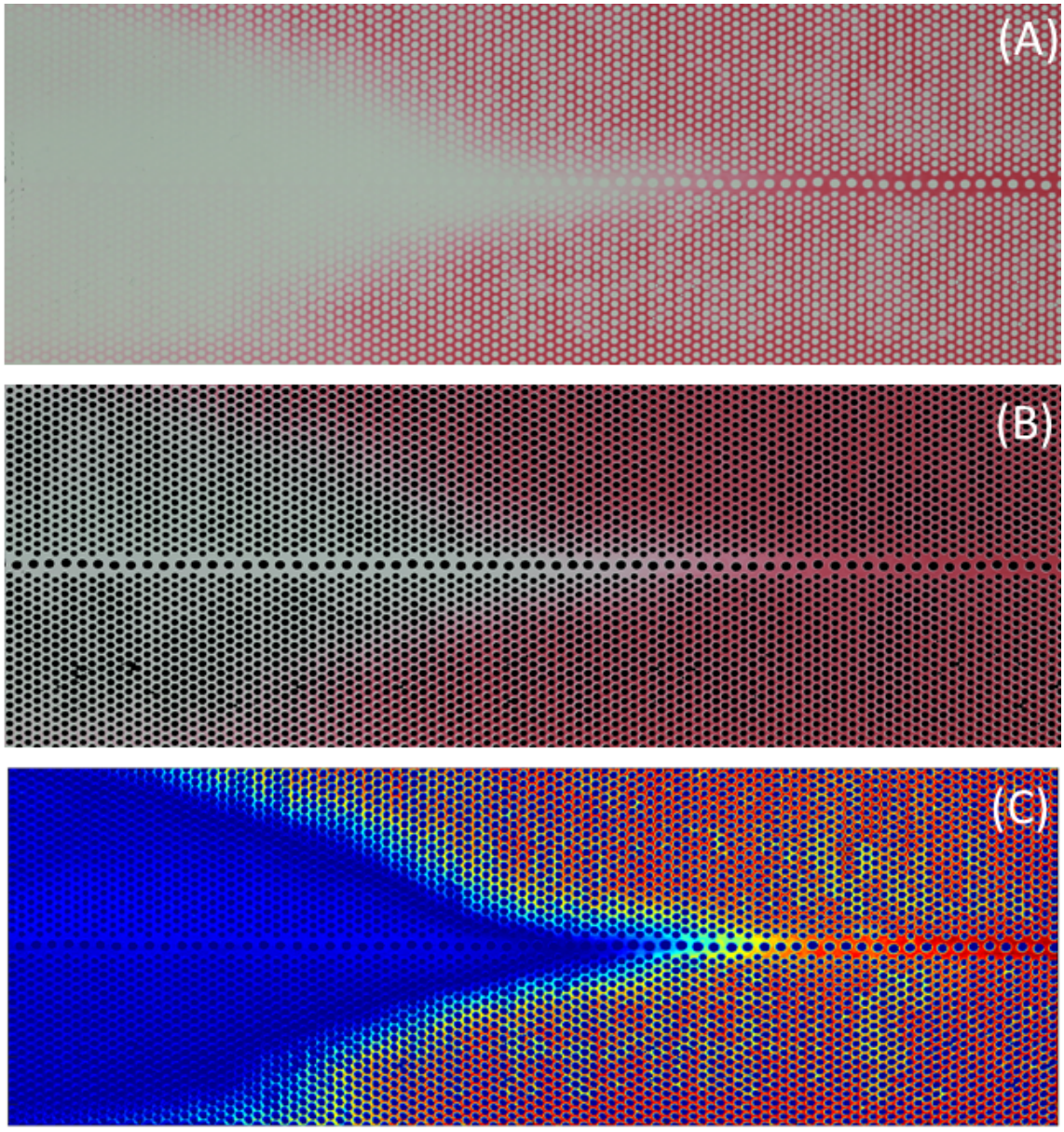

Figure 3.20: Image processing technique- (A) is the cropped raw image, (B) is selected-analyzed mask image, and (C) is processed image at 0.02 $\frac{cc}{min}$

developed methodology uses various images of fully saturated media with multiple known saturations for the concentration calibration and accurately identifying the color changes in mixing zones. The program is then rendered with captured pictures

with known time intervals during the displacement and to implement a unique technique for estimating the concentration map. In the following, processed images are converted to data sets and the program matches the results with the analytical solution of (Advection-Diffusion Equation) ADE using Bayesian estimator technique. In the following, the averaging technique is applied to filter the unreliable pixels and average the estimated dispersivities for each pixel. Despite the more number of calculations, the proposed method provides more accurate and detailed results along with faster processing time. The method has also the advantage of extendibility to work from homogeneous to heterogeneous media.

3.15.1 Colour calibration

The proposed technique is based on the combination of image processing algorithms and the analytical solution of ADE. Figure 3.21 shows the designed steps for calculation of longitudinal and transverse dispersion from taken images during miscible displacement. During the miscible displacement tests, we do not have a distinct interface between the displacing and displaced fluids. However, a mixing zone exists between the pure displacing fluid and the displaced fluid. The mixing zone contains a range of concentrations from zero (a pure displacing fluid) to 100 (a pure displaced fluid). Images taken during miscible injection at known times are used to approximate the concentration profile. The most challenging part is distinguishing the concentration of the solvent across the porous medium; this requests a strong calibration of color intensity. For this purpose, a MATLAB code has been developed which is used to measure the percentage of the specific pattern covered with the fluid based on the color (3.27). The code provided has two input parameters of reference image containing image of the grid pattern fully saturated with dyed water and folder containing

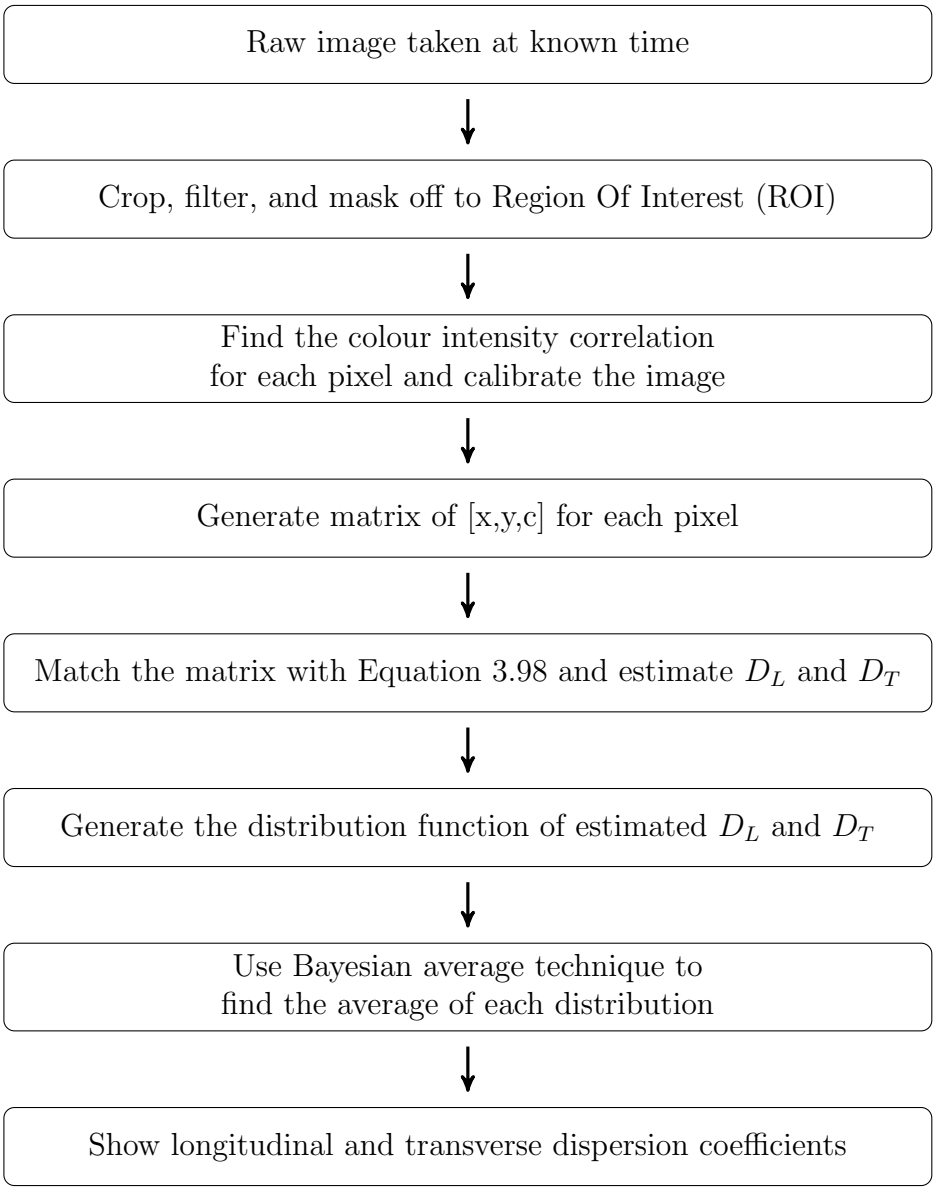

Figure 3.21: Image processing procedure for miscible displacements in 2D micromodel

images of the same grid pattern on different stages of the miscible displacement experiment. The output should contain the measurement (in percents from the area of the grid) of different degrees of fluid coverage.

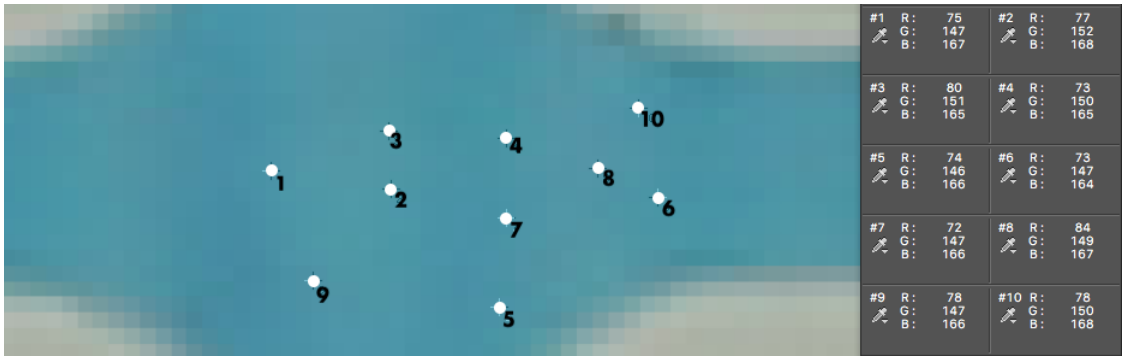

Figure 3.22: Randomly selected RGB values in different sample points for the same saturation (25% blue dyed water)

Table 3.9: RGB values in different randomly selected sample points for same saturation of 25% blue dyed water

Pixel	1	2	3	4	5	6	7	8	9	10
R	75	77	80	73	74	73	72	84	78	78
G	147	152	151	150	146	147	147	149	147	150
B	167	168	165	165	166	164	166	167	166	168

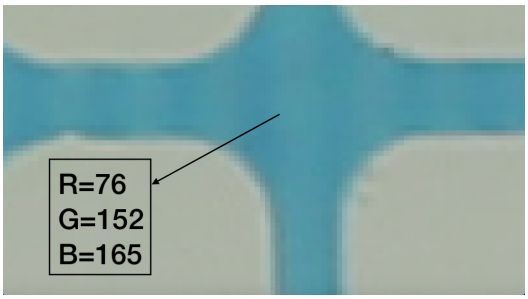

(a) 25% Saturation

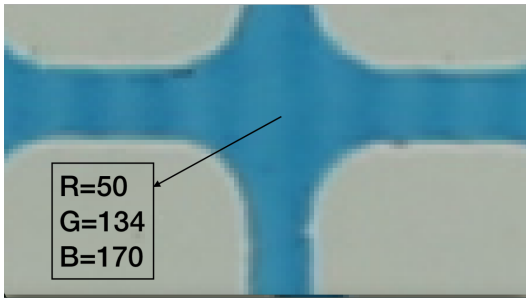

(b) 50% Saturation

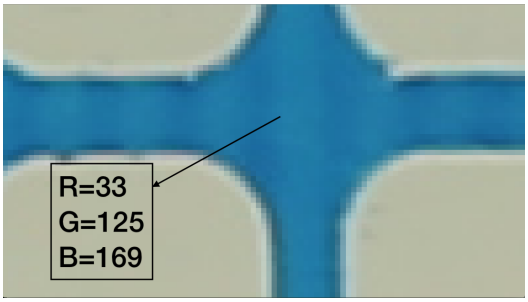

(c) 75% Saturation

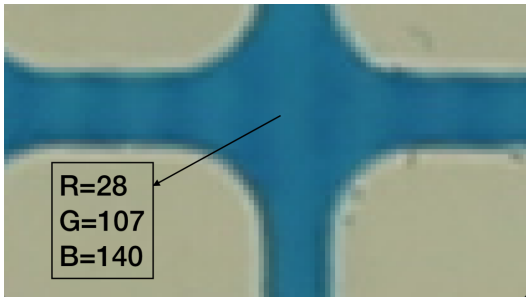

(d) 100% Saturation

Figure 3.23: Difference in color intensity of the same pore channel at different saturation

To reduce the uncertainty, it is assumed that the color conditions can be slightly different between different frames. Figure 3.27 and Table 3.9 show non-uniform color intensity in a same saturation for the the pore space of micromodel. This is due to different pore depth caused by the laser engraving and chemical etching step in micromodel fabrication. The developed image processor is programmed to extract a different correlation for different pixel points on the model. The program asks for all of the calibration images (Figure 3.23), then for a specific pixel point extracts the color intensity related to each concentration and determines the correlation between concentration and color intensity for that specific point. For example, we pick the chosen pixel in Figure 3.23. We follow the steps below to find the colour intensity correlation for that specific pixel:

1. Covert the RGB (Red, Green, Blue) value to intensity. To find the linear intensity from RGB, we first divide RGB value by 255, and compute the equation below:

$$Linear\ Intensity = 0.2126 \times R + 0.7152 \times G + 0.0722 \times B \tag{3.110}$$

2. Compute non-linear gamma correction [4] of the colour intensity.

3. Find the correlation of concentration versus intensity. For example for this specific pixel:

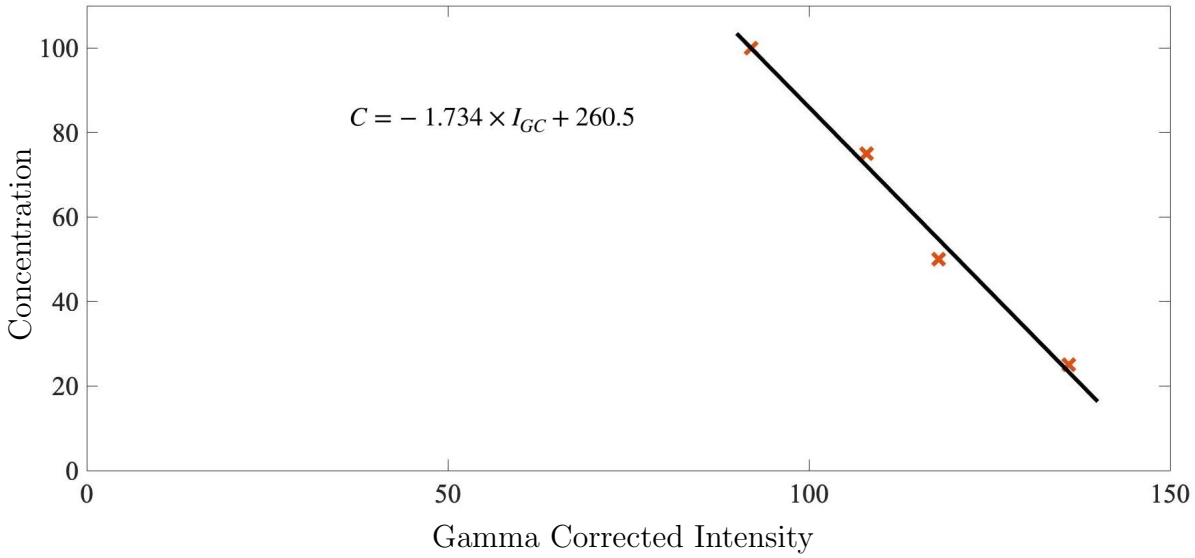

Figure 3.24: Correlation of concentration and colour intensity for the specific pixel. C in concentration and I_{GC} is Gamma corrected colour intensity

The program repeats this for all of the pixel points in the pore space section of the micromodel image. This means that for an image with thousands of pixels, we would have thousands of correlations. Figures 3.25 and 3.26 show the selected pore space before and after calibration.

[4]Gamma encoding of the image is used to optimize the usage of bits when encoding an image

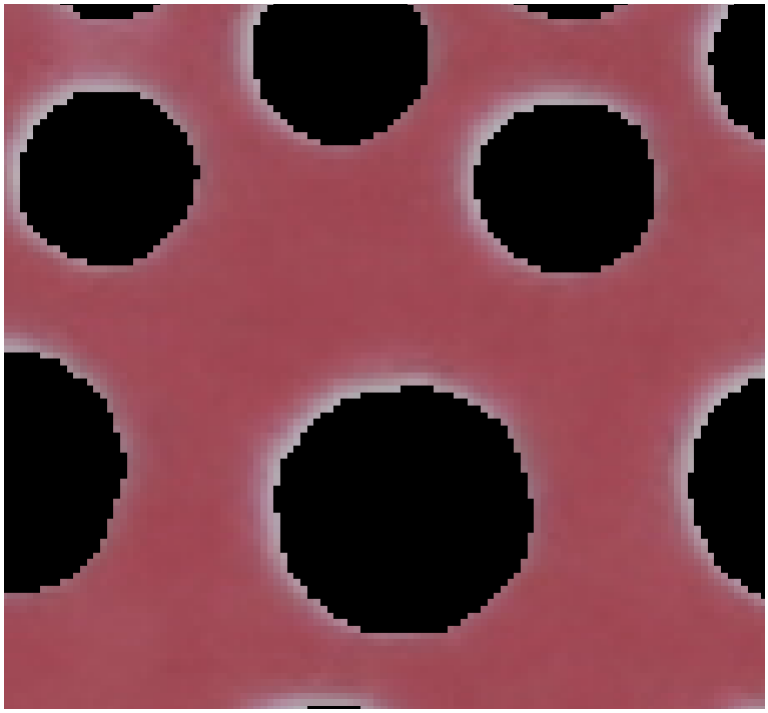

Figure 3.25: Selected pore space before colour intensity calibration

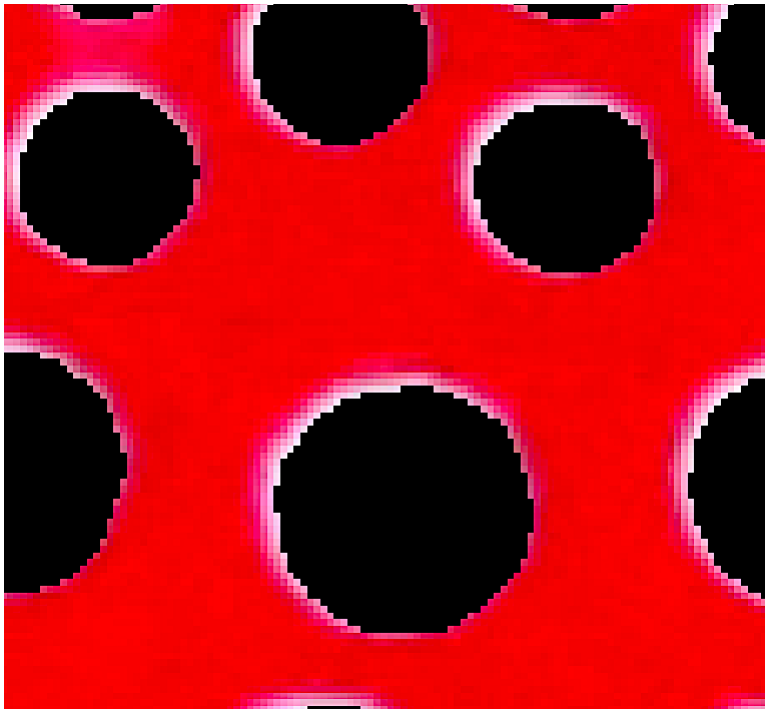

Figure 3.26: Selected pore space after colour intensity calibration

The overall saturation range from 0 to 1 is divided in several grades and number of

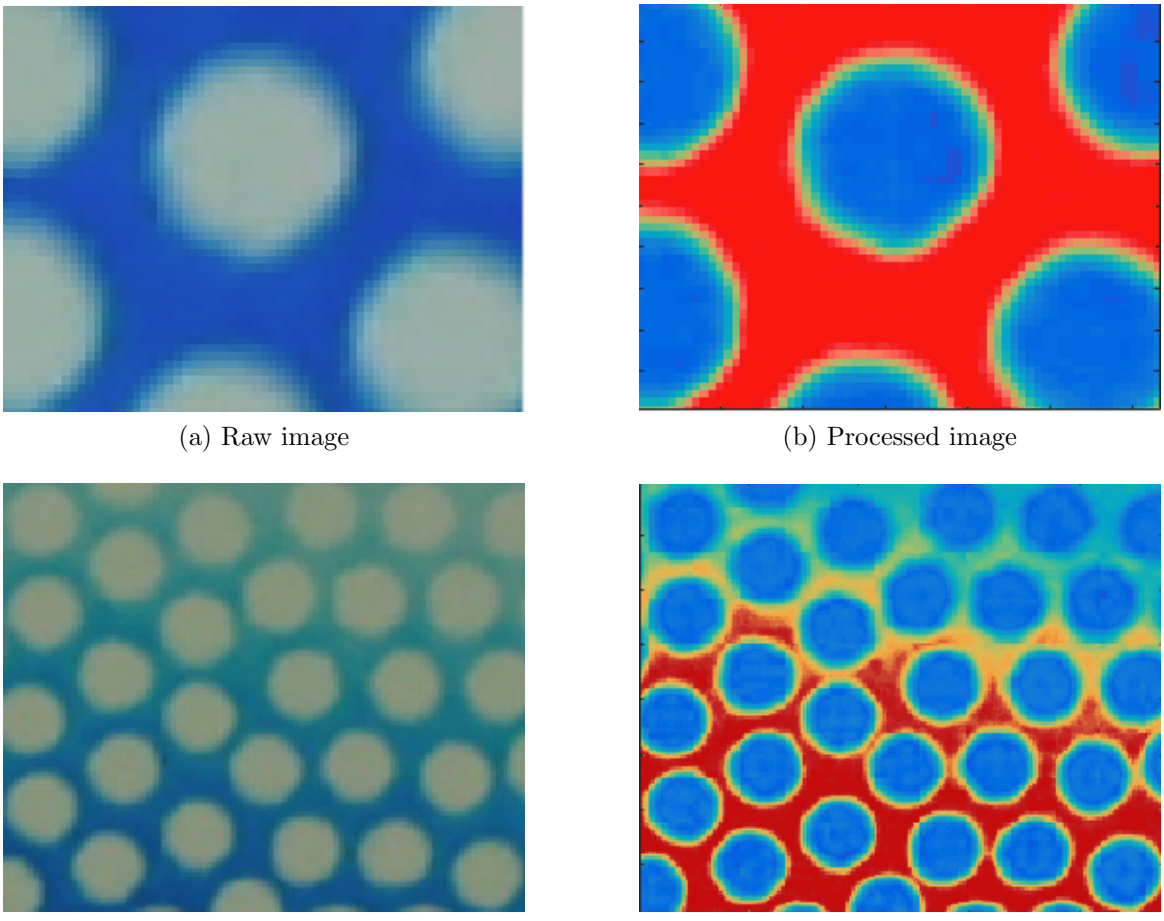

(a) Raw image

(b) Processed image

(c) Raw image

(d) Processed image

Figure 3.27: Pixel by pixel processing of the fully saturated pores (a, b) and mixing zone during miscible displacement (c, d)- Images (a,c) are raw and (b,d) are processed

pixels in each grade is computed. The final prepared map is used to be fitted with the introduced analytical solution in Equation 3.98 to estimate the dispersion coefficients. In order to avoid pattern misclassifications white balancing algorithm is applied. The adaptation of the Grey world white balancing algorithm is used. In this approach it is expected that the average color of the image should be gray and the deviation from this is assumed to be caused by the illuminant color. The updated algorithm

differs from the original one by only considering candidate grey pixels except all the pixels of the image. In the developed image processing tools, the grid pattern color estimation is based on the analysis of the peaks of the histogram of pixel saturation and hue in Hue- Saturation- Value (HSV) format. Initially the algorithm finds first peak of the saturation and uses it as the limit for selection of the grid. All the pixels below this level are assumed to be white and not relevant to the grid. Next, verification is done based on the brightness of the pixels. Pixels which have very low brightness are considered to be black, pixels with high brightness are considered to be white. Parameters "blackCutoff" and "whiteCutoff" define threshold limits. When the uncolored pixels are excluded from the analysis histogram of the pixels hue is analyzed in order to estimate number of different peaks which should be related to different colors of the image. The number of maximum expected colors is set up with parameter "colorNum". Finally the color covering the largest area is selected as grid color. Finally when the image and the mask are aligned it is possible to compute areas covered by different fluids. It is assumed that areas which have more fluids have less intensive color and though smaller saturation. The overall saturation range from 0 to 1 is divided in several grades and number of pixels in each grade is computed.

3.15.2 Matching the Calibrated Concentration Map with the Analytical Solution of ADE

After obtaining the concentration indirectly for all of the pixel points (Figure 3.30), we can analyze the miscible displacement images in time. Different tests were conducted with different injection flow rates to determine the effect of the fluid velocity on longitudinal and transverse dispersion. The time intervals and exact time of each image were recorded. With this information, the concentration map for each time step was extracted from the processed images as Figure 3.32 shows an example. The

program reads the image point by point and uses the specific correlation (extracted from the calibration step) for each point to calculate the concentration from the R (Red), G (Green), and B (Blue) values for each pixel.

3.15.3 Calculation of Dispersion Coefficients

The development of a process model typically goes through several steps. These steps include model formulation, a collection of data from designed experiments, model testing and discrimination, and extensions of the database with sequential experiments. The statistical investigation of the ADE model begins with the estimation of its parameters from experimental observations (longitudinal and transverse dispersion coefficients). To achieve this goal, experimental observations with independent Normal error distributions and given relative variances, Baye's theorem leads to the method of least squares. Least squares were introduced by Legendre [3] in 1805 as a curve-fitting method, and by Gauss [3] in 1809 as a Bayesian procedure for estimating parameters from data with independent Normal distributions of error. An engaging account of these developments and related events is given by Stigler [85] (1986). Gauss included models non-linear in the parameters and weighted the observations according to their precision. He gave an efficient solution scheme for the normal equations of the least-squares problem and showed how to calculate the variances of the resulting parameter estimates. Later work has been largely built on this foundation, refining the posterior density function and adding interval estimates, hypothesis tests, model discrimination methods, and efficient procedures for the design of experiments. In this study the *Athena Visual Studio* solver is used for estimation of parameters (longitudinal and transverse dispersion coefficients).

To do this, the developed program reforms the image using the extracted data. The apparent longitudinal and transverse dispersion coefficients are estimated by fitting

experimental concentration map obtained from the image processing to the analytical solution with the use of the Bayesian estimator. In this code, the objective function, a weighted sum of squares of deviations of model predictions from observations, is expanded as a quadratic function of the parameters, around the initial values of the current iteration. The resulting parameter minimization problem is solved with quadratic programming by using a modified Gauss-Jordan algorithm [1]. Interval estimates of the parameters are computed by using a posterior density function constructed from the final quadratic expansion of the objective function, this is done automatically in the subroutine package *GREGPLUS* of the software *Athena Visual Studio*. Figure 3.28 shows the segmentation of written source code in *Athena Visual Studio*.

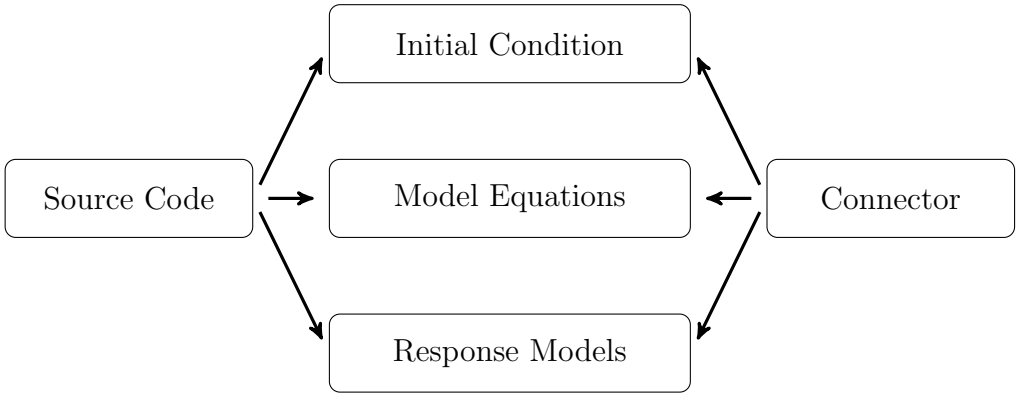

Figure 3.28: Source code segmentation for estimation of dispersion coefficients

Figures 3.29, 3.30, 3.31 and 3.32 show the followed steps as an example of analyzing procedure for a miscible displacement in a micromodel experiment from cropping to processing.

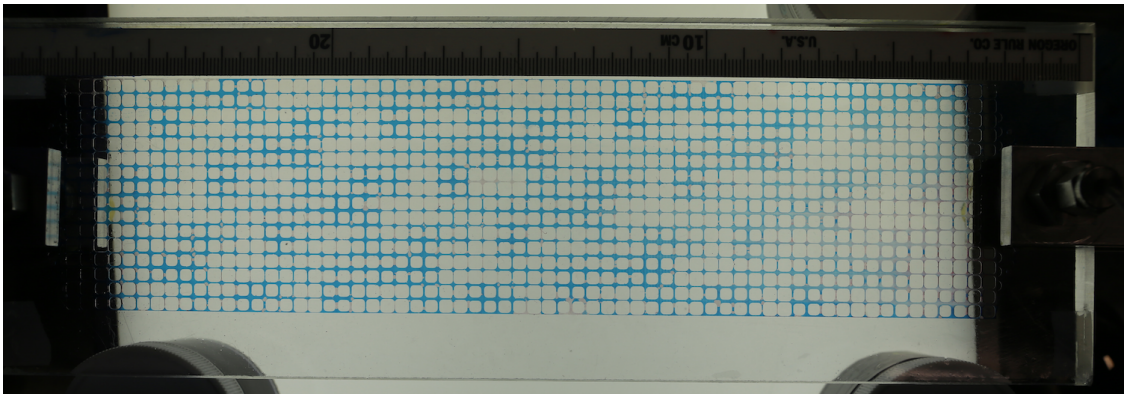

Figure 3.29: Sample raw image taken during the experiment

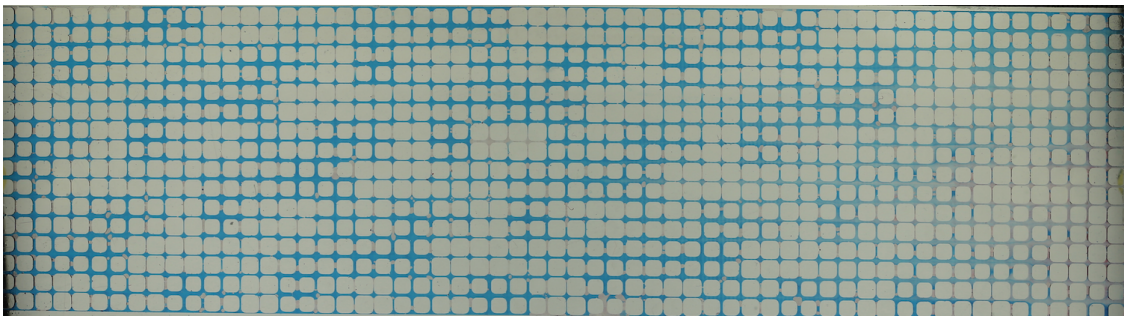

Figure 3.30: Cropped and calibrated images

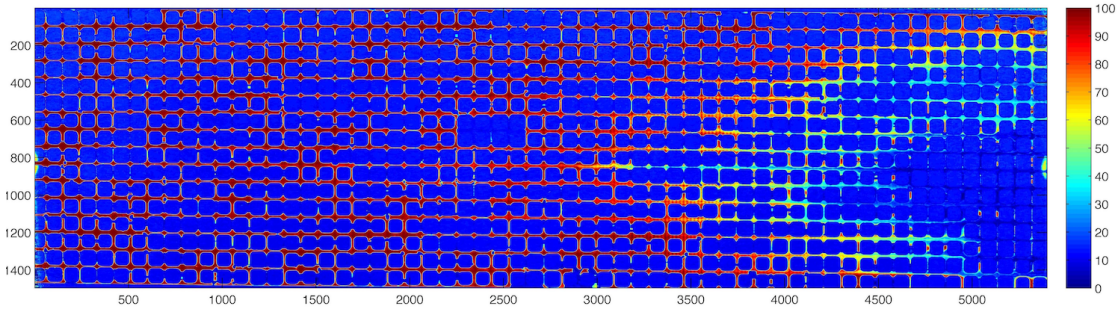

Figure 3.31: Processed image

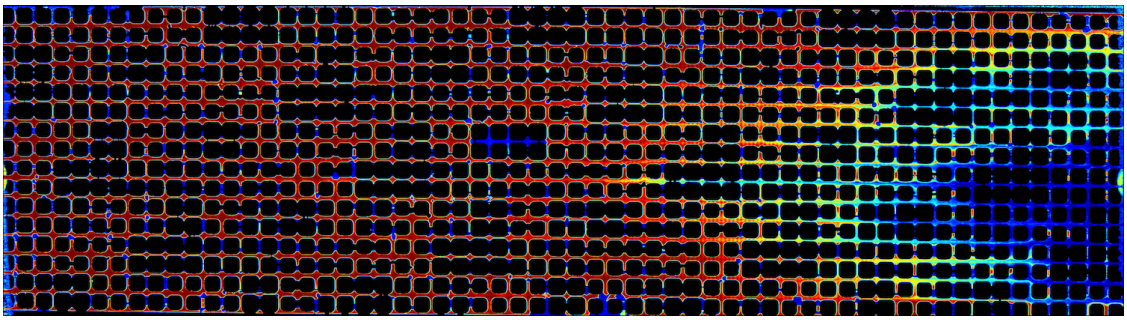

Figure 3.32: Analyzed masked image and concentration map

3.16 Design of Experiments (DOE)

Design of Experiment (DOE) in academic and industrial research is a systematic method to design, perform, and analyze an experimental process and determine the relationship between input factors of a process and the output of that process that has been measured or calculated. Input variables are categorized into two types:

1. Controllable variables that can be varied easily during experiments and such variables have a key role to play in process characterization.

2. Uncontrollable variables are difficult to control during experiments and defined under errors caused by random uncertainties.

Figure 3.33 shows the output as a response characteristic of input. Responses, or output measures, are the elements of the process outcome that the experiment is studying. To gain the maximum advantage from a series of experiments, they must

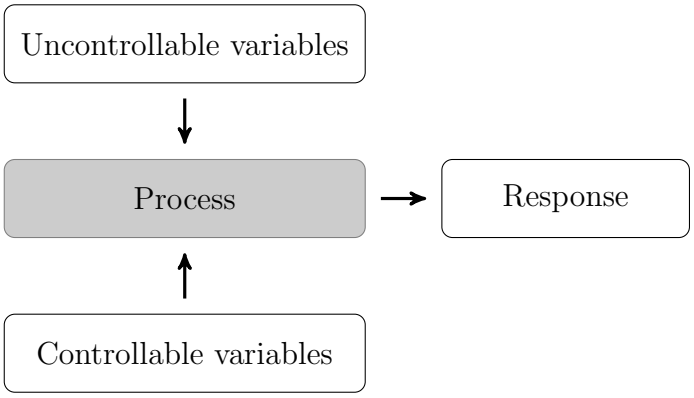

Figure 3.33: Experimental process input factors and output responses

be properly designed. Starting with a series of organized trails and screening tests to obtain the experimental information DOE is implemented. Before we start the design of the experiment, the input and output variables need to be characterized. This experimental study is looking at the effect of pore geometry and fluid velocity

on dispersion (longitudinal and transverse) during miscible displacement. The inputs and responses in this study are shown in Table 3.10. The difference between the two types of variables is that the experimental variable is one that we have control over and should be randomized to reduce the human error [28]. The responding variable is the variable that we will be observing to see if there is any effect on it.

Table 3.10: List of input factors and output responses in experimental study

Parameter	**Symbol**	**Type**	**Subject to study**
Mean pore throat diameter	$\langle R \rangle$	Input	Yes
Mean pore throat length	$\langle l \rangle$	Input	Yes
Variance of pore throat diameter	$\langle R^2 \rangle$	Input	Yes
Variance of pore throat length	$\langle l^2 \rangle$	Input	Yes
Kurtosis of pore throat diameter	$\langle R^4 \rangle$	Input	Yes
Pore volume of micromodel	PV	Input	No
Porosity	ϕ	Input	No
Fluid viscosity	μ	Input	No
Fluid density	ρ	Input	No
Pressure	P	Input	No
Temperature	T	Input	No
Molecular diffusion	D_m	Input	No
Flow velocity	v	Input	Yes
Peclet number	Pe	Input	Yes
Time	t	Response	Yes
Permeability	K	Response	Yes
Concentration	C	Response	Yes
Longitudinal dispersion	D_L	Response	Yes
Transverse dispersion	D_T	Response	Yes

In this study for single permeability experiments we choose single factor (velocity) multilevel design (Table 3.11). This design is more efficient to detect the possible non-linear effects of velocity on dispersion. For the dual permeability pattern we use optimal design for two factors including velocity with 5 levels and permeability with 2 levels (Table 3.12). The input factor permeability in dual permeability porous media represents different pore geometry such as pore size distribution in one single factor.

Table 3.11: Design of miscible displacement experiments in single permeability porous media

Factor	**Level**
Velocity	5 (0.002, 0.004, 0.006, 0.008, 0.010 cc/min)

Table 3.12: Design of miscible displacement experiments in dual permeability porous media

Factor	**Level**
Velocity	5 (0.002, 0.004, 0.006, 0.008, 0.010 cc/min)
Permeability	2 (Low, High)

3.16.1 Response analysis

In this study, we use the Design Expert to analyze the responses (output) measured or calculated from each experiment. For this purpose we use the tools below:

- Residuals: The unexplained remainder of the squared deviations from the mean is called residuals or random uncertainty.

- Box-Cox plot: The results need a transformation when the residual is a function of the response, otherwise, results are biased. Design-Expert provides diagnostic

capabilities to verify if the statistical assumptions are satisfied. The normal plot of the residuals examines their normality. The residuals versus predicted response value plot checks if a pattern exists. The Box-Cox plot provides a recommended transformation from the power family if it is needed.

3.17 Error and Uncertainty Analysis

Experimental investigations maintain operational errors and uncertainties. In this section, some sources of errors including experimental (systematic) and random have been highlighted which should be taken into account when considering the results.

3.17.1 Random Errors

Random errors are statistical fluctuations in the measured data due to the precision limitations of the measurement devices. Random errors usually result from the experimenter's inability to take the same measurement in exactly the same way to get exactly the same number. In this study, the most important sources of random errors are as discussed below.

- **Camera adjustment**: To avoid this error a wide-angle lens has been used that can be used as a starting point for optimization. The image processing tool has been designed to minimize the effect of camera angle and picture coverage to capture only the flow domain; however, sometimes there was a little bend in the tripod adjustment so the captured flow domain was not straight and cropping of the image was needed to include this dead area. This process created some error of calculations in image processing. Also error during mounting the glass model as it was based on local observation and not by some instrument. This caused a slight difference in the angle adjustment.

- **Breakthrough Estimations**: Misjudgment in estimating when the fluid arrived into the system, which affected the start and the ending time of the experiments. To avoid this error besides using a high-accuracy, low-rate pump, the fixed time intervals of images allows the image processing program to capture the accurate time of breakthrough and also the total time of displacement.

- **Experimental Environment**: The experiments were replicated as best as possible in terms of the colour intensity of the room light, however, the ideal condition might not happen. Although the image processing tool is designed to correct this error, the amount error might have varied from one experiment to another as they have been carried out in the different condition of the room light. This affected the image processing of the final image.

3.17.2 Systematic Errors

Systematic errors, by contrast, are replicable inaccuracies that are consistently in the same direction. Systematic errors are often due to a problem which persists throughout the entire experiment.

- Syringe pump precision to operate low flow rates. The pumps accuracy was (0.1 cc/hr)

- Leaks caused bubbles and reduced flow rates.

- Some areas were not invaded by either the injected or in-place solvent as air blocked those channels.

- Error due to image processing as the final image might not have been 100% saturated, but it was considered as it is fully invaded by the injection fluid. To

avoid this error, a color calibration tools have been built in the image processing program.

- Images were cropped to select only the flow domain of the micromodel. However, sometimes the frame was not straight which resulted in bad cropping. Thus, an image processing, the small area was also considered. To minimize this error, a javascript plugin has been developed for Photoshop to crop all of the images of the same experiment in a consistent manner.

- For the small concentration values in the porous domain when mixing occurred at the microscopic level, the lower values of reddish tint were ignored.

Chapter 4

Results and Discussions

4.1 Mathematical Results

A conceptual model of dispersion using random walk theory and the probabilistic properties of particle movement in porous media has been introduced. The model is assumed valid when molecular diffusion is negligible ($10 \leq Pe \leq 10^6$). The dominant mechanical dispersion is decoupled into transverse and longitudinal dispersion. The established model predicts dispersion using pore geometry parameters including degree of heterogeneity or normalized variance of pore throat length and normalized kurtosis of pore throat diameter. Experimental relationships for both longitudinal and transverse dispersion, under similar conditions show that they are proportionally dependent to velocity which concurs with the theoretical model. A dimensional ratio of $\frac{\langle l^2 \rangle}{\langle l \rangle}$ also proves the scale dependency of dispersion, which is in agreement with observational studies [13]. Obtained models for dispersion are shown in Equation 4.1:

$$D_T = \frac{3\pi}{64} \frac{\langle l^2 \rangle}{\langle l \rangle} \frac{\langle R^4 \rangle}{\langle R^2 \rangle^2} \langle v_x \rangle \quad \text{and} \quad D_L = \frac{9\pi}{64} \frac{\langle l^2 \rangle}{\langle l \rangle} \frac{\langle R^4 \rangle}{\langle R^2 \rangle^2} \langle v_x \rangle + \frac{\pi}{12} \frac{\langle l^2 \rangle}{\langle l \rangle} \langle v_x \rangle \tag{4.1}$$

In the following section, the proposed models are discussed in detail.

4.1.1 Ratio of Longitudinal and Transverse Dispersion

As shown in Equation 4.2, using the statistical relationships for dispersion coefficients, the ratio of longitudinal to transverse dispersion, is always higher than three.

$$\frac{D_L}{D_T} = \frac{\frac{9\pi}{64}\frac{\langle l^2\rangle}{\langle l\rangle}\frac{\langle R^4\rangle}{\langle R^2\rangle^2}\langle v_x\rangle + \frac{\pi}{12}\frac{\langle l^2\rangle}{\langle l\rangle}\langle v_x\rangle}{\frac{3\pi}{64}\frac{\langle l^2\rangle}{\langle l\rangle}\frac{\langle R^4\rangle}{\langle R^2\rangle^2}\langle v_x\rangle} = 3 + \frac{\pi}{12}\frac{\langle R^2\rangle^2}{\langle R^4\rangle} \tag{4.2}$$

Results show that increasing the $\frac{\langle R^2\rangle^2}{\langle R^4\rangle}$ increases the ratio of longitudinal and transverse dispersion coefficients. Also, the Equation 4.2 shows that the ratio of D_L to D_T depends on pore throat diameter and independent from the distribution of pore throat length. The ratio of $\frac{\langle R^2\rangle^2}{\langle R^4\rangle}$ is the inverse of the normalized forth moment of the Probability Distribution Function (PDF) and is a measure of the distribution flatness. Heavier tailed distributions have a smaller $\frac{\langle R^2\rangle^2}{\langle R^4\rangle}$. Hence, for a uniform, unconsolidated, isotropic porous media, $\frac{\langle R^2\rangle^2}{\langle R^4\rangle} << 1$ is very small and therefore a value of $\frac{D_L}{D_T}$ approaches 3. For consolidated media, the pore throat diameter distribution is skewed meaning a higher $\frac{\langle R^2\rangle^2}{\langle R^4\rangle}$ leading to higher values of $\frac{D_L}{D_T}$. It is also shown in Equation 4.2 that the ratio of longitudinal to transverse dispersion is independent of velocity, as the velocity term in Equation 3.54 was neglected and v_x cancels out in Equation 4.2. The result is that the dependency of $\frac{D_L}{D_T}$ on v_x is considered very weak or negligible for the assumed range of Peclet number ($10 \leq Pe \leq 10^{12}$)[1].

4.1.2 Effect of Heterogeneity

The common term in both the longitudinal and transverse dispersion coefficients is normalized variance of pore throat length (l). As Equation 4.1 illustrates increasing the term of $\frac{\langle l^2\rangle}{\langle l\rangle}$ increases both the longitudinal and transverse dispersion coefficients. The ratio $\frac{\langle l^2\rangle}{\langle l\rangle}$ describes the degree of heterogeneity of the porous media denoted by

[1]Within the range of valid Darcy fluid behaviour and negligible molecular diffusion

D_{Het}. This ratio shows the extent of variability in relation to the mean of the pore throat length. As a result, higher value of $\frac{\langle l^2 \rangle}{\langle l \rangle}$ means broader length distribution and higher degree of heterogeneity which leads to higher variability in flow velocity and the rate of spreading. It should be noted that longitudinal dispersion, due to a stronger dependency, is more sensitive to the degree of heterogeneity. The dimension of $[L]$ or length of this ratio also shows scale dependency of dispersion.

4.1.3 Effect of Pore Size Distribution

The second mutual term in equations of D_L and D_T (Equation 4.1) is $\frac{\langle R^2 \rangle^2}{\langle R^4 \rangle}$, which describes the distribution of pore throat diameter $f(R)$. The pore throat diameter distribution affects dispersion coefficients similarly to permeability. The interpretation of this effect is complex. However, it is valid to say that smaller pores and pore throats have shorter residence time and most particles may move quickly through the larger pores with maximum opportunity for longitudinal and transverse dispersion. Hence, both components of dispersion increase proportionally by increasing the $\frac{\langle R^2 \rangle^2}{\langle R^4 \rangle}$, while the ratio of longitudinal to transverse ($\frac{D_L}{D_T}$) decreases.

4.1.4 Effect of Pore Geometry

Four different porous media with the same average grain size and porosity are assumed. Statistical heterogeneity of the system increases by increasing the variance of pore throat length. Hence, the medium with the largest value of variance is the most heterogeneous medium. The statistical properties of the assumed porous media are shown in Table 4.1. Since in the experimental section of this study a pixel-based method has been used to develop an unstructured pore network model to conduct micromodel experiments, higher porosity media have been considered here. Besides

the petroleum industry, higher porosity media are found in many industrial applications such as metallic thin-fiber material and metallic powder, which are used in the transportation industry. Longitudinal dispersion over molecular diffusion (assumed

Table 4.1: Statistical properties of the assumed porous media to investigate the effect of pore geometry on calculated longitudinal and transverse dispersion

Porous Media	ϕ %	$\langle R \rangle$ (μm)	$\langle l \rangle$ (μm)	$\langle R^2 \rangle$ (μm^2)	$\frac{\langle R^4 \rangle}{\langle R^2 \rangle^2}$ [1]	$\langle l^2 \rangle$ (μm^2)	$\frac{\langle l^2 \rangle}{\langle l \rangle}$ (μm)
1	48	324	640	0.1885	1.8369	0.6448	0.0010
2	44	286	631	0.1082	1.3087	0.6503	0.0011
3	38	238	580	0.0637	1.3854	0.3997	0.0007
4	34	234	495	0.0627	1.4296	0.2701	0.0005

$10^{-9} m^2 s^{-1}$) versus increasing velocity is illustrated in Fig 4.1. As shown in Figure 4.1

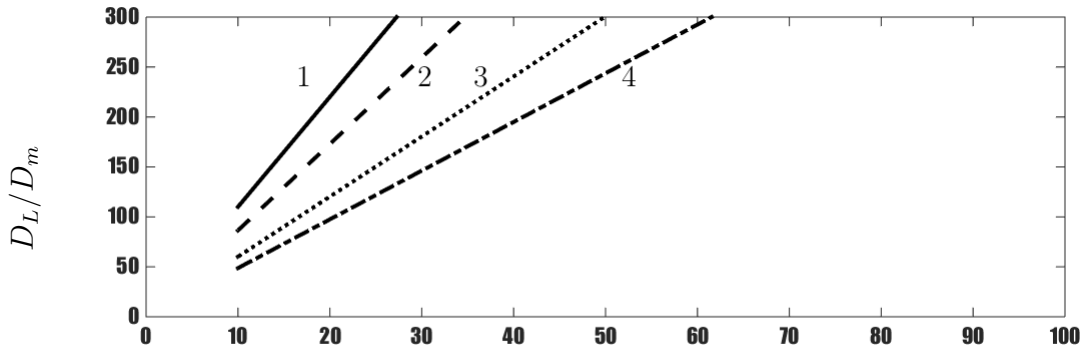

Figure 4.1: Relative longitudinal dispersion over molecular diffusion vs fluid velocity for different pore geometries (fluid velocity in $\times 10^{-6}[ms^{-1}]$).

dependency of the dispersion coefficient on velocity increases as the heterogeneity of the medium increases. The Peclet number is directly proportional to fluid velocity, so the same behaviour is expected for dispersion versus Peclet number. Fig 4.2 also shows the variation of transverse dispersion. According to Fig 4.1 and 4.2, the effect of heterogeneity on the longitudinal and transverse dispersion coefficients decrease with

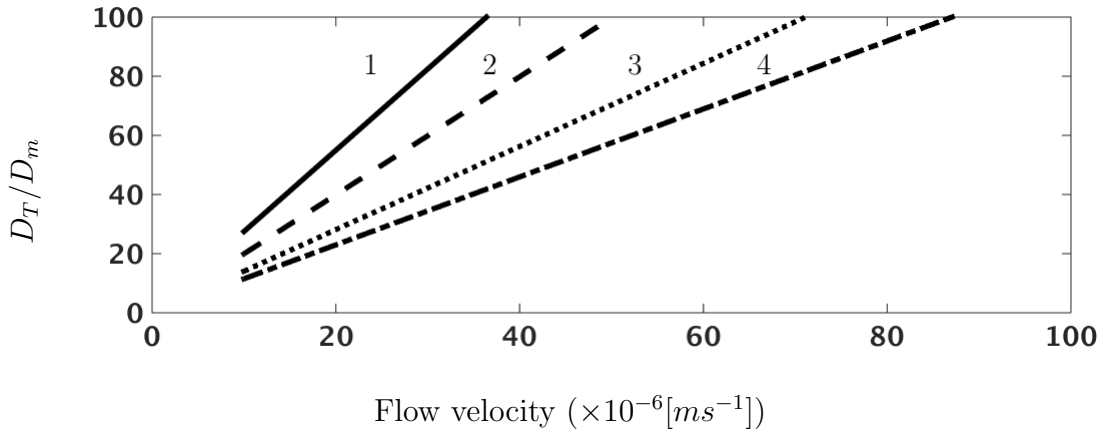

Figure 4.2: Relative transverse dispersion over molecular diffusion vs fluid velocity for different pore geometries (fluid velocity in $\times 10^{6}[ms^{-1}]$).

decreasing fluid velocity. This means that for a high fluid velocity (Peclet number), heterogeneity has a greater effect on increasing the dispersion coefficient. This effect could be concluded from reducing the importance of advective spreading on the mixing process by decreasing the fluid velocity. In Fig 4.3, longitudinal and transverse dispersion for porous medium 1 is shown. As shown in the Table 4.1 porous medium has higher variance of pore diameter ($\langle R^2 \rangle$) which implies higher level of heterogeneity. As illustrated, longitudinal dispersion is higher than transverse dispersion and this difference increases as velocity (Peclet number) increases.

4.1.5 Visual Simulation of Assumed Porous Media

In this section, we implement the estimated dispersion coefficients from the statistical model into the numerical simulation introduced in Section 3.9 to observe the ability of the developed model in simulating the behavior of the miscible displacement and capturing the special phenomena during the process. We assume the four pore geometries introduced in Table 4.1 to simulate the apparent mixing as a result of advective spreading in longitudinal and transverse directions.

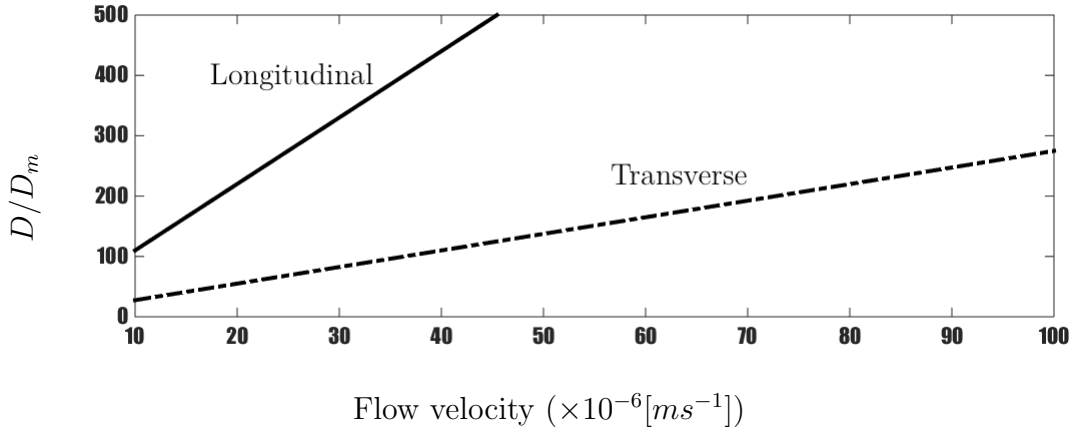

Figure 4.3: Relative longitudinal and transverse dispersion over molecular diffusion vs fluid velocity for certain pore geometries (fluid velocity in $\times 10^{6}[ms^{-1}]$).

The relative importance of these two dispersion sources at a different injection velocities of the different pore geometry is shown in Figure 4.4. The injection velocity is the same for all four media, but the longitudinal and transverse dispersion coefficients are different due to a difference in pore properties (as per Table 4.1). Figures 4.4, 4.5, and 4.6 show the results of the miscible displacement of continuous injection of displacing fluid in four anisotropic porous medium. The color spectrum is representative of concentration. Continuity of the color spectrum in the mixing zone could be used as a characteristic for effective mixing. In order to determine the concentration profile of displacing fluid in a miscible displacement for each porous media, the calculated concentrations of all of the pixel points from the found correlations (explained in Section 3.15.2) over the desired cross section are averaged at the chosen time. Figures 4.4 and 4.5 show the results of the calculated concentration of each porous media at the chosen time step in parallel and normal directions to injection. The effect of higher dispersion coefficient is visible in concentration profiles, for instance, higher transverse dispersion coefficient in porous medium 1 leads to more compact concentration lines in Figure 4.5c compared to porous medium 4 in Figure 4.4a. Simultaneously, the

same effect happened on concentration profiles in x-direction (Figures 4.5d and 4.4b) which implies the faster development of the displacement process.

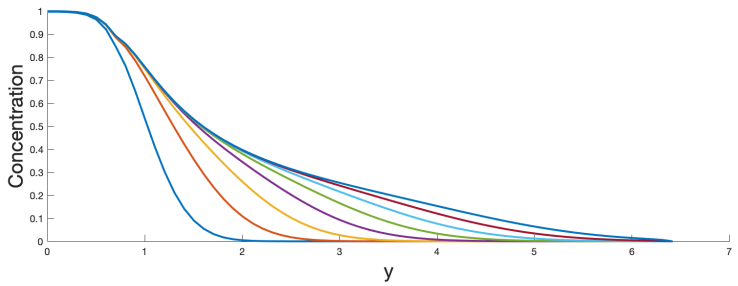

(a) Concentration versus y direction for porous medium 4

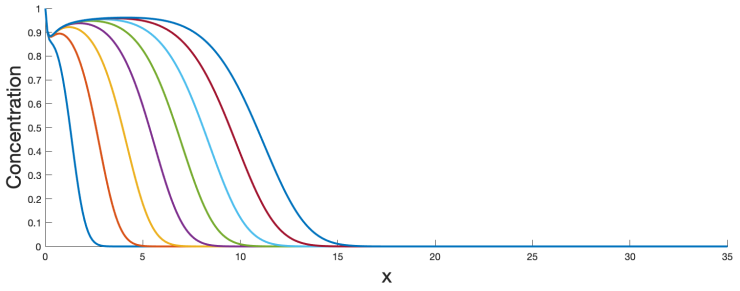

(b) Concentration versus x direction for porous medium 4

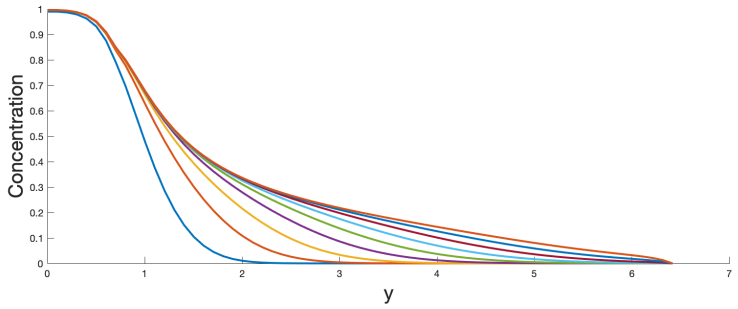

(c) Concentration versus y direction for porous medium 3

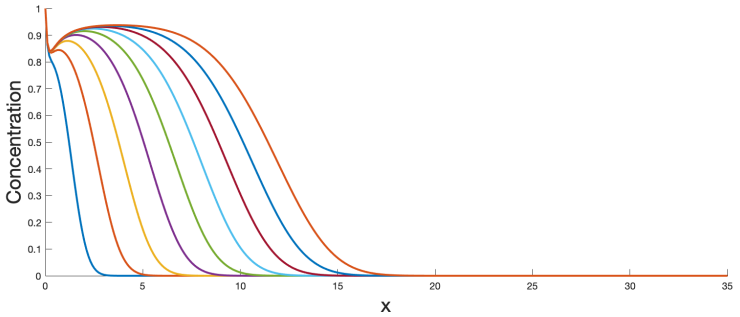

(d) Concentration versus x direction for porous medium 3

Figure 4.4: Concentration profile versus x and y-directions for assumed porous media 3 and 4 in Table 4.1 in different time steps ($\Delta t = 10 minute$)

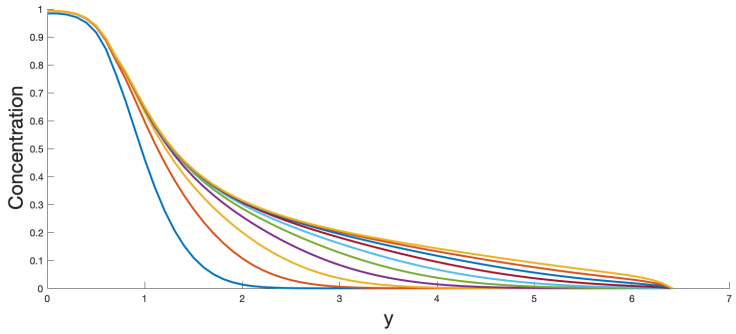

(a) Concentration versus y direction for porous medium 2

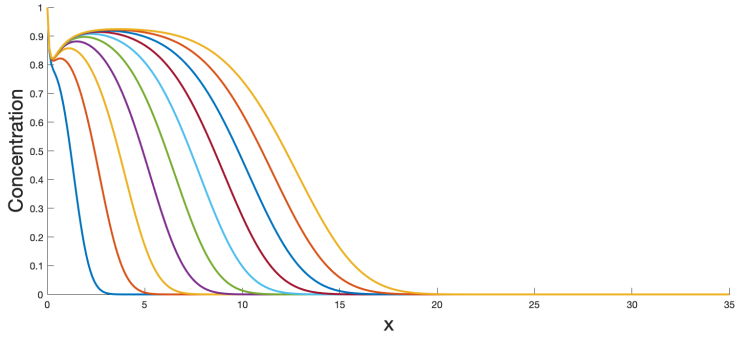

(b) Concentration versus x direction for porous medium 2

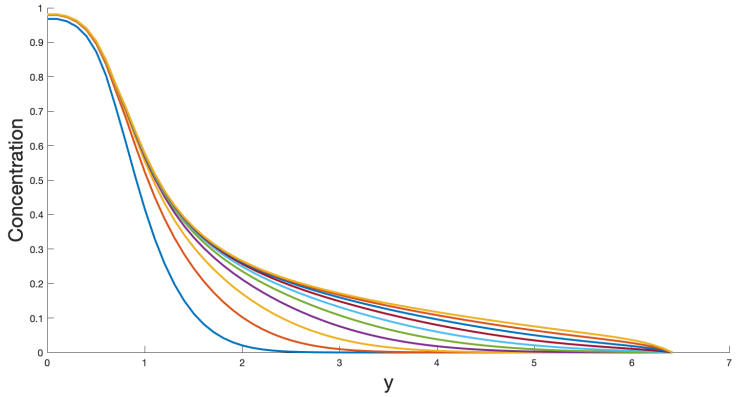

(c) Concentration versus y direction for porous medium 1

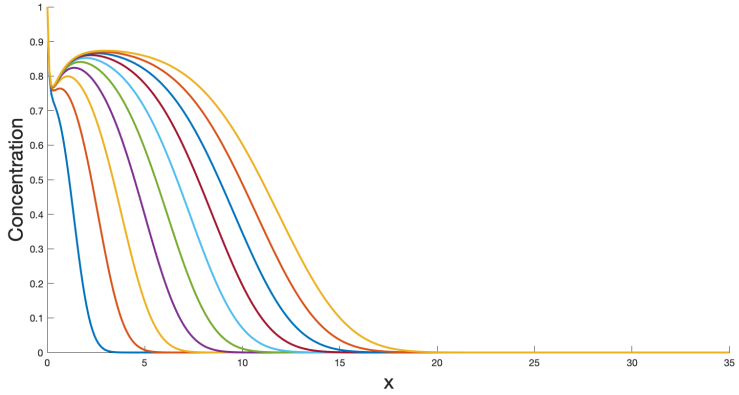

(d) Concentration versus x direction for porous medium 1

Figure 4.5: Concentration profile versus x and y-directions for assumed porous media 1 and 2 in Table 4.1 in different time steps ($\Delta t = 10 minute$)

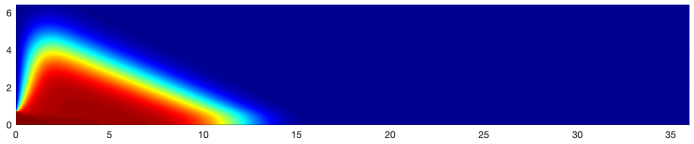

(a) Concentration map in porous medium 4

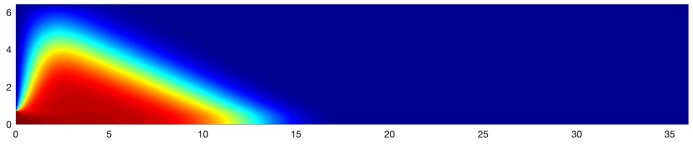

(b) Concentration map in porous medium 3

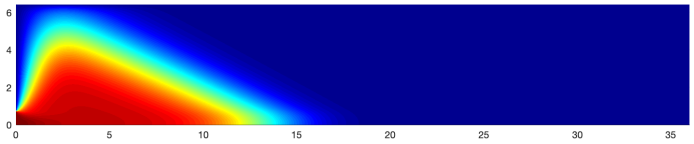

(c) Concentration map in porous medium 2

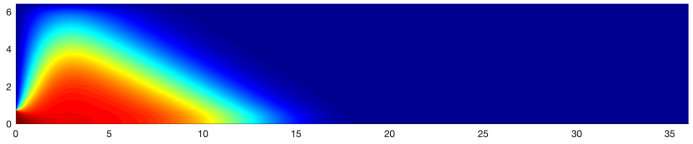

(d) Concentration map in porous medium 1

Figure 4.6: Snapshots of continuous displacing fluid injection in 4 assumed pore geometries in Table 4.1. Injection velocity for all four media are same as 0.01 cc/min and captured time-step is same as 120 min after the first drop enters the media. The $x-$ axis is the length and $y-$ axis is the width of the porous medium

Figure 4.6 displays the examples of the concentration maps for each media under the same conditions. As figures show higher dispersion coefficient in either direction of parallel or normal causes a thinker mixing zone for different pore geometries. By comparing Figures 4.6d, 4.6c, 4.6b, and 4.6a one observes that, for all porous media, the displacement front is broader in the direction parallel to the average flow (longitudinal dispersion), compared to the normal direction (transverse dispersion). While their amplitude is very different in 4 examples, indentations of the front appear at the same places, implying that they are closely related to the injection velocity which is the same for all 4 examples. In particular, a larger mixing zone is observed for media with higher heterogeneity observed in Table 4.1.

4.2 Experimental Results

In this study an experimental approach to estimate the average longitudinal and transverse dispersion coefficients in a single and dual permeability homogeneous anisotropic porous medium have been used. While the most previous studies of miscible injection have focused on using mathematical correlations to estimate the dispersion coefficients,this study utilizes a unique method to estimate the mass transfer properties. To study the dispersion in a single and dual-permeability porous media using experimental and numerical investigations the following results have been accomplished.

4.2.1 Experiment With Single Permeability Model

To gain the aimed objectives in this study a series of different injection rates and consequently different fluid velocities has been conducted. The difference between the injection rates lead to different mixing regimes during the miscible displacement and dispersion coefficients in both longitudinal and transverse directions. Using the

developed image processing tools, the processed images are obtained and longitudinal and transverse dispersion coefficients are approximated. Figure 4.7 shows the A series (cropped images) and B series (processed images) of miscible displacement experiments with the injection rate of 0.002 cc/min. The breakthrough times are reported and shown in Figure 4.11b for each experiment in the following too. This time is used in processing tool to estimate the dispersion coefficients. Visual comparison of the raw and processed images are demonstrated in Figures 4.7 and 4.8. The injection rate, interstitial velocity, longitudinal and transverse dispersion coefficients are reported in Table 4.2. As expected, increasing the injection rate in a manner consistent with the increase in average velocity for each set of experiments. The dispersion coefficients also increased with increasing fluid velocity as expected as it's shown in Figures 4.11c and 4.11d. The Peclet number ($Pe = \frac{vR}{D_m}$ where v is average velocity, R is average pore diameter and D_m is molecular diffusion) is also included.

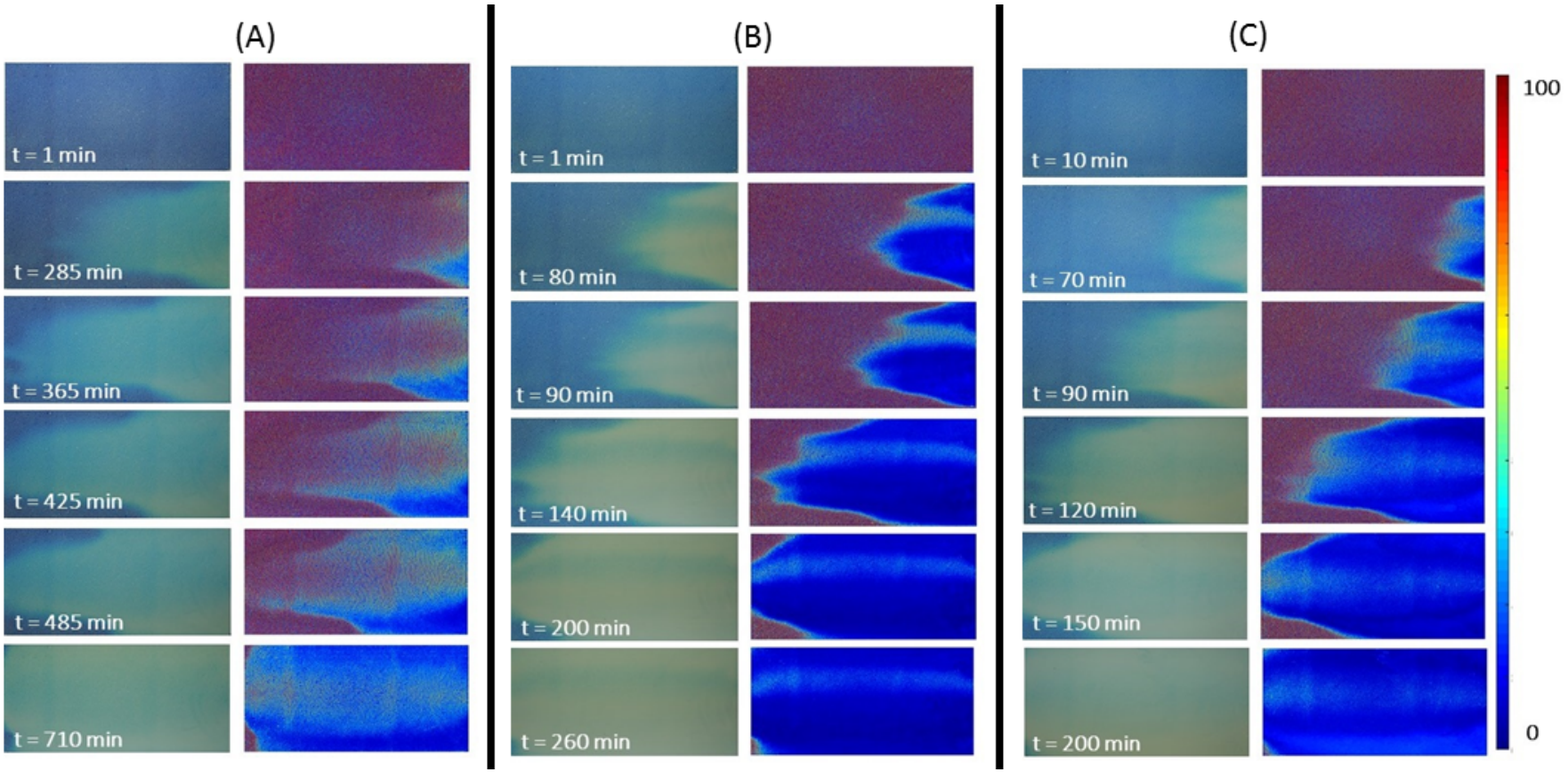

Figure 4.7: Images from the miscible displacement experiments. Scenario A is with injection rate of 0.002 cc/min, Scenario B is with injection rate of 0.004 cc/min and Scenario C is with injection rate of 0.006 cc/min. The left column of each scenario shows the actual experimental images while the right columns show the processed images (with injection from right to left of each image)

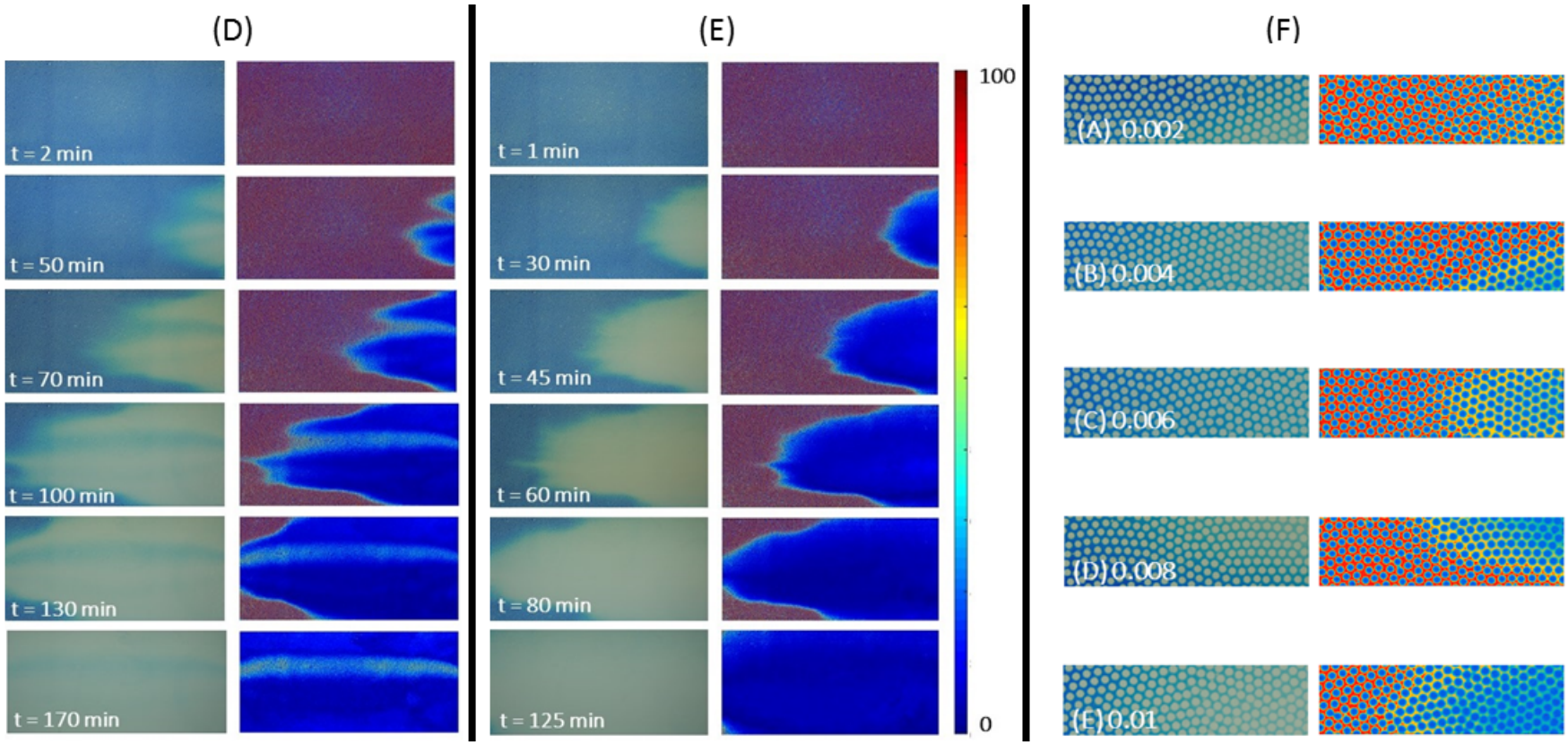

Figure 4.8: Images from the miscible displacement experiments. Scenario D is with injection rate of 0.008 cc/min, Scenario E is with injection rate of 0.01 cc/min. The left column of each scenario shows the actual experimental images while the right columns show the processed images (with injection from right to left of each image). Part F shows the comparison of mixing behaviours in mixing zones with different velocities.

For our experiments, the molecular diffusion coefficient is assumed $2.3 \times 10^{-9} m^2/s$ [75] for the experimental condition (atmospheric pressure and room temperature). The estimated average longitudinal dispersion coefficients for various injection rates and the corresponding average fluid velocity is illustrated in Table 4.2. The velocity for each experiment is calculated using the injection rate and cross sectional area as below:

$$v = \frac{q}{A} \tag{4.3}$$

where q is the injection rate in m^3/s and A is the cross sectional are of the injection port in m^2. The dispersion coefficient increases with increasing the injection rate. For the sake of simplicity, the average dispersion coefficients are estimated, however the Bayesian estimator is able to fit the matching dispersion coefficients for each pixel. The velocity distribution in the processed images in Figures 4.7 and 4.8 reflects the effect of pore size distribution of the micromodel versus fluid velocity too.

The distribution of the velocity shows more dispersion and scattering in both directions of the longitudinal and transverse (lateral) in higher velocities. The average longitudinal dispersion coefficient varies from 4.8×10^{-6} to 2.1×10^{-5} (Figure 4.11c) and respectively the transverse dispersion coefficient varies from 2.0×10^{-7} to 4.7×10^{-7} (Figure 4.11d). Transverse dispersion observation on the pore scale is significantly more challenging and fitting the analytical solution in Equation 3.98 is consequently more complicated. Dispersion in the lateral direction is caused by particle deviation from the flow path and cross from one flow path to another. The corresponding Peclet number in different scenarios varies from 3.95 to 4.65 as it is shown in Table 4.2. As shown in Figure 4.11a, the log of ratio of the longitudinal to transverse dispersion coefficient linearly increases with the log of the Peclet number. This observation is in a strong agreement with the expected behavior with the range of the displacement velocity in this experiment. The comparison of the different injection scenarios and

respectively, mixing behaviours are illustrated in Figure 4.8 part D that shows the different mixing regimes. The scattering of the fluid by increasing the velocity significantly develops in both longitudinal and lateral directions. At higher values of Pe, the distribution of the channel widths induces short range variations of the magnitude and the direction of the local velocity. One can then consider that displacing particles experience a random walk inside the pore volume with a velocity varying both in magnitude and direction relative to the mean flow velocity (v).

Figure 4.10 and 4.9 illustrate the Box-Cox plots for the calculated transverse and longitudinal dispersion coefficients in this experiment. The Box-Cox plot gives a fitting power-law transformation based on the best lambda value found at the minimum point of the curve of the natural log of the sum of squares of the residuals. If the 95% confidence interval around the λ includes 1, then there is no need for transformation, since the error (residuals) is not a function of the magnitude of the response. As Figure 4.10 and 4.9 show, there is no power transformation is required to interpret the results.

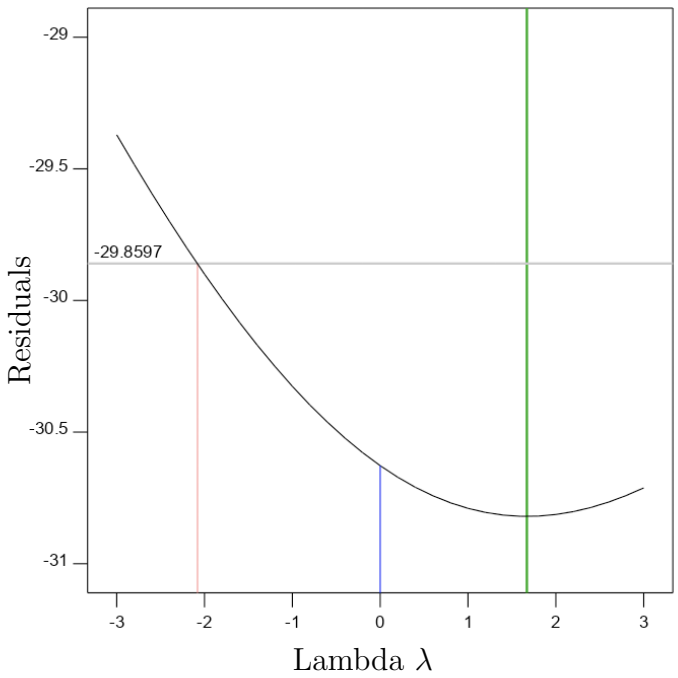

Figure 4.9: Box-Cox plot for power transformation of transverse dispersion coefficient. Current λ is 0 and best is 1.67, therefore no transformation is suggested

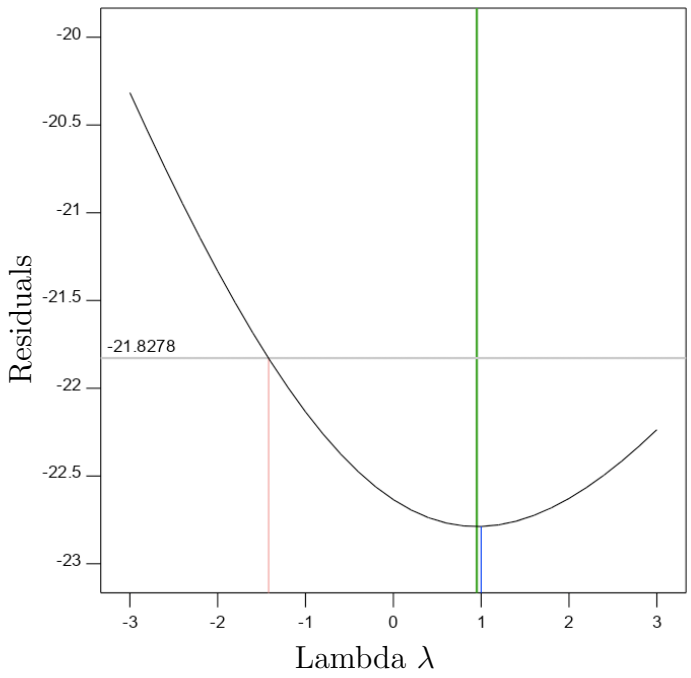

Figure 4.10: Box-Cox plot for power transformation of longitudinal dispersion coefficient. Current λ is 1 and best is 0.95, therefore no transformation is suggested

Table 4.2: Total time of the injection, longitudinal and transverse dispersion coefficients, and Peclet numbers for various injection rates, where q is injection rate, v is injection interstitial velocity, T_{tot} is total displacement time, D_L is average longitudinal dispersion, D_T is average transverse dispersion coefficient, and Pe is average Peclet number

Scenario	q (cc/min)	v (m/s)	T_{tot} (min)	D_L (m^2/s)	D_T (m^2/s)	$\log(D_L/D_T)$ [1]	$\log Pe$ [1]
A	0.002	6.0×10^{-5}	781	4.8×10^{-6}	2.0×10^{-7}	1.38	3.95
B	0.004	1.2×10^{-4}	387	8.9×10^{-6}	3.1×10^{-7}	1.48	4.26
C	0.006	1.8×10^{-4}	303	1.3×10^{-5}	3.7×10^{-7}	1.54	4.43
D	0.008	2.4×10^{-4}	238	1.6×10^{-5}	4.1×10^{-7}	1.59	4.56
E	0.010	3.0×10^{-4}	159	2.1×10^{-5}	4.7×10^{-7}	1.64	4.65

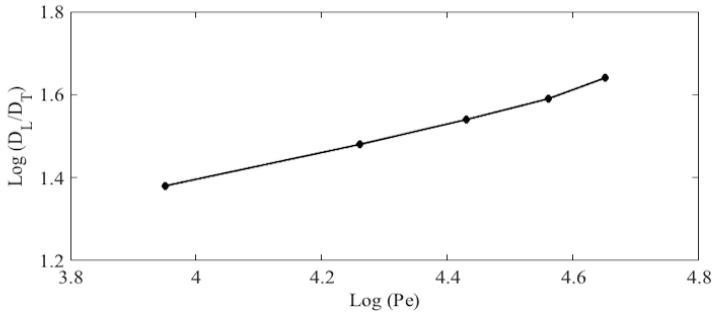

(a) Relative dispersion vs Peclet number

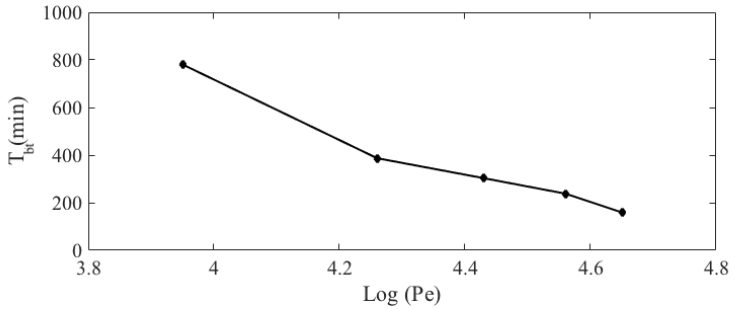

(b) Breakthrough time vs Peclet number

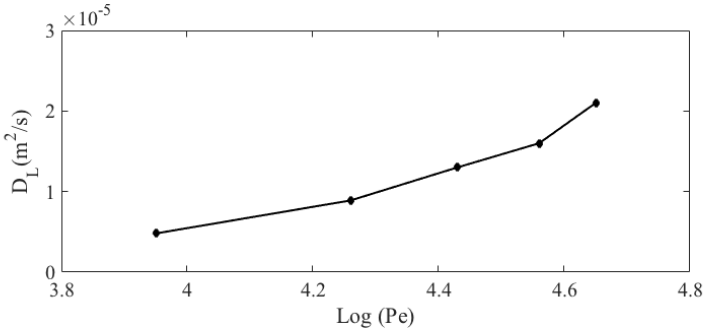

(c) Longitudinal dispersion vs Peclet number

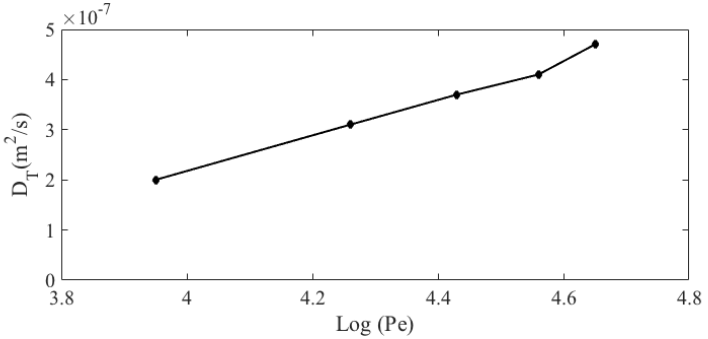

(d) Transverse dispersion vs Peclet number

Figure 4.11: Dispersion coefficients calculated from the homogeneous micromodel experiments as a function of the Peclet number

4.2.2 Experiment With Dual Permeability Model

During the experiments in the dual permeability micromodel, we observed a developing mixing zone over time. As Figure 4.19 shows, the mixing zone in the high permeability region is caused by longitudinal dispersion, and in lower permeability zone longitudinal and transverse dispersion are coupled. From the Taylor Equation 2.1, two factors are affecting on miscible displacement including advection and dispersion terms, especially in the case of lower injection rate. Comparison of the contribution of longitudinal dispersion in each region shows larger dispersion in the high permeability region than the low permeability zone. This may caused by presence of dominant flow velocity and lower height of the region 1. As it has been shown in Figure 3.20, in the high permeability zone the piston-like displacement takes place from left to right direction.

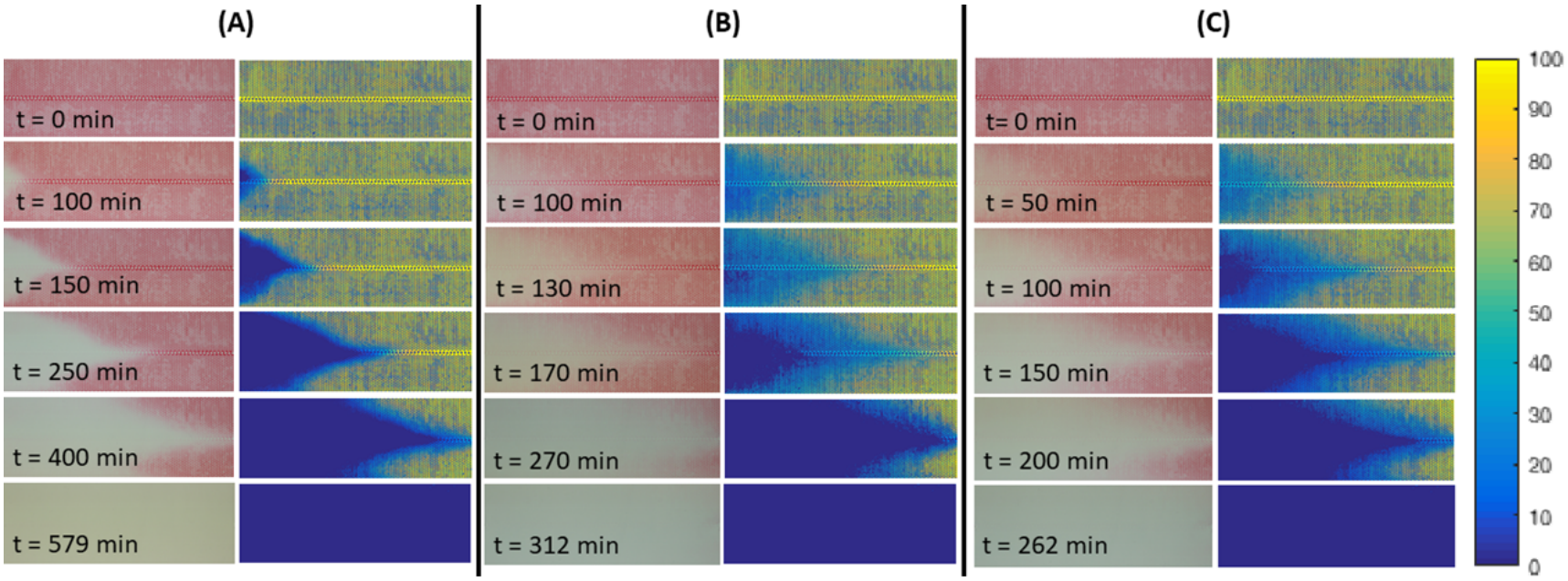

Figure 4.12: Images from the miscible displacement experiments. Scenario A is with injection rate of 0.002 cc/min, Scenario B is with injection rate of 0.004 cc/min and Scenario C is with injection rate of 0.006 cc/min. The left column of each scenario shows the actual experimental images while the right columns show the processed images (with injection from right to left of each image)

In the high permeability region due to very low height for the medium, advection and longitudinal dispersion terms have been taken into account and in the lower permeability medium, advection, longitudinal and transverse dispersion have been considered.

Table 4.3: Breakthrough time, longitudinal and transverse dispersion coefficients for various injection rates, where q is injection rate, v is interstitial velocity, T_{tot} is breakthrough displacement time, D_L is average longitudinal dispersion in the high permeability region, D_l is average longitudinal dispersion in the low permeability region, and D_t is average transverse dispersion coefficient in the low permeability region

q (cc/min)	v (m/s)	T_{tot} (min)	D_L (m^2/s)	D_l (m^2/s)	D_t (m^2/s)
0.002	8.2×10^{-5}	579	2.1×10^{-5}	1.4×10^{-7}	0.8×10^{-7}
0.004	1.6×10^{-4}	312	3.9×10^{-5}	3.8×10^{-7}	2.0×10^{-7}
0.006	2.5×10^{-4}	262	5.7×10^{-5}	5.1×10^{-7}	3.2×10^{-7}
0.008	3.3×10^{-4}	194	7.4×10^{-5}	6.6×10^{-7}	3.8×10^{-7}
0.010	4.1×10^{-4}	147	8.6×10^{-5}	7.7×10^{-7}	4.8×10^{-7}

4.2.3 Comparison of the Models

In this section, using the previously developed statistical and numerical models in this study, the longitudinal and transverse dispersion coefficients for single and dual permeability media are calculated. The sample of calculations for each experimental model is explained in the following and the comparison of three different developed models in this study and two well known models of Taylor [88] (Equation 2.1), De Josselin [51] (**??**), Schevan et.al [78] (2.3) and Saffman [76] (Equation 2.2) have been discussed. For statistical calculations, based on the Equation 3.21 longitudinal and transverse dispersion coefficients are defined as:

$$D_L = \frac{9\pi}{64}\frac{\langle l^2\rangle}{\langle l\rangle}\frac{\langle R^4\rangle}{\langle R^2\rangle^2}\langle v_x\rangle + \frac{\pi}{12}\frac{\langle l^2\rangle}{\langle l\rangle}\langle v_x\rangle \tag{4.4}$$

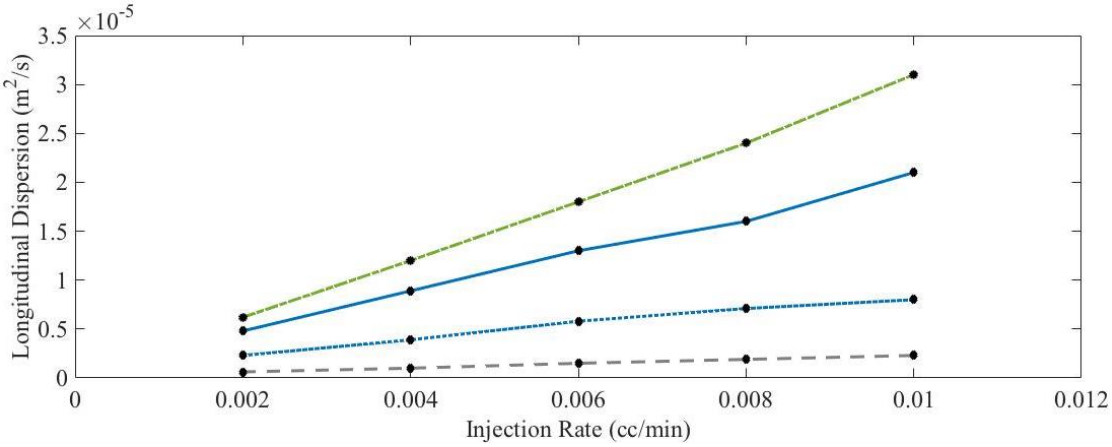

Figure 4.13: Comparison of experimental longitudinal dispersion coefficent with calculated ones from different models. The green (dash-dot) line is the proposed statistical model, blue (solid) line is the experimental results, blue (dot) line is the calculated coefficients from Taylor model and gray (dash) line is the calculated dispersion using Scheven et al., model (2014)

Using pore properties of the single permeability micromodel we can estimate the dispersion coefficients as:

$$D_L = \frac{9\pi}{64} \times \Big(1.86 \times 0.0052\Big) \times \Big(1.92\Big) \times \langle v_x \rangle + \frac{\pi}{12} \times \Big(1.86 \times 0.0052\Big) \times \langle v_x \rangle \quad (4.5)$$

for the longitudinal dispersion coefficient and as follows for the transverse dispersion coefficient:

$$D_T = \frac{3\pi}{64} \frac{\langle l^2 \rangle}{\langle l \rangle} \frac{\langle R^4 \rangle}{\langle R^2 \rangle^2} \langle v_x \rangle \quad (4.6)$$

$$D_T = \frac{3\pi}{64} \times \Big(1.86 \times 0.0052\Big) \times \Big(1.92\Big) \times \langle v_x \rangle \quad (4.7)$$

The developed image processing tool have been used to estimate each of the required parameters as summarized in the Tables 3.3 and 3.5. Statistical calculations: Same as the single permeability medium the required parameters have been calculated for both regions of high and low permeability zones. For statistical calculations, based on

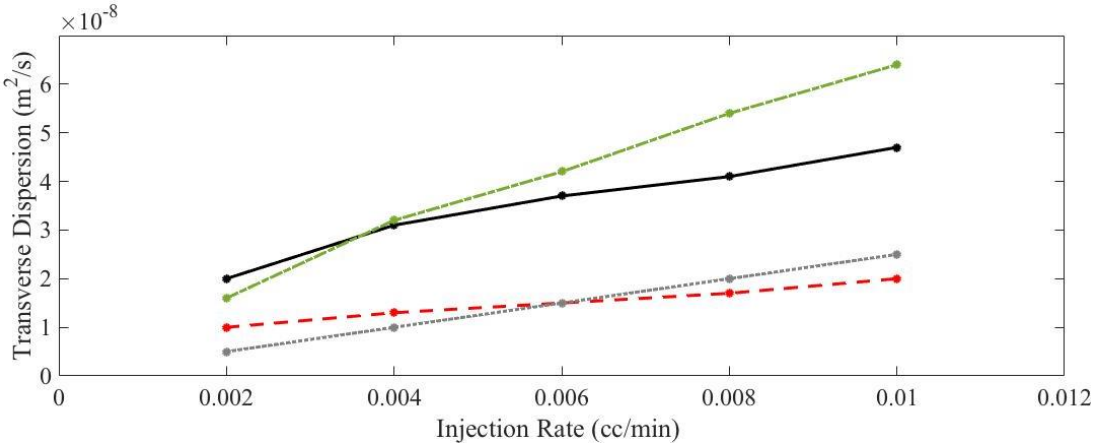

Figure 4.14: Comparison of experimental transverse dispersion coefficent with calculated ones from different models. The green (dash-dot) line is the proposed statistical model, black (solid) line is the experimental results, red (dash) line is the calculated coefficients from Saffman model and gray (dash) line is the calculated dispersion using De Joselin's model

the equation longitudinal and transverse dispersion coefficients are defined as below:

$$D_L = \frac{9\pi}{64} \times \Big(1.12 \times 0.021\Big) \times \Big(2.1\Big) \times \langle v_x \rangle + \frac{\pi}{12} \times \Big(1.12 \times 0.021\Big) \times \langle v_x \rangle \qquad (4.8)$$

$$D_l = \frac{9\pi}{64} \times \Big(1.93 \times 0.0044\Big) \times \Big(1.28\Big) \times \langle v_x \rangle + \frac{\pi}{12} \times \Big(1.93 \times 0.0044\Big) \times \langle v_x \rangle \qquad (4.9)$$

and for transverse dispersion in the low permeability region:

$$D_t = \frac{3\pi}{64} \times \Big(1.93 \times 0.0044\Big) \times \Big(1.23\Big) \times \langle v_x \rangle \qquad (4.10)$$

To accomplish the numerical simulation, the ADE introduced in the Equation 3.56 has been solved for the experimental condition. Although both regions have longitudinal dispersion terms, the longitudinal coefficient in the high permeability region is considered 20 times larger than the lower permeability zone. The assumptions appear reasonable in circumstances of the relatively smaller contribution of dispersion terms

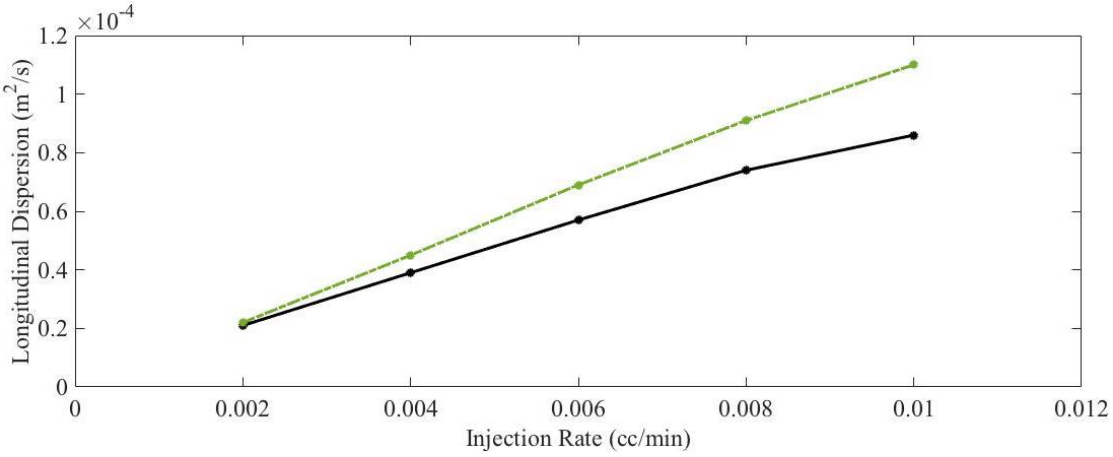

Figure 4.15: Comparison of experimental longitudinal dispersion coefficent black (solid) line for the high permeability region of the dual permeability micromodel with calculated one from the proposed statistical model (green dash-dot line)

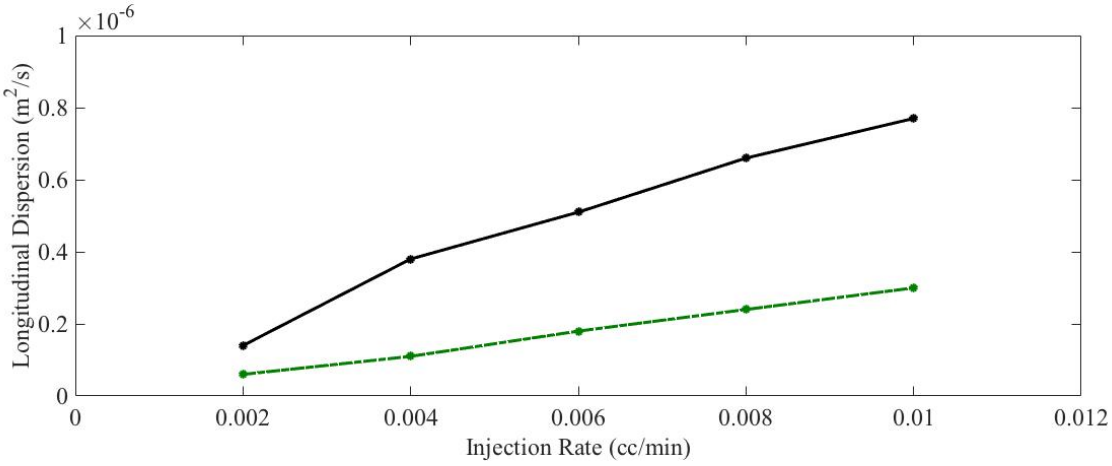

Figure 4.16: Comparison of experimental longitudinal dispersion coefficent black (solid) line for the low permeability region of the dual permeability micromodel with calculated one from the proposed statistical model (green dash-dot line)

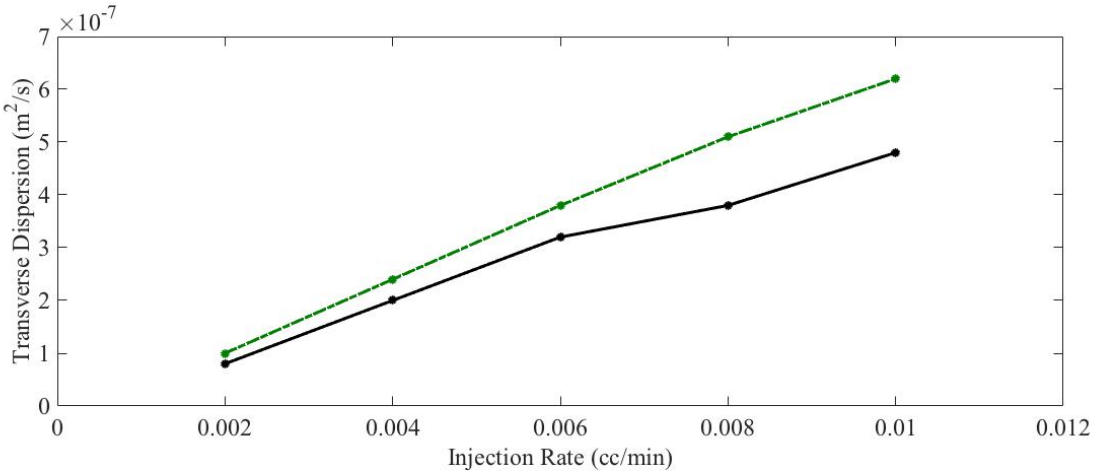

Figure 4.17: Comparison of experimental transverse dispersion coefficent black (solid) line for low permeability region of the dual permeability micromodel with calculated one from the proposed statistical model (the green or dash-dot line)

to spreading of displacing fluid when there is a clear difference in velocity between the two regions. The numerical simulation shows a solid agreement with experimental results.

As illustrated in the Figures 4.15, 4.16, and 4.17 the statistical model shows higher values for the dispersion coefficients than experimental results. As it was discussed in the section 3.6, the residence time for displacing particles plays a significant role in the precision of the statistical models. The better agreement at lower velocities implies a better agreement of the residence time estimation and consequently dispersion coefficients. This can be explained qualitatively by noting that low flow velocities have ample time to occupy wider stream tubes than high velocities because of fluid volume conservation.

4.2.4 Numerical-Statistical Simulation Validation

In this section, the calculated dispersion coefficients for the porous medium using the statistical estimation is implemented in introduced numerical simulation in Section

3.9. In the high permeability region due to very low height for the medium, advection and longitudinal dispersion terms have been considered and in the lower permeability medium, advection, longitudinal and transverse dispersion have been considered. Table 4.3 shows the assumed parameters and coefficients for the set of equations. The assumptions appear reasonable in circumstances of the relatively smaller contribution of dispersion terms to spreading of displacing fluid when there is a clear difference in velocity between the two regions.

As Figure 4.19 shows the implemented statistical dispersion coefficients in longitudinal and transverse directions shows an acceptable agreement qualitatively. Experimental results illustrated that the mixing zone is larger in high permeability region than lower permeability region. This observation also, concludes higher longitudinal dispersion coefficient in high permeability region due to dominant velocity and pore structure (higher pearmeability).

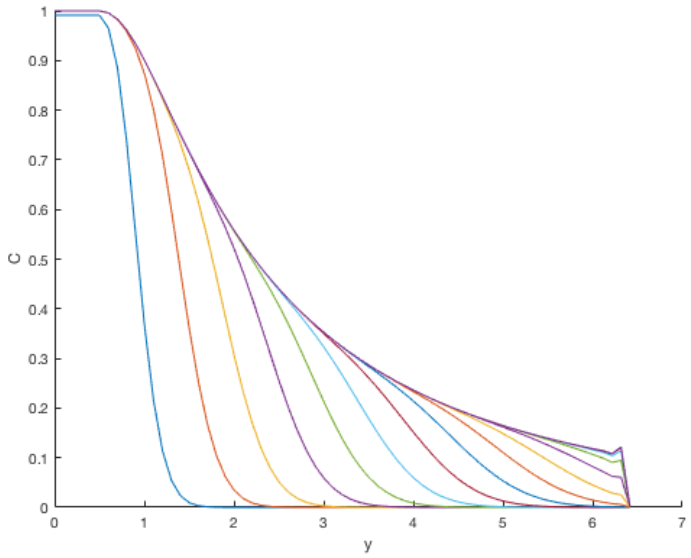

(a) Concentration change in y direction

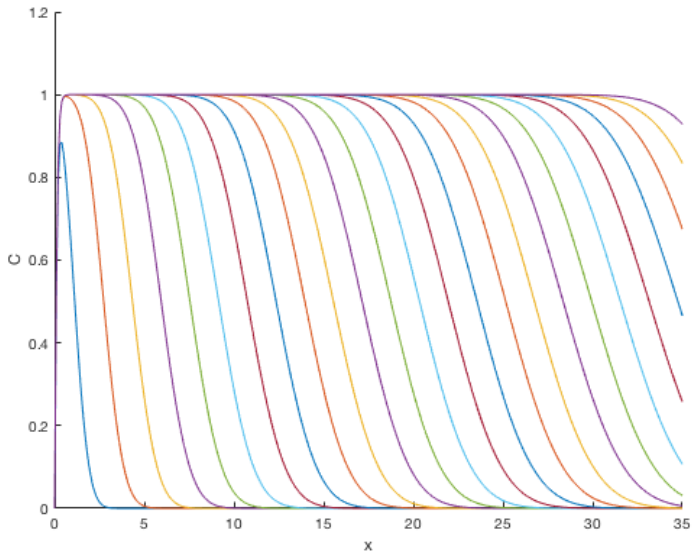

(b) Concentration change in x direction

Figure 4.18: Concentration change in x and y direction in dual permeability porous medium during the miscible discepalcement at breakthrough time for injection rate $0.002cc/min$, simulation output

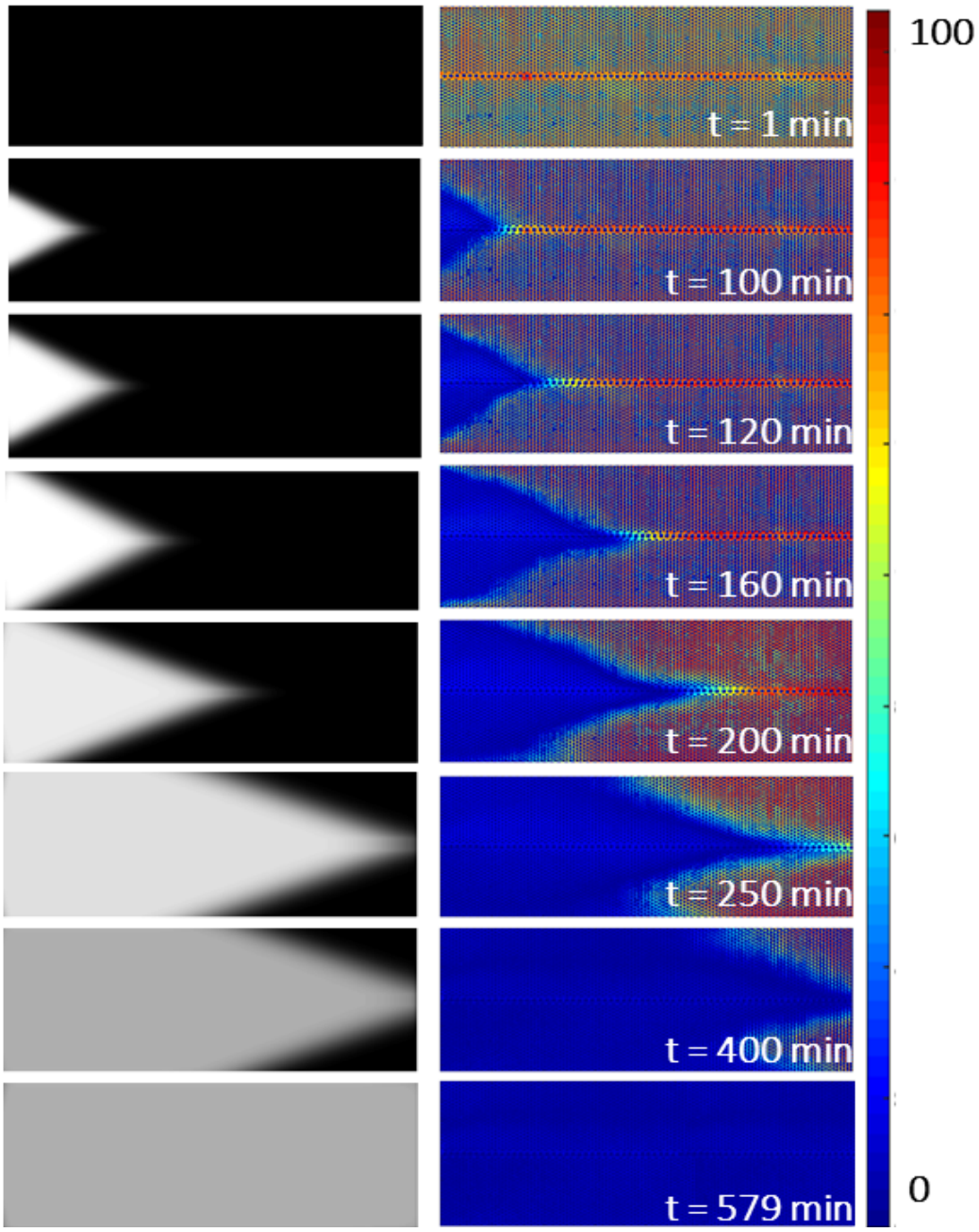

Figure 4.19: Numerical (with statistical dispersion coefficients) vs experimental results of miscible displacement progress over time for dual permeability porous medium

Chapter 5

Conclusions

This study presented the results of a statistical modeling and laboratory experiments in a two-dimensional porous media. The effects of varying displacing fluid velocity and porous media characteristics on the coupled longitudinal and transverse dispersion coefficients were estimated. A new methodology to estimate the experimental dispersion coefficients are proposed.

5.1 Conclusions

In this study, a systematic mathematical and experimental study is introduced on the water/water miscible displacement in a homogeneous anisotropic micromodel. A mathematical model to relate the dispersion coefficients to the pore properties of porous media, using a statistical approach has been developed. Assuming, the mechanical dispersion is dominant and molecular diffusion is negligible, the new equations for longitudinal and transverse dispersion coefficients have been introduced. In the following, four different porous media with different pore geometries have been assumed to investigate the effect of various parameters on longitudinal and transverse dispersion coefficients. The dispersion in both directions are non-linear functions of velocity

and depends on pore geometry of porous media. Pore throat diameter distribution affects dispersion similarly to permeability and increasing the degree of heterogeneity increases both D_L and D_T. However, longitudinal dispersion is more sensitive. The ratio of D_L to D_T is inversely proportional to dimensionless pore throat diameter and independent from distribution of pore throat length. Increasing dimensionless pore throat diameter decreases the ratio and lower values of of it leads to higher difference of D_L from D_T. An experimental approach to estimate the average longitudinal and transverse dispersion coefficients in a homogeneous anisotropic porous medium with and without fracture during a miscible displacement was designed and used to conduct a series of miscible flooding tests. Traditionally, most studies of miscible injection have focused on recovery and mechanism of the method and Peclet number that have been used to find the dispersion and diffusion coefficients from a mathematical correlations. This study utilizes a unique method to estimate the mass transfer properties. A custom and unique image processing tool was developed and used to analyze the developing mixing zone in the process and consequently processed images are used to collaborate with a developed Bayesian estimator tool to fit the dispersion coefficients in analytical solution of Advection-Diffusion Equation (ADE). The details of the approach are explained and obtained images are analyzed and interpreted. The results confirm the strong dependency of the velocity of the displacing fluid and dispersion coefficients in both directions of longitudinal and transverse. The effects of anisotropy on miscible mass transport are investigated in this study using an unique method. Some highlights of the research is listed below:

- The whole miscible displacement of dyed water by clear water is recorded and analyzed using a unique developed image processing tools and using analytical solution and Bayesian estimator, longitudinal and transverse dispersion coefficients are estimated. In this study a successful methodology to quantify the

coupled longitudinal and transverse dispersion in a miscible displacement have been demonstrated while the previous micromodel studies discuss only one direction.

- In this study, the Random Walk (RW) technique was used to develop a statistical modeling of dispersion in two-dimensional porous media. The extracted models were implemented into numerical solutions to simulate miscible displacement in heterogeneous porous media. The introduced statistical model is able to provide a more accurate initial assumption for current numerical and analytical models to simulate miscible displacement in porous media by taking the pore geometrical properties into account. Particularly, this method can help a more accurate simulation of the spreading of the fluids that is calculated by following the motion of a collection of particles.

- Experimental results showed that the mathematical models fit the miscible displacement dispersion coefficients in both parallel (longitudinal) and normal (transverse) directions respect to dominant injection velocity direction. obtained from miscible tests.

- Dispersion coefficients increase with fluid velocity in both directions.

- The effect of interstitial velocity on breakthrough time is carefully reported and decreasing breakthrough time (T_{tot}) with increase in velocity is observed.

- Experimental results illustrate that mixing is larger in high permeability regions than lower permeability regions. This observation also concludes that longitudinal dispersion is larger in high permeability region due to wider velocity profile and tortuous flow.

- Despite the significantly dominant longitudinal dispersion in high permeability

zones, longitudinal and transverse dispersion are on the same order of magnitude in low permeability regions. This indicates the effect of the presence of dominant velocity in the x-direction on the amplitude of the longitudinal dispersion.

- Simulation and experimental results show that longitudinal and transverse dispersion in low permeability regions are on the same order of magnitude. This is most possibly caused by absence of dominant velocity in the region.

5.2 Future Studies

In the current research using the given assumptions, the mathematical model presented is only valid for high Peclet numbers meaning mechanical dispersion is dominant and molecular diffusion is negligible. Further investigations to incorporate lower Peclet numbers where molecular diffusion is a significant contributor to hydrodynamic dispersion seems very interesting field to be followed up. For this purpose the problem needs to be reframed for when $t = \frac{8\langle l \rangle \left\langle R^2 \right\rangle^2}{3\pi \langle R^4 \rangle \langle v_x \rangle}$ is comparable with $\frac{\langle R \rangle^2}{8D_m}$. Another avenue could be the investigating the problem for the conditions when mechanical dispersion and molecular diffusion are both contributing, the random walk approach used in this research is not valid for this condition for two reasons.

1. The residence time is only crudely accounted for in the random walk theory.

2. the basis for the selection of a pore by a particle at a junction does not follow the simple probability density function previously derived, since diffusion becomes significant in comparison to advection. Particles no longer choose streamlines in proportion to the advective velocity along the streamline.

In this case, both mechanisms of advection and molecular diffusion are acting and the assumptions are no longer valid. In this situation, the average time step is sufficient

for molecular diffusion to ravel variations in concentration across the cross section of a the assumed pore element. Accounting for the motion caused by the effect of molecular diffusion, velocity is defined as a random function of the time. If follows that, the covariance of the velocity at a given time t and a later time $t + dt$ be considered a Lagrangian correlation function as $\langle v_t v_{t+dt} \rangle$. The displacement in the x and $y-$directions could be mathematically developed and experimentally studied.

Bibliography

[1] A. Aitken. On least squares and linear combinations of observations. *Proceedings of the Royal Society of Edinburgh*, 1935.

[2] A. Aksoy and M. S. Guney. Experimental determination of three-dimensional dispersivities in homogeneous porous medium. *Environmental Earth Sciences*, 2010.

[3] J. Aldrich. Doing least squares: Perspectives from gauss and yule. *International Statistic Review*.

[4] B. B. Alkindy A., Al-Wahaibi Y. and M. A. Investigation of longitudinal and transverse dispersion in stable displacements with a high viscosity and density contrast between the uids. *Journal of Contam*.

[5] L. Andrew, P. Meireles, and J. B. M. Pimbely. Use of the log-normal density function to analyze membrane pore size distribution: Functional forms and discrepancies. *J Mem Sci*, 1994.

[6] A. Aris. On the dispersion of a solute in a fluid flowing through a tube. *Royal Society of London*, 1956.

[7] W. B. Inertial effects in dispersion in porous media. *Water Resources Research*.

[8] J. Bear. *Dynamics of Fluids In Porous Media*. Elsevier, 1972.

[9] J. Bear and Bachmat. *Introduction to Modeling of Transport Phenomena in Porous Media*. Springer, 1990.

[10] T. W. Blackwell RJ, Rayne RJ. Factors influencing the efficiency of miscible displacement. *Petroleum Technology Journal*, 1959.

[11] H. B. Bradley, editor. *Petroleum Engineering handbook*. SPE, 1992.

[12] W. E. Brigham. Mixing equations in various geometries. *SPE*, 1986.

[13] W. E. Brigham, P. W. Reed, and J. N. Dew. Experiments on mixing during miscible displacement in porous media. *SPE*, 1961.

[14] J. S. Buckley. Multiphase displacements in micromodels. In *Interfacial Phenomena in Petroleum Recovery*, 1992.

[15] D. Buyuktas and W. W. Wallender. Dispersion in spatially periodic porous media. *Heat and Mass Transfer*, 2004.

[16] W. D. Buyuktas D. Dispersion in spatially periodic porous media. *Heat and Mass Transfer*.

[17] B. R. Carberry JJ. Axial dispersion of mass in flow through fixed beds. *AIChE*, 1958.

[18] P. Carman. Fluid flow through granular beds. *Institution of Chemical Engineers*, 1937.

[19] K. Chandrashekhar. Stochastic problems in physic and astronomy. *Review of Modern Physics*, 1943.

[20] S. Chang, F. Martin, and R. Grigg. Effect of pressure on co_2 foam displacements: A micromodel visualization study. *SPE*, 1994.

[21] R. V. Churchill. *Operational Mathematics*. McGraw-Hill, 1972.

[22] R. V. Churchill. *Operational Mathematics*. McGraw-Hill, 1972.

[23] K. H. Coats and B. D. Smith. Dead-end pore volume and dispersion in porous media. *SPE*, 1964.

[24] P. Danckwert. Continuous flow systems. *Chemical Eng. Journal*, 1953.

[25] E. DE. Dispersion and reaction in twodimensional model porous media. *Physics of Fluids A: Fluid Dynamics*.

[26] G. d. C. J. Delgado JMPQ. Measurement of the coefficient of transverse dispersion in packed beds over a range of values of schmidt number. *Journal of Transport Porous Media*.

[27] S. S. J. A. Djordjevich1, A. Explicit finite-difference solution of two-dimensional solute transport with periodic flow in homogenous porous media. *J. Hydrol. Hydromech*, 2015.

[28] F. Dullien. *Porous Media: Fluid Transport and Pore Structure*. Academic Press, 1992.

[29] W. L. H. R. Eidsath A., Carbonells R.G. Dispersion in pulsed systemsiii: Comparison between theory and experiments for packed beds. *Chemical Engineering Science*.

[30] A. Fayazi and M. H. Ghazanfari. Random walk simulation of miscible flow through heterogeneous 2d porous media considering dispersion tensor. *Chemical Engineering Science*, 2015.

[31] R. W. Fox and T. A. Mcdonald. *Introduction to Fluid Mechanics*. Wiley, 1998.

[32] Z. T. E. G. Freund H, Bauer J. Detailed simulation of transport processes in fixed-beds. *Ind Eng Chem Res*.

[33] J. J. Fried and M. A. Cambarnus. *Dispersion in porous media, advances in hydro science*. Academic Press, 1971.

[34] W. B. Golfier F, Quintard M. Comparison of theory and experiment for solute transport in weakly heterogeneous bimodal porous media. *Advances in Water Resources*.

[35] I. S. Gradshteyn and I. M. Ryzhik. *Analytical Solution for One-, Two-, and Three-Dimensional Solute Transport in Groundwater Systems with Uniform Flow*. Tables of Integrals, Series, and Products, 2007.

[36] F. E. Grane and G. H. Gardner. Measurements of transverse dispersion in granular media. *Journal of chemical engineering*, 1961.

[37] R. A. Greenkorn. *Flow phenomena in porous media.* Marcel Dekker INC, 1983.

[38] P. C. Gunn D.J. Dispersion in packed beds. *Journal of ICheME*.

[39] M. G.-N.-K. J. H. M. Nick, R. Schotting. Modeling transverse dispersion and variable density flow in porous media. *Transport in Porous Media*.

[40] . L. L. Haldorsen, H. A new approach to shale management in field-scale models. *SPE Journal*, 1984.

[41] C. R. Han NW, Bhakta J. Longitudinal and lateral dispersion in packed beds: effect of column length and particle size distribution. *Journal of AIChE*.

[42] R. Haring and R. Greenkorn. A statistical model of a porous medium with non-uniform pores. *AICheE*, 1970.

[43] S. M. Hassanizadeh and J. W. V. A. Leijnse. Experimental study of brine transport in porous media. *RIVM Report*, 1990.

[44] S. M. Hassanizadeh and A. Leijnse. A non-linear theory of high concentration gradient dispersion in porous media. *Water resource development*, 1995.

[45] A. J. Hoops and D. R. Harleman. Dispersion in radial flow from a recharge well. *Journal of Geophysic*, 1967.

[46] A. Hunt and T. Skinner. Dispersion of solutes in porous media. *European Physical Journal*, 2011.

[47] B. Hunt. Dispersive sources in uniform ground-water. *J. Hydraul. Div. Am. Sac. Civ. Eng.*, 1978.

[48] W. S. I. Park. Modeling non-fickian pollutant mixing in open channel flows using two-dimensional particle dispersion model. *Advances in Water Resource*.

[49] S. I.M. Calculation of coefficients longitudinal mass transport in the flow of solutions through a nonsorbing bed. *Journal of Applied Chemistry*, 1961.

[50] T. E. Johansen. *Principles of reservoir engineering*. Thormod E. Johansen, 2008.

[51] G. D. Josselin. Longitudinal and transverse diffusion in granular deposits. *American Geophysic*, 1958.

[52] L. F. Khilyuk and G. V. Chilingar. *Probability in Petroleum and Environmental Engineering*. Gulf Publishing, 2005.

[53] J. K.-H. K.-D.-J. Kim, S.-B. and W. Jury. Determination of two-dimensional laboratory-scale dispersivities. *Hydrological Processes*, 2010.

[54] D. Koch and J. Brady. Dispersion in fixed beds. *Fluid Mechanics*, 1985.

[55] A. G. Kramers H. Frequency response analysis of continuous flow systems. *Chemical Eng. Science*, 1953.

[56] N. M. Kulkarni and D. N. Rao. Experimental investigation of miscible and immiscible water- alternating-gas (wag) process performance. *Journal of Petroleum Science & Engineering*, 2005.

[57] L. W. Lake. *Enhanced Oil Recovery*. SPE, 2010.

[58] A. J. Landman. *Analysis of physical mechanisms underlying densitydepen- dent transport in porous media*. PhD thesis, Delft University of Technology, 2005.

[59] H. D. LugoMendez, F. J. ValdesParada, and J. A. O. Tapia. An analytical expression for the dispersion coefficient in porous media using chang's unit cell. *Journal of Porous media*, 2013.

[60] W. J. Lyman, W. F. Reehl, and D. H. Rosenblatt. *Handbook of Chemical Property Estimation Methods*. American Geochemical Society, 1990.

[61] D. C. G. V. Majdalani S., Chazarin J.P. Solute transport in periodical heterogeneous porous media: importance of observation scale and experimental sampling. *Journal of Hydrology*.

[62] H. A. Makse, J. S. Andrade, and H. E. Stanley. Tracer dispersion in a percolation network with spatial correlations. *Physical Review*, 2000.

[63] K. T. Miyauchi T. Axial dispersion in packed beds. *Journal of Chemical Eng. and Sci.*

[64] K. Mogensen, P. Hood, R. . A. Jones, and R. Noman. Gas injection project in the kharaib b reservoir of the giant al shaheen field. *SPE*, 2010.

[65] M. N. Ozisik. *Heat Conduction*. John Wiley and sons, 1980.

[66] T. K. Perkins and O. C. Johnston. A review of diffusion and dispersion in porous media. *AIME*, 1963.

[67] J. K. W. R. A. Dawe, E. G. Mahers. *Pore scale physical modeling of transport phenomena in porous media*. Martinus Nijhoff, Dordrecht, 1987.

[68] W. S. R.B. Bird and E. Lightfoot. *Transport Phenomena*. Wiley, 1960.

[69] R. Reid, J. Prausnitz, and B. Poling. *The Properties of Gases and Liquids*. McGraw Hill, 1987.

[70] C. R.G. Effect of pore distribution and flow segregation on dispersion in porous media. *Chemical Engineering Science*.

[71] J. Rice. *Mathematical Statistics and Data Analysis*. Duxbury Press, 1995.

[72] J. D. Rogers and R. B. Grigg. A literature analysis of the wag injectivity abnormalities in the co2 process. *SPE*, 2001.

[73] L. A. J. Saeid Eskandari. Experimental and numerical investigation of dispersion in a dual permeability porous medium during miscible displacement. In *Society of Core Analysis*, 2017.

[74] P. Saffman. A theory of dispersion in a porous medium. *Journal of Fluid Mechanic*, 1959.

[75] M. Sahimi. *Flow and Transport in Porous Media and Fractured Rock*. VCH, 1995.

[76] M. Sahimi. Dispersion in porous media, continuous-time random walks, and percolation. *Physical Review*, 2012.

[77] K. M. Sahraoui M. Slip and no-slip temperature boundary conditions at the interface of porous, plain media: Convection. *International Journal of Heat and Mass Transfer*.

[78] U. M. Scheven, A. D. S. Khirevich, and U. Tallarek. Longitudinal and transverse dispersion in flow through random packing of spheres: A quantitative comparison of experiments, simulations, and models. *Physical Review*, 2014.

[79] D. A. T. U. Scheven U.M., Khirevich S. Longitudinal and transverse dispersion in flow through random packings of spheres: A quantitative comparison of experiments, simulations, and models. *Physical Review*.

[80] K. L. Silliman, S.E. and C. Voss. Laboratory investigation of longitudinal dispersion in anisotropic porous media. *Water Resources Research*, 1987.

[81] A. Skauge and E. I. Dale. Progress in immiscible wag modelling. *SPE*, 2007.

[82] R. W. Stallman. *Multiphase fluids in porous media- A review of theories pertinent of hydrologic studies*. Geological survey, 1964.

[83] B. Starke and M. Koch. Laboratory experiments and monte carlo simuations to validate a stochastic theory of density-dependent macro dispersion. *Water resource development*, 2006.

[84] S. Sternberg. Dispersion measurements in highly heterogeneous laboratory scale porous media. *Journal of Transport in Porous media*, 2004.

[85] S. M. Stigler. Gauss and the invention of least squares. *Statist*.

[86] S. Sundaresan, R. Amundson, and R. Aris. Observations on fixed bed dispersion models- the role of the interstitial fluid. *AIChE*, 1980.

[87] G. Taylor. Dispersion of soluble matter in solvent flowing slowly through a tube. *Royal Society of London*, 1953.

[88] G. Taylor. Conditions under which dispersion of a solute in a stream of solvent can be used to measure molecular diffusion. *Royal Society of London*, 1957.

[89] N. Toride, F. J. Leji, and M. T. van Genuchten. Convective-dispersive stream tube model for field-scale solute transport: I. moment analysis. *Soil Science Society of America Journal*, 1996.

[90] L. Ujfaludi. Longitudinal dispersion tests in non-uniform porous media. *Water resource development*, 1986.

[91] A. W. van Genuchten, M. Analytical solutions of the one-dimensional convectivedispersive solute transport equation. *US Department of Agriculture*, 1982.

[92] S. J. Watson, D. A. Barry, R. J. Schotting, and S. M. Hassanizadeh. Validation of classical density dependent solute transport theory for stable, high concentration gradient brine displacements in coarse and medium sands. *Advance Water Resources*, 2002.

[93] E. Wexler. Analytical solution for one-, two-, and three-dimensional solute transport in groundwater systems with uniform flow. *U.S Geological Survey*, 1989.

Appendix A

Mathematical Details

A.1 Fundamentals of Statistics

In statistic distributions of random variables can be stated in terms of a Cumulative Distribution Function (CDF), $F(x)$, which is the probability that the pore diameter is equal to or less than x, or in terms of the Probability Density Function (PDF), $f(x)$, which is equal to the derivative of $F(x)$ with respect to x as Equation A.1.

$$f(x) = \frac{dF(x)}{dx} \tag{A.1}$$

Since $F(x)$ is continuous and monotonically increasing, its derivative exists for all values of x. $f(x)$ is equal to the number of pores with diameters between $x - \delta x$ and $x + \delta x$ divided by $2\delta x$, in the limit as δx approaches zero. In fact, the pore structure of a porous medium is described by the pore size distribution and a pore size distribution curve represents the cumulative fraction of the total pore volume within a porous sample composed of particular ranges of pore sizes [5].

A.2 Central Limit Theorem

The central limit theorem and the law of large numbers are the two fundamental theorems of probability. Roughly, the central limit theorem states that the distribution of the sum (or average) of a large number of independent, identically distributed variables will be approximately normal, regardless of the underlying distribution. The importance of the central limit theorem is hard to overstate; indeed it is the reason that many statistical procedures work. [71]. Let $X_1, ..., X_n$ be a random sample of size n, that is, a sequence of independent and identically distributed random variables drawn from distributions of expected values given by μ and finite variances given by σ^2. Suppose we are interested in the sample average:

$$S_n := \frac{X_1 + \cdots + X_n}{n} \tag{A.2}$$

of these random variables. By the law of large numbers, the sample averages converge in probability and almost surely to the expected value μ as $n \longrightarrow \infty$. The classical central limit theorem describes the size and the distributional form of the stochastic fluctuations around the deterministic number μ during this convergence. More precisely, it states that as n gets larger, the distribution of the difference between the sample average S_n and its limit μ, when multiplied by the factor $\sqrt{n}$ (that is $\sqrt{n}(S_n - \mu)$), approximates the normal distribution with mean O and variance σ^2. For large enough n, the distribution of S_n is close to the normal distribution with mean μ and variance σ^2/n. The usefulness of the theorem is that the distribution of $\sqrt{n}(S_n - \mu)$ approaches normality regardless of the shape of the distribution of the individual X_i's.

$$\sqrt{n}\left(\left(\frac{1}{n}\sum_{i=1}^{n} X_i\right) - \mu\right) \xrightarrow{d} N(0,\ \sigma^2) \tag{A.3}$$

A.3 Adjustable Parameters Description

We can define the dimensionless wetting phase saturation, S_D, as below [50]:

$$S_D = \frac{S_w - S_{wr}}{1 - S_{wr}} = \frac{V_x}{V_{tot}} \tag{A.4}$$

Where S_D is based on the pore space available at irreducible water saturation. Hence, the wetting phase saturation of an ideal porous medium is:

$$S_D = \int_{R_{min}}^{R_{max}} f(R)dR \Rightarrow f(R) = \frac{dS_D}{dR} = \frac{d(\frac{V_x}{V_{tot}})}{dR} \tag{A.5}$$

Where V_x is the cumulative volume of water in the throat and voids connected to them and V_{tot} is the total cumulative volume of water. If you feed the Equation A.5 with considered function for pore throat diameter Equation 3.1, we can perform the integration and find the statement for α.

$$f(R) = \alpha\beta^\gamma R^{\gamma-1}e^{-(R\beta)^\gamma} = \frac{dS_D}{dR} \Rightarrow S_D = \int_{R_{min}}^{R_{max}} \alpha\beta^\gamma R^{\gamma-1}e^{-(R\beta)^\gamma}dR \tag{A.6}$$

$$S_D = \alpha(1 - e^{-(\beta R)^\gamma}) \Rightarrow \alpha = \frac{S_D}{(1-e^{-(\beta R)^\gamma})} \xrightarrow{R=R_{max}} \alpha = \frac{1}{(1-e^{-(\beta R_{max})^\gamma})} \tag{A.7}$$

Theoretically as R_{max} goes to infinity, α should be zero, and the entry capillary pressure will be zero as well.

A.4 Normalization Factor

In probability theory, a normalizing constant is a constant by which an everywhere non negative function must be multiplied so the area under its graph is 1, to make it a probability density function or a probability mass function. We defined our pore size and length distribution function before. To find the normalization factor (ζ) of

probability function we can write:

$$1 = N\left(\left(\int_{l_{min}}^{l_{max}} f(l)dl\right)\left(\int_{D_{min}}^{D_{max}} f(D)dD\right)\left(\int_{-\pi/2}^{\pi/2}\cos\theta d\theta\right)\right) \tag{A.8}$$

However,

$$\int_{l_{min}}^{l_{max}} g(l)dl = 1 \qquad ; \qquad \int_{R_{min}}^{R_{max}} f(R)dR = 1 \tag{A.9}$$

Substituting the values in normalization equation results in:

$$N(\int_{-\pi/2}^{\pi/2}\cos\theta d\theta) = 1 \qquad \Rightarrow 2N = 1 \Rightarrow N = \frac{1}{2} \tag{A.10}$$

Same procedure can be applied for normalization factor in probability of path existence.

$$\int_{\Psi} d\Psi = \tfrac{\zeta\pi R^2}{4}\left(\underbrace{-\frac{R^2}{32\mu}\frac{\Delta p}{L_n}\cos\theta}_{\text{Velocity}}\right)\left(\underbrace{\frac{1}{2}\int_{R_{min}}^{R_{max}} f(R)dR\int_{l_{min}}^{l_{max}} g(l)dl\int_{-\pi/2}^{\pi/2}\cos\theta d\theta}_{\text{pore probability}}\right) \tag{A.11}$$

$$= \tfrac{\zeta\pi\Delta p}{256\mu L_n}\left(\underbrace{\int_{R_{min}}^{R_{max}} R^4 f(R)dR}_{\langle R^4\rangle}\right)\left(\underbrace{\int_{l_{min}}^{l_{max}} g(l)dl}_{1}\right)\left(\underbrace{\int_{-\pi/2}^{\pi/2}\cos^2\theta d\theta}_{\pi/2}\right) \tag{A.12}$$

$$\frac{\zeta\pi^2\Delta p\,\langle R^4\rangle}{512\mu L_n} = 1 \Rightarrow \zeta = -\frac{512\mu L_n}{\pi^2\Delta p\,\langle R^4\rangle} \tag{A.13}$$

Substituting of ζ in Equation 3.6 results the final statement for $d\Psi$:

$$d\Psi = \frac{-512\mu L_n}{\pi^2\Delta p\,\langle R^4\rangle}\frac{\pi R^2}{4}\left(\frac{-R^2}{32\mu}\frac{\Delta p}{L_n}\cos\theta\right)\left(\frac{1}{2}\ f(R)dR\ g(l)dl\ \cos\theta d\theta\right) \tag{A.14}$$

$$d\Psi = \frac{2}{\pi\,\langle R^4\rangle}\ g(l)dl\ R^4 f(R)dR\ \cos^2\theta d\theta \tag{A.15}$$

A.5 Theory of Moments

In statistic, a moment is a specific quantitative measure of the shape of a set of points. The zeroth moment is the total probability, the first moment is the mean, the second moment is the variance, and the third moment is the skewness. The normalised $n-th$ central moment or standardized moment is the $n-th$ central moment divided by σ_n; the normalised $n-th$ central moment of

$$x = \frac{\langle (x-\mu)^n \rangle}{\sigma^n}. \tag{A.16}$$

These normalised central moments are dimensionless quantities, which represent the distribution independently of any linear change of scale. For example Let $f(x)$ be any function which is defined and positive on an interval $[a, b]$. We might refer to the function as a distribution, whether or not we consider it to be a probability density distribution. Then we will define the following moments of this function:

$$\langle M \rangle = M_0 = \textstyle\int_a^b f(x)dx \qquad \left\langle M^2 \right\rangle = M_1 = \displaystyle\int_a^b xf(x)dx \tag{A.17}$$

$$\langle M^3 \rangle = M_2 = \textstyle\int_a^b x^2 f(x)dx \qquad \left\langle M^4 \right\rangle = M_4 = \displaystyle\int_a^b x^n f(x)dx \tag{A.18}$$

$$\tag{A.19}$$

- Mean (Average): The first raw moment is the mean.
- Variance: The second central moment is the variance. Its positive square root is the standard deviation σ.
- Skewness: The third central moment is a measure of the lopsidedness of the distribution.
- Kurtosis: The fourth central moment is a measure of whether the distribution

is tall and skinny or short and squat. If a distribution has a peak at the mean and long tails, the fourth moment will be high and the kurtosis positive; conversely, bounded distributions tend to have low kurtosis. The kurtosis can be positive without limit. Based on Equation A.16 if σ is the variance of $f(x)$ then normalized kurtosis can be defined as below:

$$K_N = \frac{\langle (x-\mu)^4 \rangle}{\sigma^2} \tag{A.20}$$

A.6 Random walk theory

A random walk is a mathematical formalization of a path that consists of a succession of random steps. Random walks are related to the diffusion models and are a fundamental topic in discussions of Markov processes. Several properties of random walks, including dispersal distributions, first-passage times and encounter rates, have been extensively studied.

A.7 Calculation of Variances

In probability theory, variance measures how a set of random variables is spread out around the average (mean). A variance of zero indicates that all the values are identical. Variance is always non negative value and playing a main role in understanding the heterogeneity of a distribution. Find the σ_x and σ_y in chapter 3 in full details is

presented here.

$$n\left\langle l\right\rangle^2\sigma_x^2 \quad = n\langle(x_n-\langle x_n\rangle)^2\rangle = n\int_\Psi l^2\cos^2\theta d\Psi - n(\tfrac{8\langle l\rangle}{3\pi})^2 \tag{A.21}$$

$$= \tfrac{2n}{\pi\langle R^4\rangle}\underbrace{\int_{l_{min}}^{l_{max}} l^2 g(l)dl}_{\langle l^2\rangle}\underbrace{\int_{R_{min}}^{R_{max}} R^4 f(R)dR}_{\langle R^4\rangle}\underbrace{\int_{-\pi/2}^{\pi/2}\cos^4\theta d\theta}_{\frac{3\pi}{8}} \tag{A.22}$$

$$-n(\tfrac{8\langle l\rangle}{3\pi})^2 = \tfrac{3n\langle l^2\rangle}{4} - \tfrac{64n\langle l\rangle^2}{9\pi^2} \Rightarrow \sigma_x^2 = \tfrac{3\langle l^2\rangle}{4\langle l\rangle^2} - \tfrac{64}{9\pi^2} \tag{A.23}$$

Same work has been done for y direction below:

$$n\left\langle l\right\rangle^2\sigma_y^2 \quad = n\langle(y_n-\langle y_n\rangle)^2\rangle = n\int_\Psi l^2\sin^2\theta d\Psi - \underbrace{0}_{\text{from Equation 3.30}} \tag{A.24}$$

$$= \tfrac{2n}{\pi\langle R^4\rangle}\underbrace{\int_{l_{min}}^{l_{max}} l^2 g(l)dl}_{\langle l^2\rangle}\underbrace{\int_{R_{min}}^{R_{max}} R^4 f(R)dR}_{\langle R^4\rangle}\underbrace{\int_{-\pi/2}^{\pi/2}\sin^2\theta\cos^2\theta d\theta}_{\frac{4\pi}{32}} \tag{A.25}$$

$$= \tfrac{n\langle l^2\rangle}{4} \Rightarrow \sigma_y^2 = \tfrac{\langle l^2\rangle}{4\langle l\rangle^2} \tag{A.26}$$

Variance of time:

$$n\frac{\langle l\rangle^2}{\langle v_x\rangle^2}\sigma_t^2 \quad = \langle(T_n-\langle T_n\rangle)^2\rangle = n\langle(t_n-\langle t_n\rangle)^2\rangle = n\int_\Psi(\tfrac{l}{v})^2 d\Psi - n\langle t\rangle^2 \tag{A.27}$$

$$\xrightarrow{\text{v from Equation 3.8}} \quad = \tfrac{8n\langle R^2\rangle^2}{9\pi\langle R^4\rangle\langle v_x\rangle^2}\underbrace{\int_{l_{min}}^{l_{max}} l^2 g(l)dl}_{\langle l^2\rangle}\underbrace{\int_{R_{min}}^{R_{max}} f(R)dR}_{1}\underbrace{\int_{-\frac{\pi}{2}}^{\frac{\pi}{2}} d\theta}_{\pi} - n\langle t\rangle^2 \tag{A.28}$$

$$= \tfrac{8n\langle R^2\rangle^2\langle l^2\rangle}{9\langle R^4\rangle\langle v_x\rangle^2} - n\left(\tfrac{8\langle l\rangle\left\langle R^2\right\rangle^2}{3\pi\langle R^4\rangle\langle v_x\rangle}\right)^2 \Rightarrow \sigma_t = \tfrac{8\langle R^2\rangle^2\langle l^2\rangle}{9\langle R^4\rangle\langle l\rangle^2} - \tfrac{64\left\langle R^2\right\rangle^4}{9\pi^2\langle R^4\rangle^2} \tag{A.29}$$

A.8 Covariance

In probability theory and statistics, covariance is a measure of how much two random variables change together. If the greater values of one variable mainly correspond with

the greater values of the other variable, and the same holds for the smaller values, the variables tend to show similar behaviour, the covariance is positive. In the opposite case, when the greater values of one variable mainly correspond to the smaller values of the other, the variables tend to show opposite behaviour, the covariance is negative. The sign of the covariance therefore shows the tendency in the linear relationship between the variables. The magnitude of the covariance is not easy to interpret. In this study, we require to calculate the covariance two random variables x and t. For this purpose we need to define the covariance mathematically first.

$$\frac{n\langle l\rangle^2}{\langle v_x\rangle}\sigma_{xt}^2 = \langle (T_n - \langle T_n\rangle)(X_n - \langle X_n\rangle)\rangle = \langle T_n X_n\rangle - \langle T_n\rangle\langle X_n\rangle - \langle T_n\rangle\langle X_n\rangle + \tag{A.30}$$

$$\langle T_n\rangle\langle X_n\rangle = \langle T_n X_n\rangle - \langle T_n\rangle\langle X_n\rangle = n\langle t_n x_n\rangle - n\langle t_n\rangle\langle x_n\rangle = n\int_\Psi \frac{l^2\cos\theta}{v}d\Psi - \tag{A.31}$$

$$n\langle t_n\rangle\langle x_n\rangle = n\frac{4\langle R^2\rangle}{3\pi\langle R^4\rangle\langle v_x\rangle}\underbrace{\int_{l_{min}}^{l_{max}} l^2 g(l)dl}_{\langle l^2\rangle}\underbrace{\int_{R_{min}}^{R_{max}} R^2 f(R)dR}_{\langle R^2\rangle}\underbrace{\int_{-\frac{\pi}{2}}^{\frac{\pi}{2}}\cos\theta d\theta}_{\pi/2} - \tag{A.32}$$

$$n\langle t_n\rangle\langle x_n\rangle = n\frac{2\langle R^2\rangle^2\langle l^2\rangle}{3\langle R^4\rangle\langle v_x\rangle} - n\left(\frac{8\langle l\rangle\langle R^2\rangle^2}{3\pi\langle R^4\rangle\langle v_x\rangle}\right)\left(\frac{8\langle l\rangle}{3\pi}\right) \xrightarrow{\text{simplification and rearrangement}} \tag{A.33}$$

$$\sigma_{xt} = \frac{2\langle R^2\rangle^2\langle l^2\rangle}{3\langle R^4\rangle\langle l\rangle^2} - \frac{64\langle R^2\rangle^2}{9\pi^2\langle R^4\rangle} \tag{A.34}$$

A.9 Dimensionless Variables Analysis

It is stated that the dimensionless variables χ, η and τ are defined to have mean equal to zero and variances equal to σ_x^2, σ_y^2 and σ_t^2 respectively. The calculation for mean is as below:

$$\chi = \frac{X_n - \langle X_n\rangle}{\langle l\rangle\sqrt{n}} \Rightarrow \langle\chi\rangle = \frac{\langle X_n - \langle X_n\rangle\rangle}{\langle l\rangle\sqrt{n}} = \frac{\langle X_n\rangle - \langle X_n\rangle}{\langle l\rangle\sqrt{n}} \Rightarrow \langle\chi\rangle = 0 \tag{A.35}$$

$$\eta = \frac{Y_n - \langle Y_n\rangle}{\langle l\rangle\sqrt{n}} \Rightarrow \langle\eta\rangle = \frac{\langle Y_n - \langle Y_n\rangle\rangle}{\langle l\rangle\sqrt{n}} = \frac{\langle Y_n\rangle - \langle Y_n\rangle}{\langle l\rangle\sqrt{n}} \Rightarrow \langle\eta\rangle = 0 \tag{A.36}$$

$$\tau = \frac{T_n - \langle T_n\rangle}{\frac{\langle l\rangle\sqrt{n}}{\langle v_x\rangle}} \Rightarrow \langle\tau\rangle = \frac{\langle T_n - \langle T_n\rangle\rangle}{\frac{\langle l\rangle\sqrt{n}}{\langle v_x\rangle}} = \frac{\langle T_n\rangle - \langle T_n\rangle}{\frac{\langle l\rangle\sqrt{n}}{\langle v_x\rangle}} \Rightarrow \langle\tau\rangle = 0 \tag{A.37}$$

And for variances as below:

$$\langle \chi^2 \rangle = \frac{\langle (X_n - \langle X_n \rangle)^2 \rangle}{\langle l \rangle^2 n} \xrightarrow{\text{From Appendix A.7}} \langle \chi^2 \rangle = \frac{\langle l \rangle^2 n \sigma_x^2}{\langle l \rangle^2 n} \Rightarrow \langle \chi^2 \rangle = \sigma_x^2 \quad \text{(A.38)}$$

$$\langle \eta^2 \rangle = \frac{\langle (Y_n - \langle Y_n \rangle)^2 \rangle}{\langle l \rangle^2 n} \xrightarrow{\text{From Appendix A.7}} \langle \chi^2 \rangle = \frac{\langle l \rangle^2 n \sigma_y^2}{\langle l \rangle^2 n} \Rightarrow \langle \eta^2 \rangle = \sigma_y^2 \quad \text{(A.39)}$$

$$\langle \tau^2 \rangle = \frac{\langle (T_n - \langle T_n \rangle)^2 \rangle}{\frac{\langle l \rangle^2 n}{\langle v_x \rangle^2}} \xrightarrow{\text{From Appendix A.7}} \langle \chi^2 \rangle = \frac{\langle l \rangle^2 n \sigma_t^2}{\frac{\langle l \rangle^2 n}{\langle v_x \rangle^2}} \Rightarrow \langle \tau^2 \rangle = \sigma_t^2 \quad \text{(A.40)}$$

A.10 Mean Squared Displacement

To find the MSD, one can take one of two paths: one can explicitly calculate $\langle x^2 \rangle$ and $\langle x \rangle$, then plug the result back into the definition of the MSD; or one could find the moment generating function, an extremely useful, and general function when dealing with probability densities. The moment generating function describes the k^{th} moment of the PDF. The first moment of the displacement PDF shown above is simply the mean: $\langle x \rangle$. The second moment is given as $\langle x^2 \rangle$. So then, to find the moment generating function it is convenient to introduce the characteristic function:[disambiguation needed]

$$G(k) = \langle e^{ikx} \rangle \equiv \textstyle\int_I e^{ikx} P(x,t|x_0) dx = G(k) = \sum_{m=0}^{\infty} \frac{(ik)^m}{m!} \mu_m \quad \text{(A.41)}$$

$$\ln(G(k)) = \textstyle\sum_{m=1}^{\infty} \frac{(ik)^m}{m!} \kappa_m = \sum_{m=1}^{\infty} \frac{(ik)^m}{m!} \kappa_m \quad \text{(A.42)}$$

, where κ_m is the m^{th} cumulant of x. The first two cumulants are related to the first two moments, μ, via $\kappa_1 = \mu_1$; and $\kappa_2 = \mu_2 - \mu_1^2$, where the second cumulant is the so called the variance, σ^2. With these definitions accounted for one can investigate the moments of the Brownian particle PDF,

$$G(k) = \frac{1}{\sqrt{4\pi D t}} \int_I \exp(ikx) \exp\left(-\frac{(x - x_0)^2}{4Dt} \right) dx \quad \text{(A.43)}$$

by completing the square and knowing the total area under a Gaussian one arrives at:

$$G(k) = \exp(ikx_0 - k^2 Dt) \tag{A.44}$$

Taking the natural log, and comparing powers of ik to the cumulant generating function, the first cumulant is $\kappa_1 = x_0$. which is as expected, namely that the mean position is the Gaussian centre. The second cumulant is $\kappa_2 = 2Dt$, the factor 2 comes from the factorial factor in the denominator of the cumulant generating function. From this, the second moment is calculated,

$$\mu_2 = \kappa_2 + \mu_1^2 = 2Dt + x_0^2 \tag{A.45}$$

Plugging the results for the first and second moments back, one finds the MSD,

$$\langle X^2 \rangle - \langle X \rangle^2 = 2Dt \tag{A.46}$$